Stony Brook University

Quantification and Control of Inhomogeneity in Wurtzite $(GaN)_{1-x}(ZnO)_x$ Semiconductors for Visible Light Absorption

A Dissertation Presented

by

Alexandra Audrey Reinert

to

The Graduate School

in Partial Fulfillment of the

Requirements

for the Degree of

Doctor of Philosophy

in

Chemistry

Stony Brook University

December 2014

Stony Brook University

The Graduate School

Alexandra Audrey Reinert

We, the dissertation committee for the above candidate for the

Doctor of Philosophy degree, hereby recommend

acceptance of this dissertation.

Peter Khalifah – Dissertation Advisor
Assistant Professor/Assistant Chemist, Stony Brook University/Brookhaven National Laboratory

Michael White - Chairperson of Defense
Professor of Chemistry/Senior Chemist, Stony Brook University/Brookhaven National Laboratory

John Parise – Third Member of Defense
Distinguished Professor, Stony Brook University

Peter Stephens – Outside Member of Defense

Professor, Department of Physics and Astronomy

This dissertation is accepted by the Graduate School

Charles Taber
Dean of the Graduate Schoo

Abstract of the Dissertation

Quantification and Control of Inhomogeneity in Wurtzite $(GaN)_{1-x}(ZnO)_x$ Semiconductors for Visible Light Absorption

by

Alexandra Audrey Reinert

Doctor of Philosophy

in

Chemistry

Stony Brook University

2014

Semiconductors must absorb energy from solar photons and subsequently transport photogenerated electrons and holes to surfaces in order to drive the H_2 and O_2 formation half-reactions of solar water splitting. The hexagonal wurtzite $(GaN)_{1-x}(ZnO)_x$ semiconductor solid solution has produced promising results for visible light solar water splitting, but has yet to achieve an efficiency high enough for practical applications, and the origin of the efficiency limit remains unknown. In this work, a detailed investigation of the average and local structure of these materials has been conducted in order to gain insights into how to improve water splitting efficiencies. Our analysis of $(GaN)_{1-x}(ZnO)_x$ samples up to $x \sim 0.67$, has led to the discovery of previously unrecognized types of compositional and structural defects.

A new high zinc content $Ga_2O_3(ZnO)_{16}$ (2:16) precursor, was developed to prepare higher zinc content oxynitrides. The use of this precursor results in the production of arrays of nanorods with favorable diameters and band gaps for visible light solar water splitting. Optical

measurements of these 2:16 precursor samples have shown to be sensitive to small amounts of free carriers whose presence is indicative of compositional defects. Complementary quantitative phase analysis by thermogravimetric analysis, on nanorod samples ranging from $x_v = 0.08 – 0.52$, suggests a substantial quantity of cation vacancies (~3%) may be present.

A structural defect in the form of a common zinc-blende (cubic) intergrowth was discovered from transmission electron microscopy measurements. This defect was found to have a uniform size throughout many particles. The abundance of this defect is dependent on both the precursor used during synthesis and the overall zinc content. Further supporting evidence for this cubic intergrowth phase is provided by ^{14}N solid state NMR experiments. Samples synthesized from the novel $Ga_2O_3(ZnO)_{16}$ precursor show no evidence of cubic intergrowths, while samples synthesized from a popular $ZnGa_2O_4$ precursor show varying amounts of cubic intergrowth with changes in zinc content and reaction conditions.

A new method has been developed for using powder diffraction techniques to quantify the amount of this cubic zinc-blende intergrowth. This intergrowth can be modeled in Rietveld refinements using large *c*-axis superstructures. However, intergrowths such as in this work cannot be seen as explicit diffraction peaks, but are hidden as partial intensities in the existing wurtzite diffraction pattern peaks. Supercells consisting of 80-100 total layers are created with layers of hexagonally close packed atoms and layers of cubic closed packed atoms. Ideal supercell models were investigated and have shown to improve fits to the data as compared to using a typical wurtzite unit cell model. This supercell method for modeling intergrowths is easily applicable to other polymorph systems. It allows for quantification of the amount of intergrowth present using a bulk average structural technique.

The local environment of atoms in $(GaN)_{1-x}(ZnO)_x$ have been investigated through solid state NMR and pair distribution function studies. ^{71}Ga NMR studies suggest inhomogenous local cation environments that are dependent upon the percentage of zinc in samples. Modeling of neutron pair distribution function data confirms clustering on the local scale and provides a quantitative measure of the differences in bond lengths locally, changes that result from differences in the local composition and bond strengths. Quantitative fitting of the first (nearest-neighbor) PDF peak (~2.0Å) finds that the Ga-N bond distances shrink upon introduction of ZnO into GaN. At low Zn contents, the Zn-O bond lengths are lengthened substantially and relax to nearly the expected average value at the halfway point of the GaN/ZnO solid solution (x = 0.50).

The compositional and structural deviations from an average wurtzite structure, as shown through defects and local disorder in this work, stress the importance of conducting an in-depth analysis of these and all materials with potential uses in water splitting. In particular, the defects found in this work may allow for their systematic influence on band gap and efficiency for photoactivity to be resolved.

Dedication Page

Dedicated to my parents, Elizabeth and John Reinert, my biggest fans and greatest supporters

Table of Contents

List of Figures

List of Tables

List of Abbreviations

BVS – bond valence sum

DFT – density functional theory

DR – diffuse reflectance

GZNO – gallium zinc oxynitride

KM – Kubelka-Munk

LDH – layered double hydroxide

MAS – magic angle spinning

ND – neutron diffraction

NMR – nuclear magnetic resonance

NPDF – neutron pair distribution function

PDF – pair distribution function

SEM – scanning electron microscopy

STEM- scanning tunneling electron microscopy

TEM – transmission electron microscopy

TGA – thermogravimetric analysis

XPDF – X-ray pair distribution function

XRD – X-ray diffraction

2:16 – $Ga_2O_3(ZnO)_{16}$

Acknowledgments

I would like to thank my advisor Dr. Peter Khalifah for his guidance throughout my PhD career. This project has been a great platform for learning a number of techniques, being a part of a number of valuable collaborations, and for growing as a scientist. I would also like to thank Dr. Michael White and Dr. John Parise for helping whenever asked and serving as my committee members for the last 6 years. Without all of your guidance I would not have been able to complete this research project.

I would also like to thank all of my past and present fellow group members for offering assistance and friendship throughout my time here. I am fortunate to have been a part of such a wonderful group of scientists.

I would like to also thank my collaborators; Dr. James Ciston who not only measured my samples via transmission electron microscopy but analyzed them in detail, without which a major portion of this work would not be possible; Dr. Fulya Dogan for her collection and analysis of all solid state NMR data shown in this work and to Dr. Derek Middlemiss for his added DFT insights and Dr. Clare Grey overseeing this work; Dr. Katherine Page and Thomas Proffen for spending countless hours teaching me how to collect and analyze PDF data; Dr. Ashfia Huq and Dr. Mikhail Feygenson for their help in neutron diffraction and PDF measurements; and finally Huafeng Huang who will be continuing on with this project and who provided me with data on his LDH $(GaN)_{1-x}(ZnO)_x$ samples.

I am extremely grateful to my close friend Diane Colabello for her constant encouragement and support. A true friend for life. Finally I would like to thank my home support system; my parents and Tom for their love, understanding, and constant encouragement.

Vita, Publications and/or Fields of Study

A. A. Reinert, C. Payne, L. Wang, J. Ciston, Y. Zhu, P.G. Khalifah, "Synthesis and Characterization of Visible Light Absorbing $(GaN)_{1-x}(ZnO)_x$ Semiconductor Nanorods", *J. Inorg. Chem.*, **2013**, 52, 8389-8398.

Chapter 1

Introduction

1.1 Overview

The need for a renewable alternative energy source is necessary due to the rising levels of CO_2 emissions produced from the burning of fossil fuels. While fossil fuel reserves, such as those for coal and natural gases, are not going to run out in the very near future, they are going to run out eventually.[1] It is estimated that the remaining fossil energy reserves could supply a 25 – 30 TW energy consumption for a few centuries.[2] The real problem with using these sources of fuel however, is from the production of CO_2 gas when these fuels are burned. Approximately 85% of the energy produced in the world is from the burning of fossil fuels, and for the last two hundred years, a shift in the types of fossil fuels used, from wood and coal to oil and gas, has occurred. Oil and gas are overall less harmful to the environment in terms of CO_2 production because of their higher hydrogen to carbon ratios, which in a combustion reaction allows for more water and less CO_2 to be produced when compared to coal.[3,2] CO_2 emissions, however, are cumulative, and impact the planet for 500 to 2,000 years following its emission.[2] Atmospheric CO_2 concentration has been shown to be correlated with rising sea levels and temperature swings that could potentially be the causes for ice ages on the planet.[2] Through the greenhouse effect, these rising levels of CO_2 accumulation in the atmosphere can cause a rise in the mean global temperature.[4]

Carbon dioxide also plays a role in acidifying the oceans and destroying coral reefs. The oceans absorb approximately 70-80% of emitted CO_2, which forces the reaction of an abundance of carbonate ions ($CaCO_3$ in deep sea sediments) with carbon dioxide and water. This process, known as sea floor neutralization, forces a decrease in the concentration of carbonate ions and throws the ocean out of balance causing chemical erosion.[5]

$$CO_2 + CO_3^{2-} + H_2O \leftrightarrow 2HCO_3^- \quad (1.1)$$

Supressing the amount of CO_2 gas emitted is not the answer to this ever growing problem. An alternative and clean energy source needs to be implemented.[4] The longer it takes to implement a zero carbon emission energy source, the more of that zero carbon emission energy source will be needed, especially when accounting for the expected increase in power consumption by the year 2050 (expected 27.6TW).[4] Electricity is a convenient form of energy produced from fossil fuels, but it is fairly inefficient as compared to non-electrical forms of energy such as natural gas and gasoline. Zero carbon emission energy resources such as hydro, ocean, wind, geothermal, and solar have all been investigated for their applicability, cost-effectiveness, and efficiency. From an analysis in 2006, it was discovered that solar, wind, geothermal, and ocean waves are the four sources with theoretical potentials exceeding 15TW, while only solar and wind have extractable potentials exceeding 15TW. Finally, solar was the only resource found to have technical potential exceeding 15TW, making it an attractive resource for a future zero carbon emission energy source to replace fossil fuels.[4]

1.2 Photoelectrolysis

Of the many sources of energy available, the sun is the most abundant and efficient. Many have focused on work dealing with thermal energy from the earth, oceanic and tidal energy, and even energy from wind or biomass in order to facilitate with the world's energy needs. None of these sources of energy are abundant, efficient, or cheap enough to supply sufficient amounts to the entire world. Energy produced from the sun is the only renewable source with enough potential to provide levels necessary to power the entire globe. In one hour, the sun on average provides 120,000TW of power, which is more than needed to power the earth in one year, and yet in the year 2001 only approximately 1.6% combined electricity and fuels were provided by solar sources.[1,2] While a large amount of this energy is lost to a number of factors including power residing in the inaccessible deep oceans, enough is still available for worldwide use of this zero carbon emission resource.[4] Solar photons do not cause

environmental threats, making them appealing for energy applications.[3] In addition, when taking into account the solar flux hitting the earth (1.37kW/m^2) the theoretical potential of solar power can be calculated to be equal to 89,300 TW using the average flux over the earth's surface area. This value represents more energy hitting the earth's surface in one and a half hours than energy consumed in the year 2001 from all energy sources (approximately 13.5 TW or 425 x 10^{18} Joules).[2,4] With this information, a calculation to generate 15 TW of zero carbon power from a solar-conversion system that is only 10% efficient would need to only cover 0.17% of the earth's surface area, which is equal to 858,792 km^2.[4]

Using solar energy requires both capture and conversion to a usable chemical fuel.[2] Converting solar power to a usable chemical fuel can be done in three ways; solar electricity, solar fuels, and solar thermal. Solar electricity assumes that the capture of concentrated sunlight is converted into electricity, and has an efficiency of approximately 87%. This electricity then needs to be converted to a chemical fuel, taking our theoretical potential of 89,300 TW down to 58,300 TW. Storing electricity is a feat in itself, as a battery with a 30 year lifetime necessary for a solar device, that is also inexpensive, does not exist.[2] It is important to note that the time of day and time of year also play a large factor in the efficiency of devices used for harvesting solar electricity as exposure to sunlight changes throughout the day/year. For solar fuels it is only necessary to take part in a single conversion, to a chemical fuel. With the assumption of un-concentrated sunlight, solar fuels have an efficiency of approximately 68% and provide an overall useable 60,700 TW of power. Examples of solar fuels include biomass and liquid organic materials produced from photosynthesis type processes. Solar thermal power is by far the least efficient, as it requires an initial conversion into heat followed by conversions to mechanical, electrical, and finally chemical energy. Out of a theoretical 89,300 TW available, only 19,400 TW would be usable through solar thermal applications. However, it is the cheapest method of capture, conversion, and storage.[2] From an economic standpoint, in 2010 renewable energies cost approximately

$3.80/W, and the projected goal is a cost of $1/W.[6] The energy potentials of these and other harvesting technologies are depicted in Figure 1. These calculations stress the importance of using a technology that produces chemical fuel and lacks conversions that ultimately decrease the usable amount of energy available.[4]

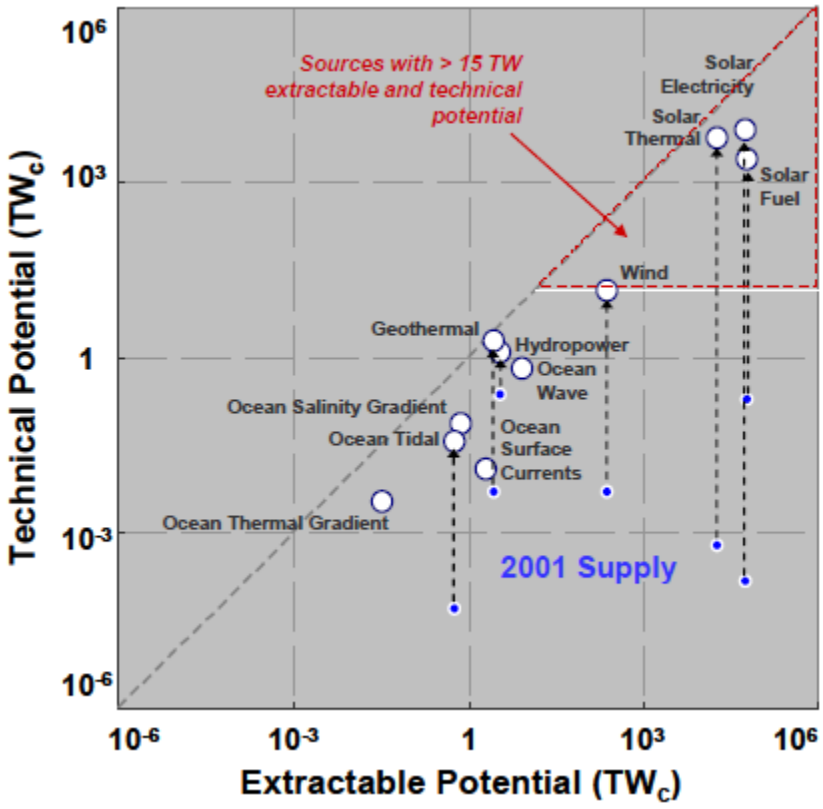

Figure 1.1. Energy potentials of various energy harvesting technologies circa 2001[4].

Implementation of a large scale photosynthetic process in plants has proven to be inefficient, as large areas of land would be needed with optimal environments for plants.[4] Only about 3-4% of energy from sunlight that hits a leaf's surface is converted into energy via photosynthesis, and even less of this is actually stored.[7] Photosynthesis takes carbon dioxide, water, and photons from the sun and converts them into sugars and oxygen. The process is effective, however the percentage of stored energy is not nearly enough to have efficient storage for our planet via plants only. However, a technology that takes into account the process of photosynthesis, but gives an overall higher efficiency compared to plants and

algae, could be used to produce alternative solar fuels using semiconductors. Just as photosynthesis produces O_2 from H_2O, the process of water splitting has been discovered to produce both O_2 and H_2 providing both a zero carbon fuel and water as a regenerated product to start the process over again.

Water splitting involves the evolution of O_2 as one component and the formation of a reduced fuel (H_2) as the other. A photoelectrochemical cell is the reaction vessel used for this process and consists of two electrodes and an electrolyte. In this type of cell one of the electrodes is made of a semiconductor which produces current through the cell and leads to the production of chemical fuels.[8] A semiconductor electrode, when immersed in water and illuminated, creates an electric field at the interface between the solid electrode and the liquid causing charge separation. Known as the Becquerel effect, or the occurrence of the photovoltaic effect, electrons are transferred from one electrode to another due to this charge separation.[9] A counter electrode made of metal, such as Pt, is also immersed in the liquid. Figure 1.2 depicts the reaction setup in a photoelectrochemical cell. Photons from the sun are absorbed by a photocatalyst (semiconductor) producing energetic holes and electrons, which travel to the surface of the photocatalyst and take part in two separate half reactions if the electrons and holes have enough energy to overcome the band gap energy of the material and overpotentials, as shown in the following equation.

$$4H^+ + 4e^- \rightarrow 2H_2$$

$$\underline{2H_2O \rightarrow O_2 + 4H^+ + 4e^-}$$

$$2H_2O \rightarrow 2H_2 + O_2 \qquad (1.2)$$

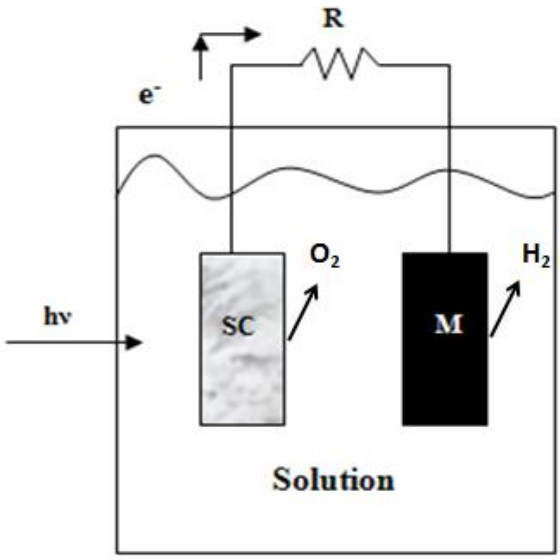

Figure 1.2. Schematic of a photoelectrochemical cell.

Water splitting is a multi-electron process that involves a number of barriers that need to be overcome in order for it to be efficient. Barriers include the necessities of having: strong light absorption, suitable band positions of the semiconductor, sufficient charge transport, high chemical stability, low overpotentials, and low cost. Figure 1.3 shows the spectral distribution of light spanning from the ultraviolet to the near infrared regions of light. It is clear that the UV region of the spectrum accounts for only about 5% of the total sunlight hitting the earth, whereas the visible light and near infrared regions account for approximately 45% each. The near infrared region is large in size compared to that of UV, but for water splitting is also inefficient due to the energy needed for the two half reactions to occur. After about 1000 nm, or 1.23 eV, any smaller band gaps will not be able to participate in solar water splitting reactions. The exception to this was found in using a Si/partner device where the low band gap energy Si (1.1 eV) is partnered with a wider band-gap semiconductor species. This allows the generation of enough current to be produced with voltages exceeding those thermodynamically required for producing fuel.[10] The visible region, which spans from about 380 to 750 nm equates to approximately 3.3 – 1.6 eV on an energy scale. These values are important, as

semiconductors involved in water splitting must have band gap energies that are sufficient for visible light photoelectrolysis, and also have suitable band positions. This is the motivation behind working on semiconductor materials that absorb in the visible region of the solar spectrum. In order to better understand the chemistry behind some of the properties of semiconductors that are required for effective solar water splitting, the band gap energies must be analyzed.

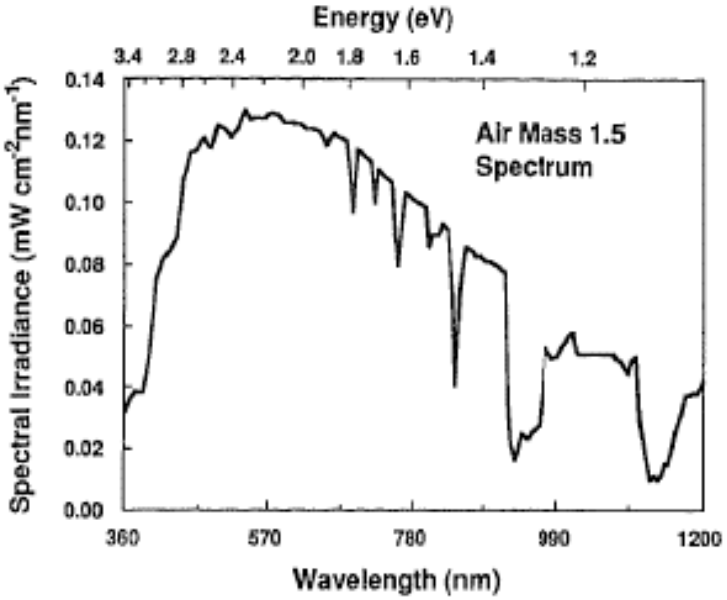

Figure 1.3. Spectral distribution of sunlight under Air Mass 1.5 conditions of when the sun is 48° above the horizon.[11]

For absorption to occur, an incoming photon must have energy greater than or equal to the band gap (E_g) of the material absorbing that photon. A semiconductor has both a valence band and a conduction band, relating to the LUMO and HOMO respectively in molecular orbital theory. The electronic properties of all semiconductors rely greatly on the size of the gap between the top of the valence band and the bottom of the conduction band, or the band gap. The valence band edge is associated with the highest energy of the valence band, while the conduction band edge is associated with the lowest energy of the conduction band. The band gaps of semiconductors can also offer insight into the stability of the material. Covalent semiconductors, such as silicon, tend to have small band gaps

while ionic semiconductors, such as TiO_2, have larger band gaps. The larger band gap of TiO_2 makes the material more stable and less likely to undergo corrosion or oxidation. This is because the closer the band gaps are to one another, the more reactive the semiconductor is thought to be.[11]

As was briefly discussed earlier, a semiconductor used for water splitting absorbs photons from the sun. Absorption of this incoming photon excites an electron from the top of the valence band to the bottom of the conduction band. This in turn leaves holes in the valence band and partially fills the conduction band. Figure 1.4 depicts this phenomenon along with pertinent band positions necessary for the production of H_2 and O_2 to occur. The valence band edge (E_{vbe}) and the conduction band edge (E_{cbe}) must be at energies that effectively straddle the potentials necessary for oxidizing H_2O to O_2 (1.23 eV) and that for reducing H^+ to H_2 (0 eV) based on the values for a normal hydrogen electrode reference at pH = 0.[12] The electric field produced at the interface between the semiconductor and water prevents the recombination of holes and electrons.[13] The actual band gap however must be larger than 1.23 eV due to overpotentials, or the difference between the thermodynamically determined reduction potential and the actual potential observed from the redox reaction. Overpotentials have been calculated to be approximately 0.3–0.4 eV, which increases the minimum band gap energy to approximately 1.5–1.6 eV. Thermodynamic losses must also be accounted for (~0.4 eV), raising the minimum band gap energy required for overall water splitting in a single semiconductor system to approximately 1.9–2.0 eV.[13]

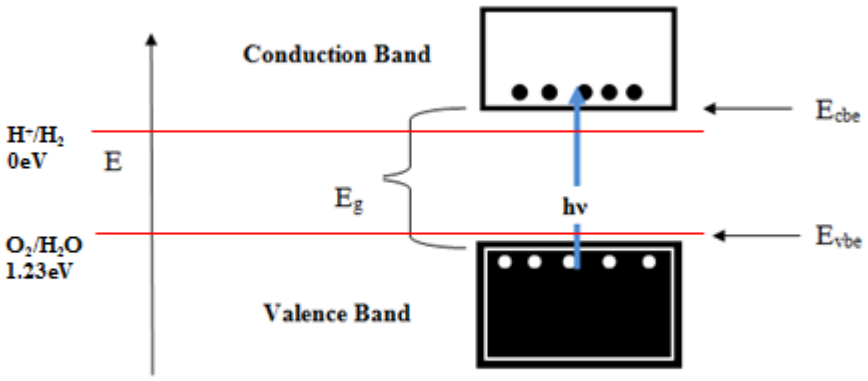

Figure 1.4. Band diagram depicting excitation of electrons to conduction band and creation of holes in valence band.

With all new energy research it is important to remember that the major problem with solar technologies is in their cost effectiveness. Fossil fuels are still the major source of energy today because they are much cheaper than the cost of solar technologies. The cost of solar energy is directly related to the low conversion efficiencies gained from these technologies, and sometimes due to the costly materials involved.[3] Materials used for solar water splitting need not only be efficient in producing H_2, the fuel, but also need to be made from inexpensive components to drive down their cost.[2]

1.3 Photoactive semiconductors for solar water splitting

In 1972 the first evidence of the production of oxygen and hydrogen gases using a semiconductor electrode and counter Pt electrode in a photoelectrochemical cell was found by Honda and Fujishima.[14] This was the first discovery of water decomposition via light absorption by a semiconductor. This was an important discovery but involved the use of UV light irradiation and an applied external voltage. After this initial find, a number of metal oxides were tested for their abilities to split water. $SrTiO_3$, WO_3, and $BaTiO_3$ are just a few materials that made an impact on the history of water splitting. $SrTiO_3$ was found to be very stable in this application, and was the first to be able to

split water without an applied potential.[15] WO_3 was the first of these materials with water splitting capability using visible light irradiation, but with the addition of a Pt co-catalyst and an applied external voltage.[16] Still this was a step above TiO_2 which used UV light irradiation. This material was still found to have a very low quantum efficiency of 0.1%. All three of these materials had band gaps around 3.0eV, accounting for at least a portion of their low efficiencies.

The use of a NiO catalyst was found to improve efficiencies of metal oxide materials in the 1980s by Domen *et al.* $SrTiO_3$ and $K_4Nb_6O_{17}$ are two examples of such materials that were improved in this manner.[16a],[17] $SrTiO_3$ to was still only able to participate in solar water splitting under UV light irradiation, and layered $K_4Nb_6O_{17}$ with a band gap of 3.3 eV was able to split water only under UV conditions as well. By itself $K_4Nb_6O_{17}$ split water non-stoichiometrically at a very low rate, but after modification with 0.1 wt% NiO was able to achieve quantum efficiencies of 5.3-20%.[16b]

Complex oxides often consisting of layered structures were found in the 1990s to have water splitting capabilities. $La_2Ti_3O_9$, $NaInS_2$, and $La_4CaTi_5O_{17}$ are just a few examples of these complex oxides. $La_4CaTi_5O_{17}$, like $K_4Nb_6O_{17}$, was modified with a NiO co-catalyst leading to increased quantum efficiencies. A perovskite structured large band gap (3.8 eV) material, $La_4CaTi_5O_{17}$/NiO was found to split water under UV irradiation with a quantum efficiency of up to 20%. In 1998 Hara *et al*. discovered that Cu_2O, an unstable material, was able to produce H_2 and O_2 at visible light region wavelengths of $\leq$ 600 nm. They also found $CuFeO_2$ to be useful in visible light water splitting, leading to the thought that perhaps linear –O-Cu^I-O bonds in a structure could be the basis for a new group of visible light solar water splitting materials.[18] Visible light solar photoelectrolysis offers the promise of the production of H_2 gas as a product of "splitting water" with higher efficiencies than would be achieved using UV wavelength photons. This is clearly depicted in the spectral distribution of light which was discussed earlier and can be seen in Figure 1.3.

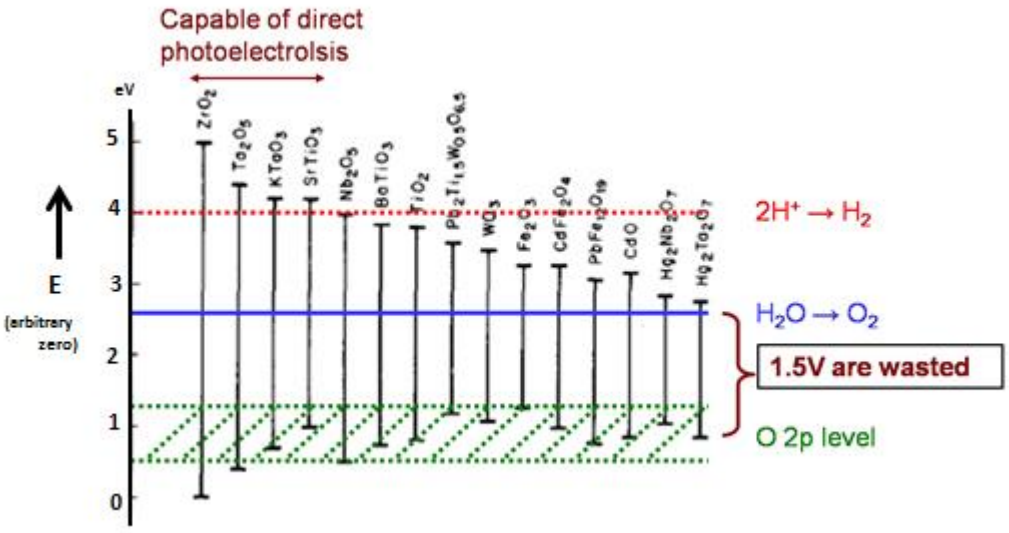

Figure 1.5. Band edge positions and energies of selected common semiconductors adapted from Kung *et al*.[19]

Figure 1.5 depicts the band gaps and relative band edge positions of a number of oxide semiconductors as compared to the potentials necessary for hydrogen reduction and oxygen oxidation. Almost all of these materials have unsuitable conduction band edges, and therefore cannot effectively produce H_2 and therefore cannot participate in overall water splitting without the use of added co-catalysts specific for H_2 production. It is also important to note that these oxides have large overpotentials due to the much lower energy levels of oxygen 2p states as compared to the potential for producing O_2. Wasted energy and unsuitable band positions seem to be large hindrances for many oxides in water splitting applications. Photoelectrochemical cells have become complicated in their design, and the use of a single material photocatalytic system would be advantageous for both cost effectiveness and design complicatedness. A system with less equipment and a photocatalyst immersed in water is cheaper and more efficient than a photoelectrochemical cell. These systems however, often require sacrificial reagants in order to produce both hydrogen and oxygen. In 2002 Kasahara *et al*. discovered $LaTiO_2N$, an oxynitride, to have the ability to produce H_2 and O_2, with the use of methanol as a sacrificial electron donor and Ag^+ as a sacrificial electron acceptor.[20] The oxynitride was

synthesized via the nitridation of $La_2Ti_2O_7$ at 850°C under ammonia flow at a rate of 20 ml/min. Visible light irradiation from 420 nm – 600 nm was implemented, instead of the more commonly used UV irradiation. DFT calculations were also conducted in order to understand specifics about orbitals in the valence band and conduction band edges. What was discovered is that the bottom of the conduction bands are comprised of empty d orbitals, while the top of the valence bands consisting mainly of N2p orbitals hybridized with O2p orbitals. These efforts only led to an overall quantum efficiency of 0.15% for H_2 production, however a material capable of visible light driven overall water splitting was discovered.

The overall solar-to-hydrogen conversion efficiency can be determined by using equation 1.2 where j is the photo-current density (Am^{-2}), P_{light} is the incident light intensity (W/m^2), V_{redox} is the potential required for water splitting (1.23 eV), and V_B is the bias voltage that can be added in a two electrode system to assist in water splitting.[13] Modifications to materials in order to alter their band gaps have the potential to lead to a higher efficiency.

$$\eta_{STH} = j(V_{redox} - V_B)/P_{light} \quad (1.3)$$

Materials for water splitting applications must also be able to sustain the oxidation and reduction reactions to produce large amounts of H_2 and O_2. In the case of $LaTiO_2N$, it was discovered that the material was partially degraded during the photooxidation of water. It was suggested that modifications to the photocatalyst could help resolve this problem.[20] Further work on this system showed that the Ti concentration on the surface of the material decreased with increasing nitridation time, overall decreasing the photocatalytic activity after 72h.[21] This is merely one example of many materials discovered that have a problem with stability. In addition, there are a number of materials with the ability to split water using UV light and with high quantum efficiencies, while only a few can split water using visible light and always lead to low efficiencies. As of now, a material capable of catalyzing the decomposition of water into H_2 and O_2 under visible light irradiation with a quantum efficiency larger

than 10% has not been found.[16b] It is therefore important that we find a material that is not only efficient in splitting water, but is stable enough to be able to sustain long reaction times, has a small band gap, contains suitable band edge positions, and has sufficient charge transport**.**

1.4 $(GaN)_{1-x}(ZnO)_x$ semiconductors for visible light solar water splitting

As nitrogen is substantially less electronegative than oxygen (3.0 vs 3.5 for oxygen on the Pauling scale), a rise in the valence band energy occurs in nitride and oxynitride analogs of oxides, allowing for overall visible light water splitting without compromising the good stability of oxide semiconductors. This was seen through the decent quantum efficiencies obtained from both Ta_3N_5 (Eg = 2.1 eV) and TaON (Eg = 2.5 eV) materials.[22] In 2005 Maeda *et al*. discovered a new set of oxynitrides for overall water splitting with the promise for high quantum efficiencies, $(GaN)_{1-x}(ZnO)_x$ semiconductors.[23] This solid solution consists of GaN and ZnO end members, both of which are wurtzite structured wide band gap semiconductors with band gaps of 3.4 eV and 3.2 eV respectively and similar lattice parameters (ZnO: a = 3.249 c = 5.207; GaN: a = 3.189 c = 5.185). The wurtzite structure (SG # 186, $P6_3mc$, Figure 1.6) consists of tetrahedrally coordinated cations and anions. When combined as a solid solution, or semiconductor alloy, an increase in energy of valence band edge occurs, producing materials with smaller band gaps than the end members, as can be seen in Figure 1.7. This raise in the valence band edge suggests that with a change in zinc content of the solid solution there should also be a change in the band gap. When combined to make a solid solution, these virtually transparent end members produce visible light absorbing oxynitrides. The Domen research group discovered that an increase in zinc content resulted in a decrease in band gap energy for $x \geq 0.42$.[23,24] It is believed that the band gap of this system can be decreased to as low as 2.4 eV. This value was determined via the analysis of absorption band edges through linear extrapolation in order to estimate the onset wavelength at which light absorption occurs.[25] Density functional theory (DFT) calculations suggest a band gap in this system could be reduced to 2.29 eV with a Zn content of x = 0.525.[26,27,28]

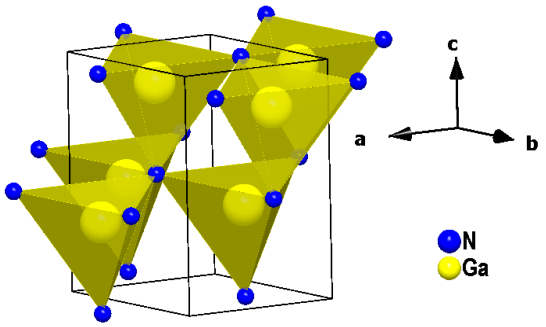

Figure 1.6. Wurtzite structure (SG #186 P6$_3$*m*c).

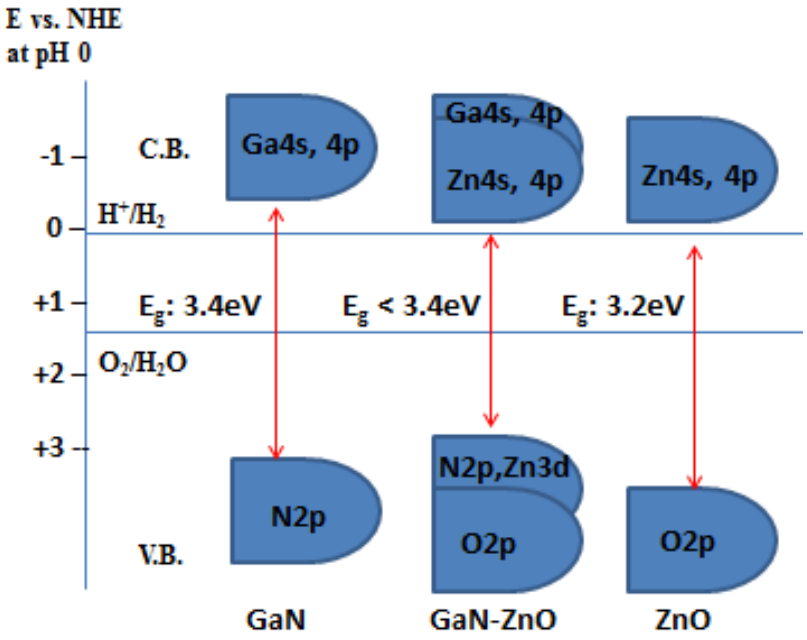

Figure 1.7. Depiction of band edges and band gap size of $(GaN)_{1-x}(ZnO)_x$ as compared to its end members.

The general synthesis route for producing these oxynitrides is via heating a mixture of Ga_2O_3 and ZnO at high temperatures, typically 850°C, under ammonia flow for several hours. Changes in flow rate and reaction time lead to variations in composition and homogeneity. Hashiguchi *et al*. obtained a zinc content of $x = 0.42$ from a mixture of Ga_2O_3 and ZnO nitride for 15 minutes at 950°C with a flow rate of 250 ml/min, which is the highest value of zinc recorded for gallium zinc oxynitrides with these

two starting materials.[29] ZnO volatization critically affects the synthesis of gallium zinc oxynitrides, as ZnO will volatize under reducing conditions at high temperatures. This suggests the need for an excess of Zn in the starting materials in order to achieve higher zinc content products due to loss during synthesis.

High pressure synthesis routes have shown to be successful in producting $(GaN)_{1-x}(ZnO)_x$ with $x = 0.50$ and $x = 0.75$.[30] High pressure synthesis routes however can generally only achieve small sample sizes. More recently, these solid solutions have been synthesized via Ga-Zn-O layered double hydroxide precursors, producing Zn-rich samples with x values ranging from $x = 0.5$ - 0.8 and reporting band gaps down to 2.35 eV.[31] This type of precursor formed porous particles that did not have well defined facets, but maintained the overall shape of the precursor crystallites. Prior work showed the same phenomenon in reactions between Ga_2O_3 and ZnO, where the particle size of the product depended greatly on the particle size of the ZnO reactant.[32] Other studies including the use of nanoscale $ZnGa_2O_4$ and ZnO precursors led to the production of Zn-rich samples ranging from $x = 0.30$ - 0.87, and band gaps ranging from 2.7 - 2.2 eV. Products were single crystalline particles due to the lower nitridation temperature of 650°C as compared to the bulk synthesis temperature of 850°C.[33] The $ZnGa_2O_4$ spinel precursor in general makes an effective precursor due to the premixing of Ga and Zn on an atomic scale.[34,30]

It is clear that a large amount of research has been done on this solid solution alone, and although this is one of the most effective systems for driving overall solar water splitting using visible light, its quantum yield has not yet reached ten percent (~6% with visible light photons).[35] In this work we explore the use of alternative Ga-Zn-O precursors that are substantially more Zn-rich than $ZnGa_2O_4$, along with conducting an in depth analysis of structural and chemical properties of this system, in order to gain insights as to how to increase the efficiency of this material.

1.5 Research objectives

This research is based on a series of $(GaN)_{1-x}(ZnO)_x$ solid solutions with varying zinc contents, synthesized from different precursors. A number of analytical techniques have been used to probe both the average and local structures of these solid solutions in order to understand and improve their efficiencies in visible light water splitting. Two main goals of synthesizing high zinc content oxynitrides, and synthesizing oxynitrides with smaller band gaps were achieved and led to an in depth analysis of the structure of these materials. Morphological studies have shown vast differences in shape and size of products synthesized from different types of precursors, and comparisons of samples from these varying precursors have been made ranging from band gap determination, to composition, and also to average and local structure investigations.

1.6 Experimental techniques

1.6.1 Powder Synthesis

Powder synthesis is a simple and direct method for producing a variety of inorganic compounds used in materials chemistry. Stoichiometric amounts of each reactant are mixed and ground well with a mortar and pestle to ensure small grain size and therefore greater surface area for an efficient reaction. The mixed powders are either placed in crucibles, reaction boats, or pressed into pellets. These powders or pellets are then heated in a furnace with a selected temperature or heating/cooling method for extended periods of time. This is known as the ceramic method, which is the most common method for preparing solids. In solid state diffusion a large amount of energy is needed in order to overcome the lattice energy, which is the energy needed to allow a cation to leave its position in the lattice. It therefore can often take long periods of time to obtain a single phase sample using this method due to structural differences between starting materials and the desired product. Increasing the temperature is a way to increase the diffusion rate of ions, therefore speeding up the reaction. Removing the reaction

mixture from the furnace and regrinding will allow for new surfaces to be in contact with the heat and gas flow and will also speed up the reaction.[36] Depending on the type of reaction desired, a number of different gas types can be used including air, O_2, H_2, N_2, Ar, or NH_3 during heating. In this work, a horizontal tube furnace is used, equipped with a 1" quartz tube that is sealed to the outside atmosphere, yet open to the desired flowing gas. The gas is exited through a bubbler in order to ensure neutralization or to easily acknowledge adequate flow rate. Solid samples produced in this manner can be analyzed in a number of ways, the first of which will be discussed is X-ray diffraction.

1.6.2 Powder X-ray diffraction

Powder X-ray diffraction is one of the most commonly used tools for identifying phase purity and the average structure of solid powders. In general, the necessary components for observing common objects include an X-ray source and a detector. While the human eye can detect most common objects, atoms are too small to be seen using a visible light source and therefore need to be observed using a suitable wavelength for individual atoms, X-rays. Diffraction can only been seen when the wavelength used is of the same order of magnitude as the distance between the scattering objects. This distance is approximately 0.5 - 2.5Å when working with crystals. X-rays scatter from the electrons, or electron density, that is distributed throughout a crystal lattice. Copper radiation, or K_α, is the most common type of radiation used for powder X-ray diffraction with a wavelength of 1.5418Å. This value is the average of the $K_{\alpha1}$ and $K_{\alpha2}$ wavelengths equal to 1.5404Å and 1.5443Å respectively, and refers to the transition of an electron from the L to K shell. K_β radiation also exists and refers to the transition from the M to the K shell. Both types produce characteristic lines on an X-ray spectrum that are indicative of an electron being ejected by another electron that was accelerated through the X-ray tube. The K_α radiation lines are much more intense than K_β spectral lines, which is why K_β filters are often used and an average of the two K_α radiations are implemented for producing an X-ray spectrum (Figure 1.8).[37]

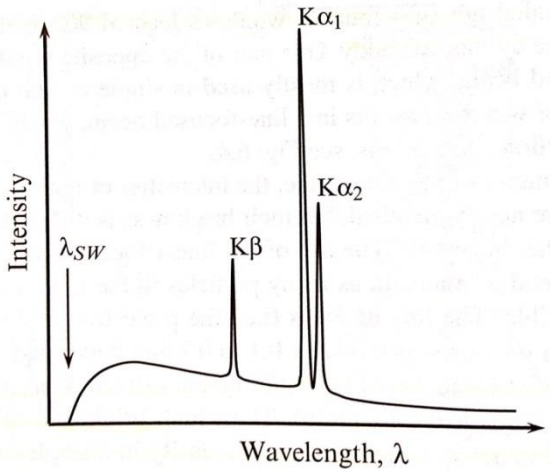

Figure 1.8. Schematic of a typical X-ray emission spectrum depicting three characteristic wavelengths: $K_{\alpha 1}$, $K_{\alpha 2}$, and K_{β}.[37]

Synchrotron radiation sources are more powerful than laboratory instruments and have large amounts of energy stored in synchrotron rings where accelerated electrons are moving in an orbit around the ring. The electrons are controlled by a magnetic field and have relativistic velocities. Newer synchrotron rings are not perfectly circular, but shaped slightly differently due to bending magnets and tangential beamlines. With high brilliance and a high intensity observed for a large range of photon energies, wavelengths may be chosen and changed when needed. This allows for energy dispersive measurements where angle is constant and wavelength is changed. This is the opposite of laboratory X-ray instruments which have a fixed wavelength and vary angle during data acquisition. Figure 1.9 shows a schematic of a synchrotron ring.

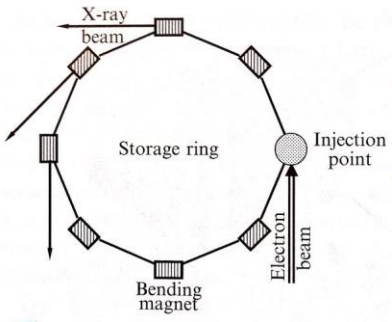

Figure 1.9. Synchrotron ring depicting radiation output from the use of bending magnets.[37]

The effectiveness of an atom in scattering X-rays is known as the atom's scattering factor (f_0). The scattering factor depends on the wavelength of X-ray radiation, the atom's atomic number, and the Bragg angle θ. The heavier the atom is, the better it will scatter X-rays. There is however a decrease in scattering power with an increase in Bragg angle. This is due to the fact that electrons are distributed around the nucleus of the atom, and as X-rays are scattered by an electron in one part of the atom they are also out of phase with those scattered in a different part of the atom. This results in diffraction patterns consisting of peaks of identical Miller indices but with differing intensities for materials with the same crystal structure. This is where the structure factor comes into play. The structure factor, or F_{hkl}, is dependent on both the position of each atom in a lattice and its scattering factor. For j atoms in a unit cell, F_{hkl} is equal to the following equation:

$$F_{hkl} = \sum_j \boldsymbol{f_j}\, \boldsymbol{e^{2\pi i(hx_j+ky_j+lz_j)}} \qquad (1.4)$$

The intensity of a particular *hkl* reflection, I_{hkl}, is proportional to the square of the structure factor, and taking the square root of this intensity will provide an amplitude for the structure factor.[36]

A crystal is modeled as a series of parallel planes of atoms that are separated equally by a distance *d*, known as the interplanar distance. Diffraction from a set of these planes is only possible at a specific angle which is determined from Bragg's law ($2d\sin\theta = n\lambda$), where *d* is the interplanar spacing, n is the order of reflection, θ is the angle between the incident beam and the plane, and λ is the wavelength of the incident beam.[37] Figure 1.10 depicts how the components of Bragg's law are measured.

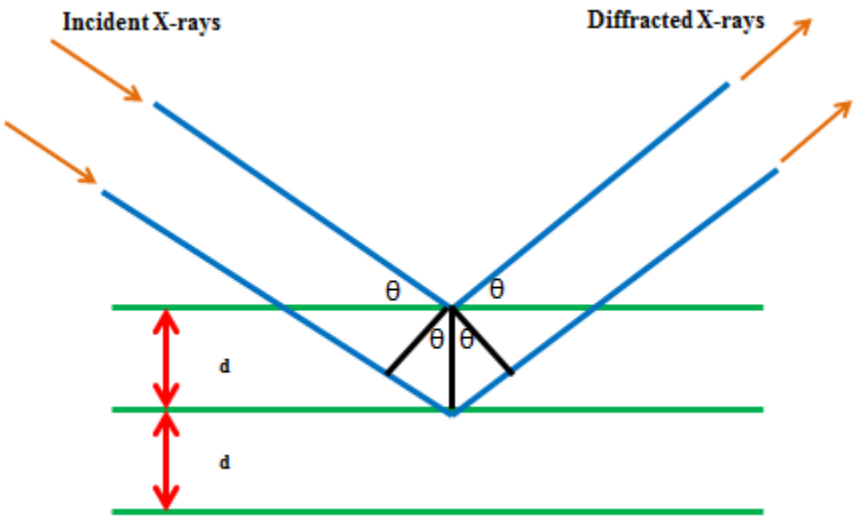

Figure 1.10. Schematic of Bragg Diffraction.

A family of crystallographic planes is described using *h*, *k*, and *l* integer indices, known as Miller indices. These indices are the definition of dividing unit cell edges **a**, **b**, and **c** of a crystal into *h*, *k*, and *l* equal parts respectively. In a powder diffraction pattern, peak positions are determined as a function of unit cell dimensions, where d is a function of the unit cell parameters and Miller indices.[37] A separate formula exists for each crystal system, but for the purposes of discussing $(GaN)_{1-x}(ZnO)_x$ systems, a hexagonal system is used and is described as follows:

$$\frac{1}{d^2} = \frac{4}{3}\frac{h^2 + hk + k^2}{a^2} + \frac{l^2}{c^2} \qquad (1.5)$$

A more in depth discussion of diffraction patterns and modeling peak positions and intensities will be discussed in the next section, but it is important to note that laboratory X-ray data is often implemented in order to conduct cell refinements on a powder sample. This allows for the calculation of lattice parameters if the crystal system of the sample is known. The amount of zinc in the sample, or x in $(GaN)_{1-x}(ZnO)_x$, was determined via EDX spectroscopy by previous workers. In this work, an estimation of zinc content was calculated via Vegard's law, which states that an approximately linear

relation exists between the lattice parameter of a solid solution and the concentrations of the elements in that solid solution.[38] The equation below is Vegard's law for ZnO in the wurtzite phase. The *a* lattice parameter depends on the zinc content, which is denoted by x_v. A determination of *a* from an initial cell refinement using lab X-ray data on samples, provides an estimate of zinc composition before an in depth analysis of the sample is made.

$$a = 0.06x_v + 3.198 \quad (1.6)$$

1.6.3 Powder neutron diffraction

Powder neutron diffraction is an invaluable tool when you have a system consisting of atoms whose X-ray scattering factors are poor. The main difference between X-ray and neutron radiation is that X-rays scatter from electrons while neutrons are scattered by nuclei, which are much smaller than electron clouds.[37] Unlike with X-rays, light atoms scatter neutrons just as well as heavy atoms. In addition, scattering factors of elements remain constant over the whole range of Bragg angles in neutron diffraction and their scattering functions are not proportional to the atomic number. Neutrons can come from two different types of sources, reactor and spallation. Neutrons from a reactor are released via atomic fission processes from a uranium target. They have very high velocities and a very small wavelength, and can be slowed using heavy water so that they can be applicable for structural studies. These generated neutrons have a wide spread variation of wavelengths, so a monochromatic beam is created from the reflection of the neutrons from a particular plane of a single crystal. Spallation sources bombard protons on metal targets in order to produce neutrons. Instead of using a fixed wavelength and varying the Bragg angle, spallation neutrons collect data from the entire beam of neutrons with all of their varying wavelengths at a fixed angle, and the diffraction pattern is created by reporting the data as a function of the time-of-flight of the neutrons.[36] Neutrons are important for this study because both the cations and the anions in $(GaN)_{1-x}(ZnO)_x$ are directly next to one another on the periodic table. This makes their X-ray scattering factors very similar. The neutron scattering factors of Ga and Zn are 7.288

fm and 5.680 fm allowing the two atoms to be distinguished from one another. Nitrogen and oxygen are also very light atoms that can easily be detected via neutron diffraction and have differing neutron scattering factors, 9.36 fm and 5.805 fm respectively, allowing them to also be differentiated from one another.

Both X-ray and neutron powder diffraction data are implemented for structural determination, phase purity, and percent composition of particular phases of solid samples. A crystal structure is not considered completely determined until all of the variables and parameters of a model have been refined against the raw powder diffraction data. The Rietveld method is the most commonly used method for structure refinement and is a full pattern or full profile type refinement. All integrated intensities are included in every calculation as functions of geometrical, sample, and structural parameters. In Le Bail method refinements, the only initial parameters needed are those such as unit cell, peak-shape, and coordinates of atoms. Conversely, the Rietveld method requires that all initial parameters be suitable for the refinement to run well.[37] The Le Bail method allows refinements to be conducted on background, peak shape, and lattice parameters, while the Rietveld method includes the refinement of these and a number of different structural parameters including: scale factor, atom positions (if not special), displacement parameters, crystallite size, strain, etc. The Rietveld method also allows for quantification of phase fractions in a multi-phase material, but regardless what the purpose of the refinement may be, a suitable model must be implemented.[37] The goodness of fit determined through a Rietveld refinement is calculated based on the difference between the observed intensity and the calculated intensity of a model. Programs such as TOPAS allow for user defined functions and macros to be implemented for sample specific special parameters, allowing for complicated structure models to be refined. Specific parameters and models will be discussed in subsequent chapters for the refinements of $(GaN)_{1-x}(ZnO)_x$ samples.

1.6.4 Scanning electron microscopy

A scanning electron microscope sends a focused beam of electrons onto the surface of a sample. The electrons scatter and are measured to form an image. Non-conducting samples require the use of a gold or graphite coating in order to ensure that build-up of surface charge does not occur. Used to study morphology and size, a scanning electron microscope can image over a large range of magnifications (approximately 100Å to 100 µm) allowing a sample to be seen at an almost atomic level.[39] The microscope consists of an electron gun, vacuum column, electron beam, target, detector(s), and a monitor. Electrons are produced in the electron gun and are accelerated through the column with an energy value between 1 and 40 keV.[40] Keeping the beam in a vacuum will ensure that the electrons do not interact with other materials, but also means that the specimens used cannot be in the liquid state, which in our studies is not a problem.

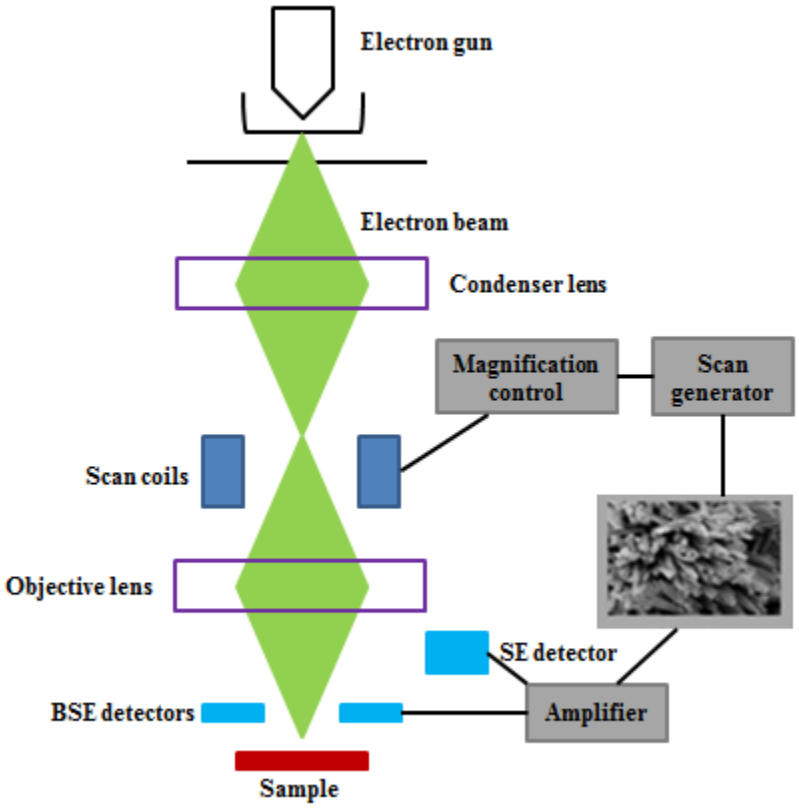

Figure 1.11. Components of a scanning electron microscope.

SEM images depend on three parameters; electron probe size (d_p), electron probe current (i_p), and electron probe convergence angle (α_p). Having a 3D sample is what makes this technique attractive for imaging, and it is important to have the correct values of the above parameters in order to get high quality images. 3D specimens are often not uniform and may contain areas with different heights, therefore in order to get a high depth-of-field image, a small convergence angle is needed. This ensures that the beam seems small over all different heights on the specimen.[40] Using a long working distance, which is the distance from the bottom of the objective lens to the surface of the specimen, can help achieve this. High-resolution images require a small probe size and a good amount of current. Lastly, high image quality can be obtained by weakening the condenser lens.[40]

There are two general types of electron-specimen interactions; elastic scattering and inelastic scattering. Elastic scattering occurs when the electron is deviated from the original beam at a certain angle. In this process, the original energy of the electron is unchanged by the change in direction.[40] Specifically, back-scattered electrons are used for composition determination, in a specific area of the specimen, as they depend on Z, or the atomic number of the specimen. The higher the atomic number the more scattering that will occur. A back-scattered detector is used to collect this type of electron. Inelastic scattering occurs when the electron not only changes direction, but also changes energy. The electron's final energy is always less than it was originally in the beam. This type of scattering creates secondary electrons, Auger electrons, and x-rays. The lower the energy with this type of interaction the more scattering that will occur. Secondary electrons are electrons that are ejected from the specimen during inelastic scattering. Generally all electrons with energy values less than 50 eV can be assumed to be secondary electrons.[40] Using both a secondary electron and a back-scattered electron detector will allow for the topography and the composition of a specimen to be determined. In this work the morphology of $(GaN)_{1-x}(ZnO)_x$ samples produced from various precursors was determined via SEM

imaging. Morphology can play a large role in the effectiveness of a material to split water due to surface area affects.

1.6.5 Transmission electron microscopy

Differing from a scanning electron microscope, a transmission electron microscope, or TEM, can produce an image by going through the thickness of a material. The image produced is 2D, unlike a 3D SEM image. A 3D image can offer much more insight into the morphology of a sample, however a scanning electron microscope can only project an image of the surface of a material. Because of its ability to transmit electrons through a sample, a TEM can provide crystallographic information in the form of diffraction patterns. This allows for individual particles to be studied in depth. The determination of whether the specimen is crystalline, along with determining different crystallographic phases, and even orientation with respect to the electron beam are made possible through TEM imaging.[41] The use of both SEM and TEM images can provide the morphology and crystallographic information of a material.

Another type of electron microscopy, STEM, or scanning transmission electron microscopy, is useful for imaging surfaces at the atomic level. In this type of analysis electrons pass through a thin sample. The electron beam is focused into a narrow spot and is scanned across the sample. Using a STEM along with a high-angle detector allows for atomic resolution images to be created. The images show contrast that is directly related to atomic number.[41]

The illumination system is the same in a TEM as in a SEM. It consists of electron guns, a column with an optic axis through the middle, and a set of lenses with focusing. Unlike in a SEM, the object in a TEM is placed between the condenser and objective lens, as can be seen in Figure 1.12. In an SEM the electron beam must pass through all of the lenses before it hits the specimen yet in a TEM, the

electron beam passes through the sample to the objective lens where the electrons are then dispersed to make a diffraction pattern. The electrons are then recombined to form an image.[41]

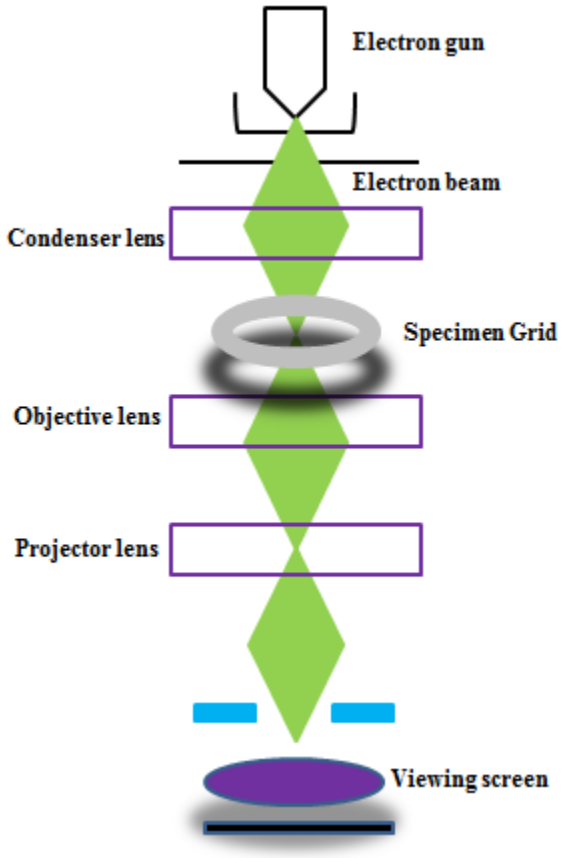

Figure 1.12. Components of a transmission electron microscope.

During an experiment, the electron beam can either be dispersed to form a diffraction pattern or recombined to form an image. The image is highly dependent on sample preparation, and very thin samples are required to produce a good image.[39] Diffraction in a TEM experiment follows the same conventions as in powder diffraction as explained earlier, however there are differences between scattering electrons and x-rays. It is important to remember that electrons have shorter wavelengths than the x-rays used in a laboratory. Electrons also scatter more strongly because they interact with the nucleus and the electrons of the scattering atoms. Instead of producing a plot of 2θ versus intensity, a reciprocal lattice of spots is produced. A reciprocal lattice is a mathematical construction that takes a

set of planes and projects them in reciprocal space through a single point. The Ewald sphere, a 3D depiction of Bragg's law, has a radius of $1/\lambda$ and always passes through the point O in the reciprocal lattice. O corresponds to the spot where the direct beam hits.[41] According to selection rules, different space groups will have different allowed and forbidden reflections. The points where the Ewald sphere touch will produce corresponding spots, and by combining these spots with selection rules, the crystallographic information of the specimen can be analyzed. TEM allows for crystal defects including stacking faults, grain boundaries, and dislocations to be seen directly using methods such as STEM which shows contrast differences in imaging.[41] This is an invaluable tool for getting an almost atomic scale look at the structure of particular particles in a sample. This is important for studies of $(GaN)_{1-x}(ZnO)_x$ as defects can have large effects on a number of properties important for materials used in solar water splitting.

1.6.6 Thermogravimetric analysis

Thermogravimetric analysis measures changes in weight of a sample as a function of temperature under certain gas flow conditions.[39] A TGA consists of a small sample pan supported by a precise balance. Sample size is often in the range of 2 to 50mg. The sample pan is found inside of a furnace that can be either heated or cooled during the experiment. A clean reference pan is held inside of a sealed chamber to allow for proper weight measurements and for a zero wt% starting point to be determined prior to heating. Heating rate, experimental method, and the type of gas flow are all very important and sample dependent. Isotherms, or temperature holds for extended periods of time are necessary for temperature stabilization at pertinent temperatures. These can also allow for corrections to buoyancy to be made if identical isotherms are held before and after the reaction takes place. These experiments can help determine if intermediate compounds are formed during a particular experiment, if water is trapped in a sample, for compositional calculations, and a number of other analyses. For the purposes of this work, TGA studies are conducted in O_2 gas to allow for full oxidation of samples at

high temperatures. Calculations are performed to determine the original amount of nitrogen in samples as a form of sample composition analysis.

1.6.7 Diffuse reflectance spectroscopy

Diffuse reflectance is described as the reflection of light from a surface that is uneven or made up of grains so that the incident rays are deflected off the surface at a number of different angles. If the surface is flat the rays will be reflected and spread evenly over the hemisphere surrounding the surface. Only the part of the beam that is scattered within the sample and reflected back to the surface is considered to be diffuse reflection. The diffusely scattered light is collected and directed to the detector's optics in order to create a spectrum. Reducing the particle size, avoiding sample dilution, and synthesizing a homogeneous sample are all factors that can increase the quality of the spectrum produced.

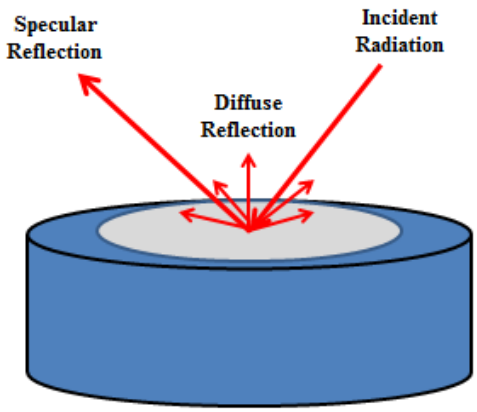

Figure 1.13. Depiction of diffuse reflection.

Analysis of diffuse reflectance data involves plots of reflectance versus wavelength in nm. For this research, the determination of the band edge of materials is crucial and requires the use of the Kubelka-Munk theory with diffuse reflectance data. The Kubelka-Munk theory has been widely used to

relate the total diffuse reflection from a material to its scattering and absorption.[42] A raw diffuse reflectance spectrum will have stronger than expected absorption from weak IR bands. This can be accounted for by using the Kubelka-Munk conversion, where R is the absolute reflectance of the sampled layer, *k* is the molar absorption coefficient, and *s* is the scattering coefficient. It assumes that there is infinite sample dilution, a constant scattering coefficient, and an infinitely thick sample layer, providing the optimal corrections for samples that are highly diluted and have very small particle size. This equation creates a linear relationship for spectral intensity as related to sample concentration.

$$f(R) = (1 - R)^2 / 2R = \alpha / s \qquad (1.7)$$

1.6.8 Solid state nuclear magnetic resonance spectroscopy

Solid state NMR spectroscopy has been shown to be a useful technique for exploring the structure of materials, in particular the local structure surrounding particular atom types. The spectra produced are often very similar in resolution to that of liquid NMR and can actually detect anisotropic interactions, something liquid NMR is unable to do.[43] It is useful for discovering internuclear distances, torsion angles, and even atomic orientations. In molecular solutions an average magnetic field is created which does not occur in solids. To account for this, the solid is spun at a magic angle of 54.44°, which is derived from the equation $3\cos^2\theta-1 = 0$. This magic angle spinning (MAS) gets rid of chemical shift anisotropy which occurs when shielding is created by other nuclei in the sample in solids. The spinning frequency has to be close to the frequency spread of the signal, otherwise spinning side bands are shown, which are separated by the spinning frequency. This is seen in an example of ^{9}Be MAS NMR in Figure 1.14. The effect of frequency on peak intensity is also observed in this image. Specific techniques used in this study, and previous studies on GaN, include ^{1}H, ^{15}N, and ^{17}Ga solid state NMR. Solid-state ^{1}H NMR allows for a clear distinction to be made between structural protons and protons on the surface of a sample.[44] ^{15}N and ^{17}Ga NMR spectra will allow for the local environment around each nitrogen and gallium atom to be discovered.

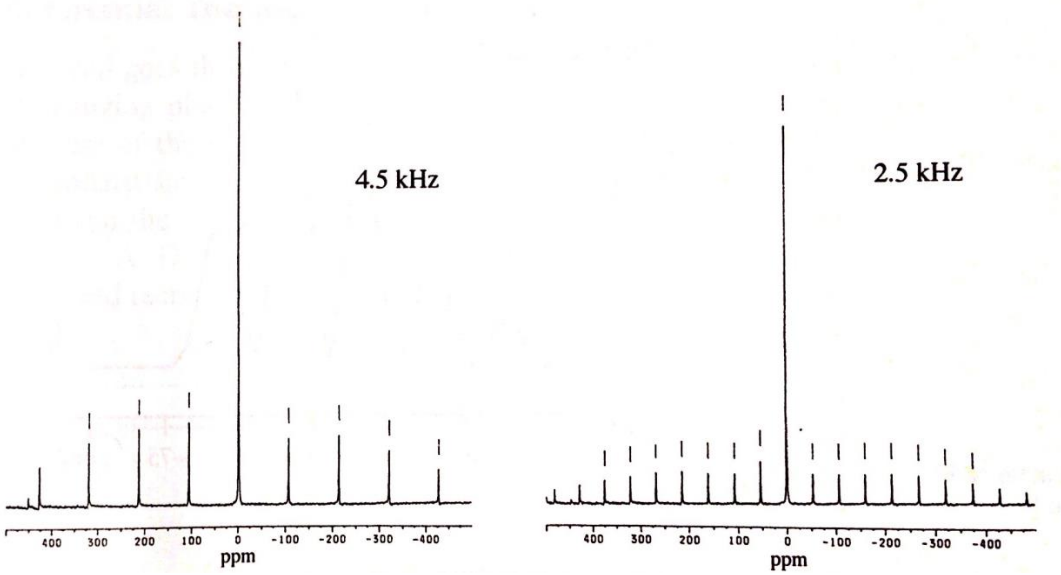

Figure 1.14. ^{9}Be MAS NMR at 4.5kHz and 2.5kHz.[39]

1.6.9 Pair distribution function analysis

Complex materials often show deviations in local structure as compared to their average structure. As was discussed earlier in the diffraction sections, Bragg's law is the foundation for crystallography. It allows a crystal with thousands and thousands of atoms to be described due to translational symmetry based on lattice symmetry and expected diffraction positions in a small unit cell. In reality, there most likely exist a number of small deviations from these positions, and Bragg's law cannot account for these differences in periodicity. For materials such as glasses and liquids, it is impossible to describe the structure via Bragg diffraction alone, but analyzing the relative positions of an atom relative to another can be analyzed. This sometimes can be more important that specific atom positions, especially on a local scale, because it is from these interactions and local displacements of atoms that changes in properties of the material occur. The relative atomic positions can be described as a set of interatomic distances, r_{vu} where v and u are individual atoms. The distribution of these interatomic distances is given by the atomic pair density function, $\rho(r)$. The function $g(r)$ is the atomic

pair distribution function, or PDF. This PDF is a one-dimensional function that shows peaks at distances of $r_{vu} = |r_v - r_u|$. All atoms in the sample are taken into account, providing a plot of all of the atom-atom distances in the solid (out to the distance that is the threshold of the instrument). ρ_0 is the number density of atoms in a system of N atoms and δ is a Dirac delta function.[45] This $\rho(r)$ function can provide information such as how many neighbors an atom has in its local environment and how far away their neighbors are.

$$\rho(r) = \rho_0 g(r) = \frac{1}{4\pi N r^2} \sum_v \sum_u \boldsymbol{\delta}(\boldsymbol{r} - \boldsymbol{r_{vu}}) \quad (1.8)$$

The equivalent to the above function in reciprocal space is known as the S(Q) or the total scattering function. With $|Q| = \frac{4\pi sin\theta}{\lambda}$, the range in Q is limited depending on the instrument wavelength. Cu K_α radiation with a wavelength of 1.54Å would limit the Q range to $8Å^{-1}$.[45] Total scattering takes into account the intensity in scattering from Bragg peaks from the global structure and diffuse scattering from the local structure. Diffuse scattering is the information between the Bragg peaks and is often hard to measure. It is in this diffuse scattering that information regarding local deviations from the average structure reside.[45] For this work PDF studies are used in order to look at differences between the local structure and average crystallographic structure of alloys of GaN and ZnO. Particular, separately determined, Ga-N, or Zn-O distances are not known as a composition of *x*. PDF studies allow for particular nearest neighbor bond distances to be determined.

Chapter 2

Synthesis and Characterization of Visible Light Absorbing $(GaN)_{1-x}(ZnO)_x$ Semiconductor Nanorods

2.1 Introduction to high zinc content precursor $Ga_2O_3(ZnO)_{16}$ for $(GaN)_{1-x}(ZnO)_x$ synthesis

A number of attempts have been made to improve the photoactivity of $(GaN)_{1-x}(ZnO)_x$ through new synthetic methods. As was shown through DFT calculations,[26,46] it is imperative to be able to synthesize high zinc content samples in order to achieve the lowest band gaps in this system. The difficulty with achieving high zinc contents however is from the ease of volatilization of zinc at high temperatures and in a reducing atmosphere. As can be seen in Figure 2.1, zinc volatilization causes unwanted reactions with quartz reaction tubes and careful reaction conditions are necessary for limiting this effect. The most Zn-rich samples prepared from binary oxides had a Zn content of $x = 0.42$.[46] High pressure synthesis was shown to be successful in producing $(GaN)_{1-x}(ZnO)_x$ with $x = 0.50$ and 0.75.[30] However, the restricted volume in high pressure syntheses has severely limited sample sizes and degree to which reaction products could be characterized.

More recently, solution methods have been utilized to prepare a Ga-Zn-O layered double hydroxide route that can be used as a precursor to produce Zn-rich samples with x values of about 0.5-0.8, and band gaps that decreased from 2.6 to 2.35 eV with increasing Zn content.[31] These appeared to form porous particles without well-defined facets that maintained the overall shape of the precursor crystallites. This is consistent with prior work which determined that in reactions between Ga_2O_3 and ZnO, the particle size of the products depends closely on the particle size of the ZnO reactant.[32] The use of nanoscale $ZnGa_2O_4$ and ZnO precursors has also produced Zn-rich samples with x values of about 0.30-0.87, and band gaps that decreased from 2.7 to 2.2 eV. This route produced single-crystalline particles with the use of a lower nitridation temperature (650°C) that used in bulk syntheses (850°C).[33]

In other studies, it was observed that the spinel compound $ZnGa_2O_4$ makes a very effective precursor for the synthesis of $(GaN)_{1-x}(ZnO)_x$ because of the premixing of Ga and Zn on an atomic scale.[47,30] In this work, we have explored the use of alternative Ga-Zn-O precursors which are substantially more Zn-rich than $ZnGa_2O_4$. In particular, the m = 16 member of the $Ga_2O_3(ZnO)_m$ homologous series has been found to enable the synthesis of well-crystallized $(GaN)_{1-x}(ZnO)_x$ nanorods with high Zn contents and band gaps that are small relative to compounds prepared simply using a $ZnGa_2O_4$ spinel precursor.

Figure 2.1. Effects of zinc volatilization on reaction apparatus components.

There are a number of closely related homologous series with generic formulas of $A_2O_3(BO)_m$, where A = In, Fe, Ga and B = Fe, Zn,[48,49] among which the $In_2O_3(ZnO)_m$ compounds have been shown to be effective photocatalysts.[48] In $Ga_2O_3(ZnO)_m$,[50] variable width $(ZnO)_m$ layers form a block that closely approximates the wurtzite structure of ZnO,[51] as can be seen in Figure 2.2 for the structure of the m = 6 member,[50] the only compounds whose full structure has been solved. This makes them candidates for a facile, rapid, and potentially even topotactic transformation to wurtzite-type $(GaN)_{1-x}(ZnO)_x$ via high temperature treatment with ammonia. However, the crystallography of these phases is quite complex. The specific values of m which have been observed to form discrete phases are 6, 7, 8, 9, and 16. Extremely large unit cells have been reported on the basis of prior single crystal diffraction studies, and the diffraction patterns that result from the various stacking variants are all quite similar to each other and to the parent wurtzite phase ($m = \infty$) because of their close structural relationship. It has been suggested that the symmetry of these compounds can most appropriately be described with a commensurately modulated superspace group.[50] Prior syntheses of these compounds were accomplished using platinum crucibles and very high temperatures at which Zn is easily volatilized and

lost, and improvements on these synthetic procedures are necessary before the $Ga_2O_3(ZnO)_m$ phases can be effectively used as a precursor for the synthesis of bulk quantities of $(GaN)_{1-x}(ZnO)_x$.

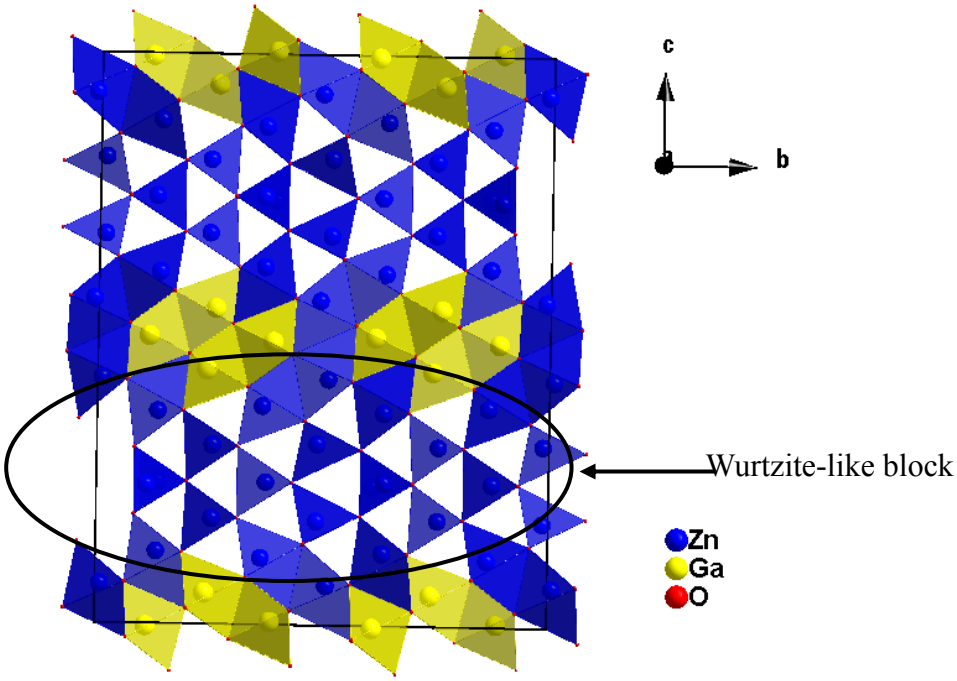

Figure 2.2. Orthorhombic structure of $Ga_2O_3(ZnO)_6$. Bond valence sum calculations using previously determined atomic positions[50] were used to assign crystallographic sites to either Ga or Zn.

2.2 Experimental

2.2.1 Synthesis

$Ga_2O_3(ZnO)_m$ phases were carried out by mixing stoichiometric amounts of Ga_2O_3 (Alfa Aesar, 99.999%) and ZnO (Alfa Aesar, 99.99%), grinding with an agate mortar and pestle, and placing the mixture in a dense alumina crucible (CoorsTek). The m = 16 phase used as a precursor for $(GaN)_{1-x}(ZnO)_x$ syntheses was obtained by reacting stoichiometric amounts of Ga_2O_3 and ZnO (1:16) in a sealed alumina tube held at 1350 °C (1623 K) under flowing oxygen (~60 ml / min) for a total of 144 h with intermediate grinding steps every 48 h to promote reactivity and product homogeneity. Conversion of the $Ga_2O_3(ZnO)_{16}$ precursor into a wurtzite oxynitride was typically done at 1123 K

under NH_3 flow (5ml/min) for times of 10-18h, resulting in single phase wurtzite samples with varying zinc contents. After heating, the sample was cooled to room temperature under NH_3 flow and the tube was then purged with N_2 gas prior to sample removal.

2.2.2 X-ray powder diffraction

Progression of reactions was monitored using X-ray powder diffraction on a Bruker D8 Advance laboratory diffractometer (Cu K_α λ = 1.54059Å, 7-120° 2θ, 0.02 step size, 300 mm radius, 12mm variable slits, 2.5º Soller slits and a 192-channel Lynx-Eye 1D position sensitive Si detector). Scans for phase identification were done at a rate of 0.1s/step (19.2 s/point) while data suitable for Rietveld refinement were collected using a scan rate of 3 s/step (576 s/point). Zero background silicon slides were used as sample holders. The JADE software package (Materials Data, Inc.) was used for preliminary unit cell refinements and for phase identification. Rietveld refinements were carried using TOPAS v4.2 (Bruker AXS)

2.2.3 Scanning Electron Microscopy

Sample morphology and size were determined by scanning electron microscopy (SEM, LEO Gemini 1550, RBSD). Powder samples were mounted on circular aluminum standard sample studs using carbon double sided conductive tape. Images were taken at magnifications ranging from 300X to 100,000X using a 20kV accelerating voltage and a working distance of 10mm.

2.2.4 Diffuse Reflectance Spectroscopy

Optical properties of samples were measured using ultraviolet-visible diffuse reflectance spectroscopy (uv-vis DRS; PerkinElmer Lambda950). Powder samples were loaded into a cylindrical powder holder with a circular quartz window 16.60 mm in diameter and 1.50mm thick. A scan range of 200 – 1000 nm (6.20 – 1.24eV with a detector change at 860.80 nm and a lamp change at 319.20nm)

was used with a data interval of 1.30 nm and a scan rate of 182.25 nm/min and a $BaSO_4$ (Alfa Aesar, 99.998%) 100% reflectance standard.

2.2.5 Thermogravimetric Analysis

Thermogravimetric Analysis (TGA; Q500 or Q5000 system from TA Instruments) was used to determine the nitrogen content in samples. Alumina sample holders (100 μL) were used for powder sample masses of 10-20 mg, which were heated under a constant flow of O_2 (25 ml/min) and held at room temperature for at least one hour before ramping in temperature to allow for gas flow stabilization. A constant ramp rate of 5 °C/min was used with holds at both 250 °C (4 h) and 950 °C (6 h). Mass loss determinations were made by comparing masses at 250 °C upon heating and cooling, allowing buoyancy errors to be avoided.

2.2.6 Transmission Electron Microscopy

Transmission electron microscopy experiments were performed in an FEI Titan 80-300 microscope equipped with a CEOS third order image aberration corrector and dedicated environmental gas cell. All high-resolution images were collected with a residual spherical aberration value of -2 microns, and recorded on a Gatan Ultrascan 1000 CCD detector. Tomographic data were collected in STEM mode with a probe convergence semiangle of 9 mrad and a detector collection range of 35-65 mrad. The differential pumping apertures of the environmental cell prevented collection angles of greater than 65 mrad. Tomography data was collected in 1 deg steps from -65 to +65 deg. Three-dimensional images were reconstructed using the FEI Inspect3D software using the simultaneous iterative reconstruction technique (SIRT) algorithm. All data acquisition and analysis was completed by Dr. James Ciston at the CFN, Brookhaven National Laboratory.

2.3 Results and Discussion

2.3.1 Synthesis of $Ga_2O_3(ZnO)_m$ precursor phases

Although the potential utility of $Ga_2O_3(ZnO)_m$ to the synthesis of Zn-rich $(GaN)_{1-x}(ZnO)_x$ semiconductors is clear, prior literature synthesis routes for these layered wurtzite-related phases had the major disadvantage of requiring very high temperatures (1350-1650 °C) with Pt crucibles.[52] The high synthesis temperatures are particularly problematic as they can strongly promote the reduction of ZnO to Zn metal and the resulting rapid evaporation of Zn metal. Reactions to produce $Ga_2O_3(ZnO)_m$ were therefore carried out under flowing oxygen, which was effective in limiting the loss of Zn. The use of large sample masses (typically 20 grams) and mostly-filled cylindrical crucibles minimized the surface area to volume ratio and allowed the net mass loss due to evaporation over the course of the reaction to be limited to about 0.2%. The Ga-Zn-O phase diagram was explored in a coarse fashion to enable the minimal synthesis temperatures for various $Ga_2O_3(ZnO)_m$ to be identified and an approximate phase diagram to be constructed. Figure 2.3 shows that the only ternary phase stable at modest temperatures (<1200 °C) is the $ZnGa_2O_4$ spinel, and that the layered $Ga_2O_3(ZnO)_m$ phases first are observed at temperatures of 1300 °C or higher. The m = 16 layered phase with the largest wurtzite blocks is the only layered compound observed at 1300 °C, and successively higher temperatures are required to produce phases with smaller wurtzite blocks.

At 1300°C, reaction times of a week or longer are typically required to obtain a homogenous product. The X-ray diffraction pattern of a typical reaction product is shown in Figure 2.4, with marked peak positions expected for the literature orthorhombic unit cell (a = 3.25, b = 19.76, c = 54.208Å). It should be noted that X-ray diffraction patterns could not confirm that the $Ga_2O_3(ZnO)_{16}$ samples were single phase since the crystal structure has not yet been solved and refined. The pattern analysis is made more challenging since the m = 16 pattern inherently has a tremendous degree of peak overlap due to its large unit cell, has great similarity between the periodicities along different axes due to its close relationship with the wurtzite subcell, has a very large degree of peak overlap with other $Ga_2O_3(ZnO)_m$ phases, and has a structure which is likely conducive to the formation of stacking faults. It also appears

that these phases are best described in terms of modulated structures that require more than three dimensions to be accurately indexed. As a result, reactions were judged to be complete when X-ray patterns no longer showed any evidence of starting materials or the spinel phase. The ability to synthesize $Ga_2O_3(ZnO)_m$ phases at temperatures lower than previously reported allowed the reactions to be carried out in alumina crucibles rather than in the more expensive Pt vessels used previously.

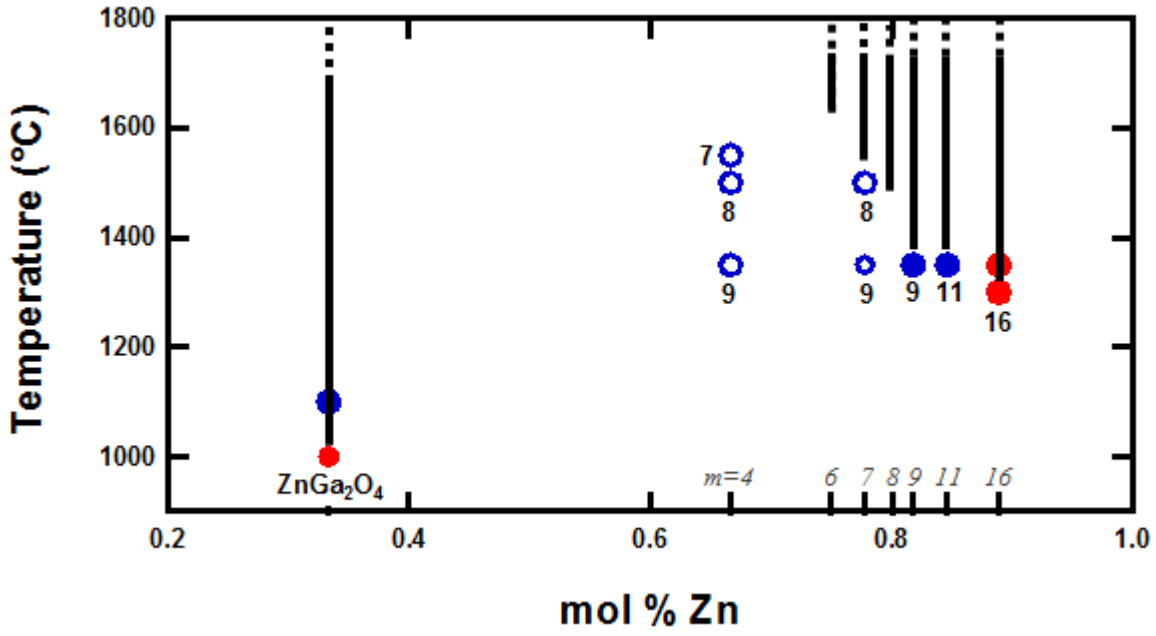

Figure 2.3. ZnO-Ga_2O_3 partial phase diagram. Closed circles represent single phase products and open circles represent multiphase samples containing $ZnGa_2O_4$ and a layered phase whose m value is indicated. No symbol is shown for the m=6 phase which was prepared as a single crystal at 1650 °C without information about secondary phases. Red symbols denote samples synthesized in this work while blue symbols represent data from Kimizuka et al.[53,52] or Phani et al.[54]

The production of $(GaN)_{1-x}(ZnO)_x$ is typically accomplished by nitridation (high temperature treatment under flowing NH_3 gas) of precursors.[55] While this wurtzite phase was originally produced by the nitridation of Ga_2O_3 and ZnO mixtures,[55] it was later understood that these (and related precursors) typically quickly react to form the spinel compound $ZnGa_2O_4$, which then converts to wurtzite $(GaN)_{1-x}(ZnO)_x$ over a longer time scale.[56,57] It was later found that the nitridation of a $ZnGa_2O_4$ precursor will lead to products with very good photoactivity, perhaps facilitated by the fact that this compound has Ga

and Zn homogenously mixed on an atomic scale. The spinel composition can at most lead to $(GaN)_{1-x}(ZnO)_x$ with a cation mole fraction of Zn of x = 0.33, though the actual Zn content obtained in experiments was found to typically correspond to x values of 0.05-0.22[56,58] due to the facile loss of Zn through the mechanism of reduction to its metallic form followed by evaporation.

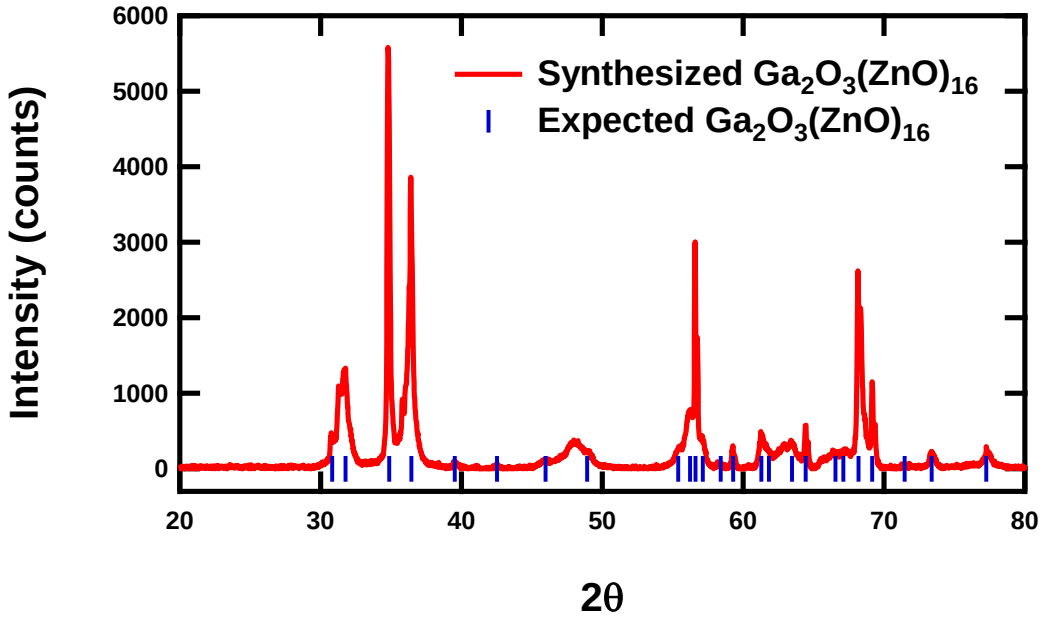

Figure 2.4. Powder XRD pattern of fully-reacted $Ga_2O_3(ZnO)_{16}$. Selected peak positions expected for the literature unit cell without considering systematic absences are marked below the pattern.

The use of a $Ga_2O_3(ZnO)_{16}$ precursor in nitridation reactions offers the same advantage of premixed Ga and Zn atoms as the spinel phase, but offers the potential to produce $(GaN)_{1-x}(ZnO)_x$ products which are Zn-rich and are therefore likely to have reduced band gaps and potentially better photoactivity for water splitting. The cation mole fraction of Zn is x = 0.89 for the m = 16 layered compound, and remains large even for the m = 6 compound which has x = 0.75. Further control over the Zn content of $(GaN)_{1-x}(ZnO)_x$ produced by nitridation reactions using a $Ga_2O_3(ZnO)_{16}$ precursor can be achieved by varying the reaction time, temperature profile, NH_3 flow rate, or any other parameter which influences the amount of Zn evaporation. About ten important variables that influence Zn content were identified in experiments. In order to achieve the best reaction reproducibility and the greatest

reduction of parameter space, all reaction parameters except for the reaction time and NH_3 flow rate were kept constant to the furthest extent possible. Due to the facile loss of Zn from $(GaN)_{1-x}(ZnO)_x$ phases, it was never possible to reach chemical equilibrium at the nitridation reaction temperature of 850 °C. However, single phase products with wurtzite X-ray diffraction patterns could be achieved (Figure 2.5). The substantial variation in the $(GaN)_{1-x}(ZnO)_x$ lattice parameters indicated that products with a wide range of Zn contents could be produced, and that high Zn contents were accessed.

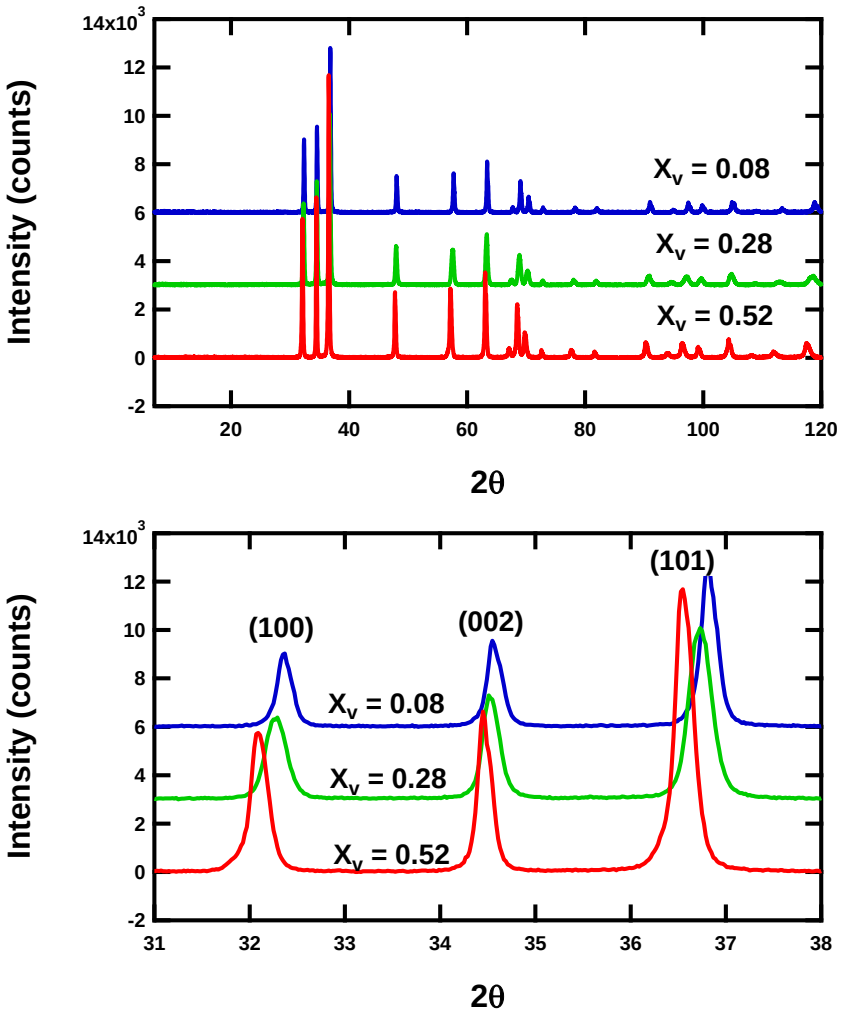

Figure 2.5. XRD patterns of $(GaN)_{1-x}(ZnO)_x$ produced from $Ga_2O_3(ZnO)_{16}$ precursor along with a zoomed image of prominent wurtzite peaks labeled with their Miller indices. Successive patterns are offset by 3000 counts/pattern in intensity for clarity.

The accurate determination of the composition of $(GaN)_{1-x}(ZnO)_x$ wurtzite phases poses a significant challenge, especially when large numbers of samples are being screened. The use of energy dispersive X-ray spectroscopy (EDX) in a SEM microscope has been utilized in the past, but high accuracy with this technique is only achieved for flat samples (*ie* thin films, single crystals) and powder samples can routinely have errors in *x* of +/- 0.05 or worse. Furthermore, EDX will only be sensitive to Ga:Zn ratios as the light elements N and O cannot be accurately quantified by this method. In this study, a combination of TGA (to determine the N content) and quantitative phase analysis (QPA) by Rietveld refinement (to determine the Ga and Zn contents) were utilized to obtain accurate insights into $(GaN)_{1-x}(ZnO)_x$ stoichiometries in a manner which will be discussed more later. However, a more rapid compositional assessment that was used to provide precise and reproducible results was the Vegard's law analysis of the wurtzite *a*-lattice parameter. The relationship:

$$a = 3.189 + 0.06\, x_v \qquad (2.1)$$

was used to estimate a *nominal* Zn cation mole fraction, which will be denoted x_v, based on the assumption of a linear variation in the wurtzite *a*-lattice parameters between that of the end members of GaN ($x = 0$, $a = 3.189$) and ZnO ($x = 1$, $a = 3.249$). The high quality X-ray diffraction data allowed x_v to be determined with a precision of about 0.01. The accuracy of this method is not known absolutely, but based on analogies with other semiconductor systems it is expected that the *a*-lattice parameter increases monotonically with increasing Zn content and that an accuracy of about 0.05 in x_v will be achieved since there is no reason to expect strong bowing or other large deviations from Vegard's Law (linear change in lattice parameters with substitution) for the *a*-lattice parameter. As can be seen in Figure 2.5, there are about 20 discernible wurtzite X-ray diffraction peaks in a scan range of 7 – 120° 2θ, and that the peak shifts are large relative to the instrumental precision (~0.01° 2θ) even for the low angle peaks (30 – 40° 2θ) which are the least sensitive to lattice parameter changes, as can be seen in Figure 2.5.

2.3.2. Composition Determination

By following the mass change that occurs during oxidation, the nitrogen content of $(GaN)_{1-x}(ZnO)_x$ samples could be determined in TGA experiments. On heating, 1.5 atoms of O are needed to replace each N atom, giving rise to an expected mass gain of +11.93% when GaN is fully oxidized to Ga_2O_3, and a proportionally smaller mass change for $(GaN)_{1-x}(ZnO)_x$ samples with $x > 0$. The oxidation of GaN samples produced a mass change of 11.67%, slightly lower than the expected value. This could potentially be due to kinetic limitations as the decomposition of GaN took a long time to complete (>12 hrs at 950 °C) and did not show a clear plateau at 950 °C, unlike Zn-containing $(GaN)_{1-x}(ZnO)_x$ samples which were universally observed to be fully decomposed by the time the temperature ramp up to 950 °C was complete. The $x_v = 0.08$ sample was calculated to have an anion content of 82 mole % nitrogen and the balance was attributed to oxygen ($\chi_O = 18\%$), while the $x_v = 0.28$ and $x_v = 0.52$ samples were calculated to have $\chi_O = 30\%$ and 53% oxygen, respectively, as summarized in Table 2.1.

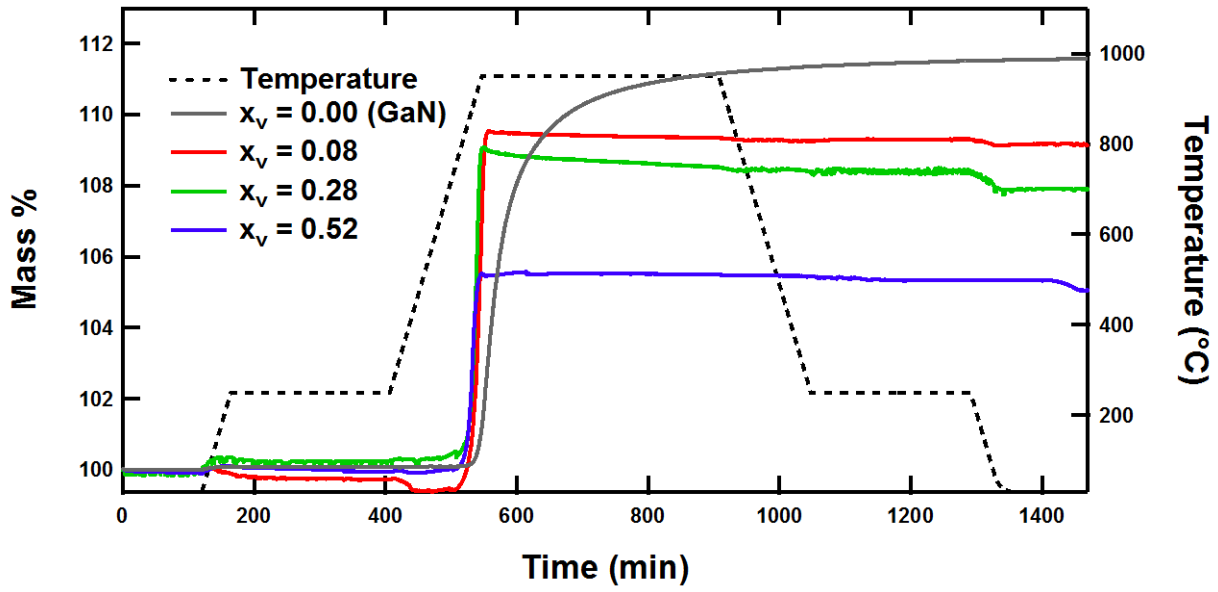

Figure 2.6. Mass changes observed during oxidation of $(GaN)_{1-x}(ZnO)_x$. GaN was synthesized by nitriding Ga metal.

Further compositional information could be obtained by collecting X-ray diffraction patterns of the TGA decomposition products and carrying out quantitative phase analysis (QPA) by Rietveld refinement to determine the cation mole fraction of Zn and Ga. The TGA decomposition products that resulted from heating in flowing O_2 at 950 °C were a mixture of wurtzite ZnO, spinel $ZnGa_2O_4$, and monoclinic β-Ga_2O_3 in a manner generally consistent with the expected phase behavior of this system ($ZnGa_2O_4$ + β-Ga_2O_3 for samples with $x < 1/3$; $ZnGa_2O_4$ + ZnO for samples with $x > 1/3$). The Zn mole fraction (χ_{Zn}) was then determined from the ratio of products from the corresponding Rietveld refinements, reported in Table 2.1. This experimentally calculated Zn mole fraction was then compared to the Vegard's law approximation of Zn content (x_v) used to label samples.

Table 2.1. Compositional analysis: Zn content from Rietveld refinements of TGA products and O content from TGA.

	Phase content from QPA (mass %)			Ion fraction (mole %) by QPA(χ_{Zn}), TGA(χ_O)		
x_v	$ZnGa_2O_4$	Ga_2O_3	ZnO	χ_{Zn}	χ_O	R_{wp}
0.08	27.1(3)	72.9(3)	-----	9	18	6.52
0.28	68.1(2)	31.9(3)	-----	23	30	
0.52	71.1(1)	-----	28.9(1)	54	53	

The Zn contents of these samples determined from QPA are near the values estimated by x_v calculations (within 3 mol %). However, a more striking discrepancy can be seen in the oxygen contents of low Zn content samples which are indicative of a Zn:O ratio that is not equimolar. The origin of this non-stoichiometry is tentatively ascribed to wurtzite cation vacancies associated with Ga ions. In particular, it is known that treatment of Ga_2O_3 with NH_3 produces a very defective gallium oxynitride, whose formula has been reported as $Ga_{0.89}\square_{0.11}N_{0.66}O_{0.34}$,[59] while the ZnO lattice does not

readily accommodate defects. Based on the experimentally determined Ga:Zn and N:O ratios, charge neutrality would be achieved with 3% cation vacancies in the $x_v = 0.08$ and $x_v = 0.28$ nanorod samples. It appears that cation defects may be important to understanding and improving the performance of wurtzite $(GaN)_{1-x}(ZnO)_x$ semiconductors, and further studies on these defects are in progress.

2.3.3. Spectroscopic Investigation of Band Structure

It has previously been reported that an increase in zinc content results in improved visible light absorption for $(GaN)_{1-x}(ZnO)_x$ samples with modest Zn contents ($x \leq 0.42$),[55,60] and this trend has more recently been seen to extend to Zn-rich samples.[56,61] The optical properties of nanorod $(GaN)_{1-x}(ZnO)_x$ samples prepared using a $Ga_2O_3(ZnO)_{16}$ precursor were determined by diffuse reflectance studies (Figure 2.7). The relative absorbance (α_{KM}) obtained from a Kubelka-Munk transform of the reflectance data showed increasing visible light absorption with increasing Zn content ($x_v \leq 0.55$), and similar behavior was observed for the band gaps (E_g) calculated from quantitative fits to the functional form expected for direct band gap absorption (Table 2.2).

The UV-vis optical response of $(GaN)_{1-x}(ZnO)_x$ has three characteristic regions, as shown in a representative fit for the $x_v = 0.55$ sample (Figure 2.8). The absorbance above the band gap of these wurtzite semiconductors was always characteristic of a direct band gap with $\alpha \sim (E\text{-}E_g)^{0.5}$, and an appropriate fitting range (green line) could be determined by looking for a linear region in a plot of $(\alpha E)^2$ vs. E. However, this direct band gap scaling was only observed for regions of the spectrum where the absorbance was relatively large ($\alpha/\alpha_{max} > 0.5$) due to the presence of a very strong Urbach tail (red line), which resulted in substantial broadening of the onset of absorption and substantial absorption at sub-band gap energies. The Urbach-type absorption was fit using the functional form $\alpha = Ae^{(E - E\_g)/E\_U}$ where E_U is the Urbach energy that describes the breadth of the optical transition. This unusually large Urbach broadening was observed for all samples and is expected to reflect either compositional inhomogeneity (bulk or locally) or the influence of a large concentration of defects.

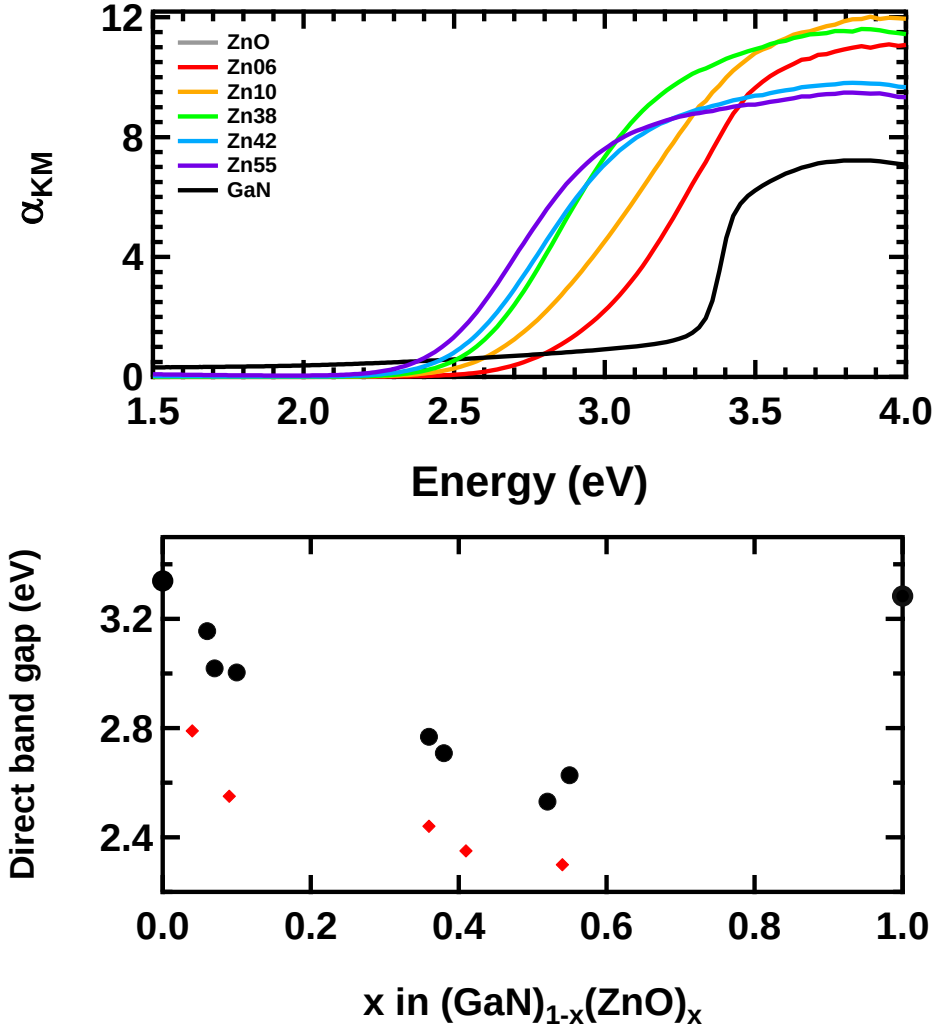

Figure 2.7. Top: Relative absorption spectra of $(GaN)_{1-x}(ZnO)_x$ samples with $x_v \leq 0.55$ obtained by nitriding a $Ga_2O_3(ZnO)_{16}$ precursor under a flow of NH_3 at 850°C for varying times. Bottom: Direct band gap energy of $(GaN)_{1-x}(ZnO)_x$ as a function of x_v [large circles]. Band edge energies determined from linear extrapolatioin are indicated with small diamonds.

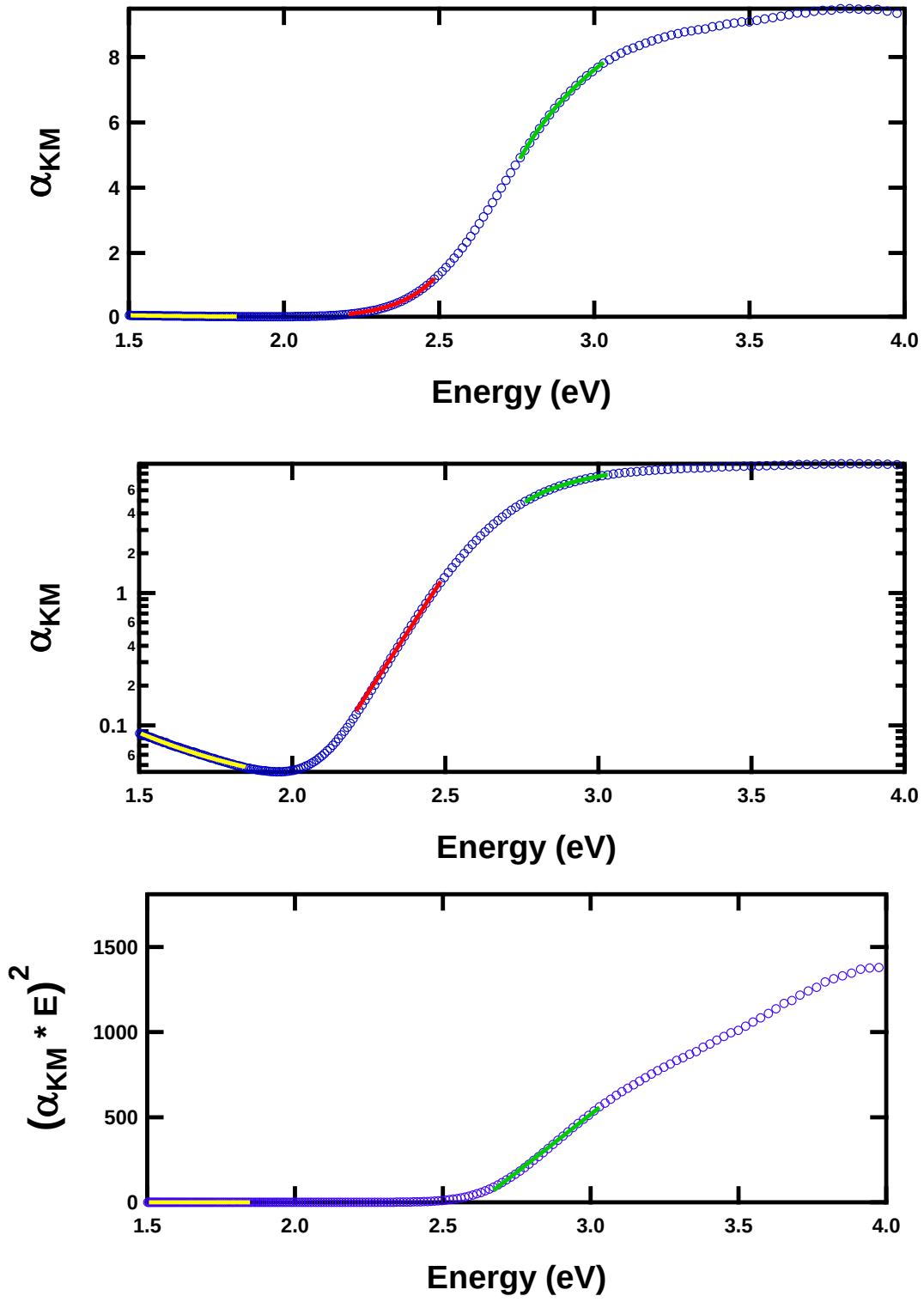

Figure 2.8. Optical response of $(GaN)_{1-x}(ZnO)_x$ $x_v = 0.55$ with the Kubleka-Munk-derived absorption scaled in three different manners to emphasize the regions where the absorbance is dominated by the direct band gap transitions (green line), the Urbach tail (red line), or free carrier absorption (yellow line).

Band gaps as low as 2.53 eV were observed for samples with the highest Zn contents, indicating that a substantial portion of the visible light spectrum can be absorbed by these nanorods. The optical data is generally consistent with those for samples prepared using other methods, though it should be noted that past literature has often used assessments of the band edge as a substitute for a proper band gap determination. The band edge is conventionally obtained by linearly extrapolating absorption to zero on a plot of α as a function of wavelength. Since this does not represent a proper functional form for light absorption, the band edge energy will necessarily differ from the band gap energy. For semiconductors like ZnO which have a sharp onset of absorption, this difference is typically small (< 0.05 eV). Differences are exaggerated for semiconductors like $(GaN)_{1-x}(ZnO)_x$ which have a broad onset of absorption, and it was found that the band edge energies (small circles on Figure 2.7) determined for $(GaN)_{1-x}(ZnO)_x$ nanorods were commonly 0.25 eV smaller than their direct band gaps, suggesting that some prior estimates of $(GaN)_{1-x}(ZnO)_x$ band gaps need to be revised upwards.

Table 2.2. Optical analysis: Values of direct band edge and Urbach tail regions from quantitative fits to functional forms of diffuse reflectance data.

x_v	E_g from direct band gap fit	E_U from Urbach tail fit	E_g from Urbach tail fit	Slope of free carrier region (B)
0.06	3.15	0.108	2.39	--
0.10	3.00	0.090	2.41	0.001
0.38	2.77	0.083	2.50	0.037
0.42	2.71	0.090	2.49	0.102
0.55	2.53	0.094	2.43	0.286

A third component of the optical absorption which has not been previously commented on for $(GaN)_{1-x}(ZnO)_x$ semiconductors is the absorption below the band gap which appears approximately linear when α is plotted on a log scale, and therefore substantially increases with decreasing energy (yellow line). We attribute this type of absorption to free carrier absorption, which is well known to be

strongest at low photon energies. It is hypothesized that Zn loss is a major mechanism for the introduction of carriers (previously reported to be holes)[62] into these wurtzite semiconductors, and that cation vacancies (or equivalently, excess anions) may be active in maintaining charge balance. This is consistent with the enhanced activity recently reported to result following the air annealing of $(GaN)_{1-x}(ZnO)_x$ with $x = 0.18$ at 550 °C.[63] The photoactivity of $(GaN)_{1-x}(ZnO)_x$ semiconductors is expected to strongly depend on their carrier concentration (which influences both band bending and the minority carrier diffusion length), and the below-gap optical absorption can potentially provide an easy and direct method for quantifying changes in the carrier concentration of powder samples introduced by physical processes or by chemical substitution.

In the simplest Drude model of free carriers, it is expected that free carrier absorption is proportional to λ^2, though other scaling relationships may be observed if other scattering processes are active, such as the $\lambda^{1.5}$ scaling when lattice vibrations are involved, or ionized impurity scattering which is expected to give either λ^3 or $\lambda^{3.5}$ scaling in different derivations.[64,65,66] Prior measurements on single crystal ZnO samples[67,68] have found λ^3 scaling that is robust over a range of free carrier and impurity concentrations, and have suggested the relationship $n_e = \alpha(E)\ E^3\ (2.24 \times 10^{17}\ cm^{-2}\ eV^{-3})$.[69] This relationship probably cannot be extrapolated to $(GaN)_{1-x}(ZnO)_x$ semiconductors since the proportionality constant relating n_e and $\alpha(E)$ will depend on the impurity concentration, which will be preparation-dependent and which is likely to be significantly different between binary ZnO and complex $(GaN)_{1-x}(ZnO)_x$. It has been shown for single crystal *n*-type germanium semiconductors[66] that absorption scales as either $\alpha(E) = n_e\ (m/m^*)^2\ \lambda^2\ f_e(T)$ for electronic-only scattering or $\alpha(E) = n_e\ N_i\ (m/m^*)^2\ \lambda^3\ f_i(T)$ for impurity scattering, where n_e is the free carrier concentration, N_i is the concentration of ionized impurities, m and m^* are the actual and effective electron masses. The temperature dependence of absorption $f(T)$ is expected to scale as $\tau^2 T$ with the electron scattering lifetime τ for an

electronic-only scattering mechanism, but is expected to be essentially independent of temperature when ionized impurities provide the dominant scattering mechanism.

Fits to the optical absorption of $(GaN)_{1-x}(ZnO)_x$ nanorods below the band gap to a combined Urbach and free carrier response (Figure 2.9, black dashed lines) with

$$\alpha(E) = Ae^{(E-Eg)/EU} + BE^{-3} + C \quad (2.2)$$

show that λ^3 (or equivalently, E^{-3}) scaling very accurately describes the energy dependence of their free carrier absorption, and that there is a very large difference in the absorption of samples with different substitution levels. It is clear that the free carrier absorption is much stronger in samples with high zinc contents, though it is not yet known if this is due to higher carrier concentrations or to higher levels of ionized impurities. Optimal performance for solar water splitting by $(GaN)_{1-x}(ZnO)_x$ nanorods can only be accomplished when both the impurity and carrier concentration are appropriate. Methods for deconvoluting their contributions to absorption that will enable their quantification by optical methods are the subject of ongoing work.

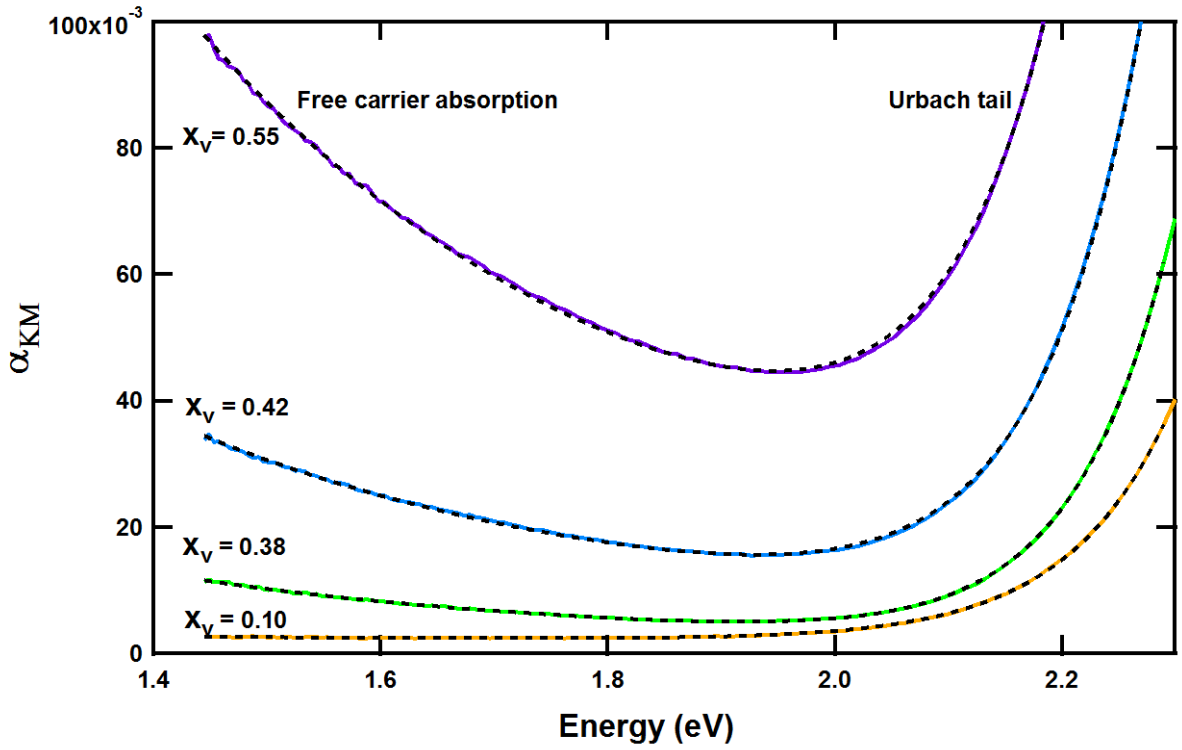

Figure 2.9. Below-band-gap absorption of $(GaN)_{1-x}(ZnO)_x$ relationship for samples with band gaps between 3.00 eV(x_v = 0.10) and 2.53 eV (x_v = 0.55) highlighting the free carrier absorption below 2.0 eV which increases substantially with increasing Zn content. Combined fits to an Urbach tail ($Ae^{(E-Eg)/EU}$), free carrier (BE^3), and baseline offset (C) response are overlaid as dashed black lines for each sample.

2.3.4. Precursor influence on product morphology

It has been previously demonstrated that both the nature of the precursor and the morphology of the precursor can strongly influence the morphology of wurtzite $(GaN)_{1-x}(ZnO)_x$ reaction products.[70] Initial insights were obtained from scanning electron microscopy experiments (Figure 2.10). Both $Ga_2O_3(ZnO)_{16}$ and $ZnGa_2O_4$ precursors were prepared using ZnO and β-Ga_2O_3 binary oxides which were dried in air at 700 °C for 2 hours prior to use. The dried ZnO consisted of particles that approximate 300nm in diameter, while β-Ga_2O_3 has a rod-like morphology and a far larger particle size (rods up to 60 μm in length were visible). After these binary oxides were reacted in O_2 at 1350 °C to form $Ga_2O_3(ZnO)_{16}$ or in air at 1000 °C to form $ZnGa_2O_4$ precursors, poly-dispersed particles were

observed. $Ga_2O_3(ZnO)_{16}$ consisted of agglomerates of particles with typical dimensions of 2 to 20 μm, while $ZnGa_2O_4$ spinel exhibited rod-like particles about 10 μm long.

Despite the comparable dimensions of the $Ga_2O_3(ZnO)_{16}$ and $ZnGa_2O_4$ precursors, the wurtzite reaction products obtained by ammonolysis at 850 °C had completely different morphologies. The cubic spinel precursor gave rise to roughly equiaxial particles about 0.5 μm in thickness, while the layered $Ga_2O_3(ZnO)_{16}$ precursor produced nanorods which were roughly 200 nm in diameter and 5 μm in length. Furthermore, these nanorods could be obtained in a carpet-like assembly with a high degree of alignment prior to dispersal, as seen in Figure 2.11. Two factors are believed to be responsible for promoting nanorod formation. First, the pre-formed wurtzite-like layers in the $Ga_2O_3(ZnO)_{16}$ precursor are believed to serve as directing agents so that the large precursor particles convert in an equivalent manner across their breadth through a pathway that is not available to the highly symmetric cubic spinel phase. Second, a very substantial amount of Zn is lost via evaporation when the $Ga_2O_3(ZnO)_{16}$ precursor converts to wurtzite, and the space between the pillared nanorods represents an organization of the void spaces that result. The needle-like morphology is very desirable for water splitting applications as it permits short diffusion lengths for carriers to access the particle surface, while maintaining a large enough particle size to allow the development of band bending that can provide a driving force for charge separation between the photo-generated electrons and holes. Future comparative tests of the photoactivity of co-catalyst functionalized wurtzite nanorods to samples prepared by other methods will be used to determine if enhanced quantum yields for overall water splitting can be realized.

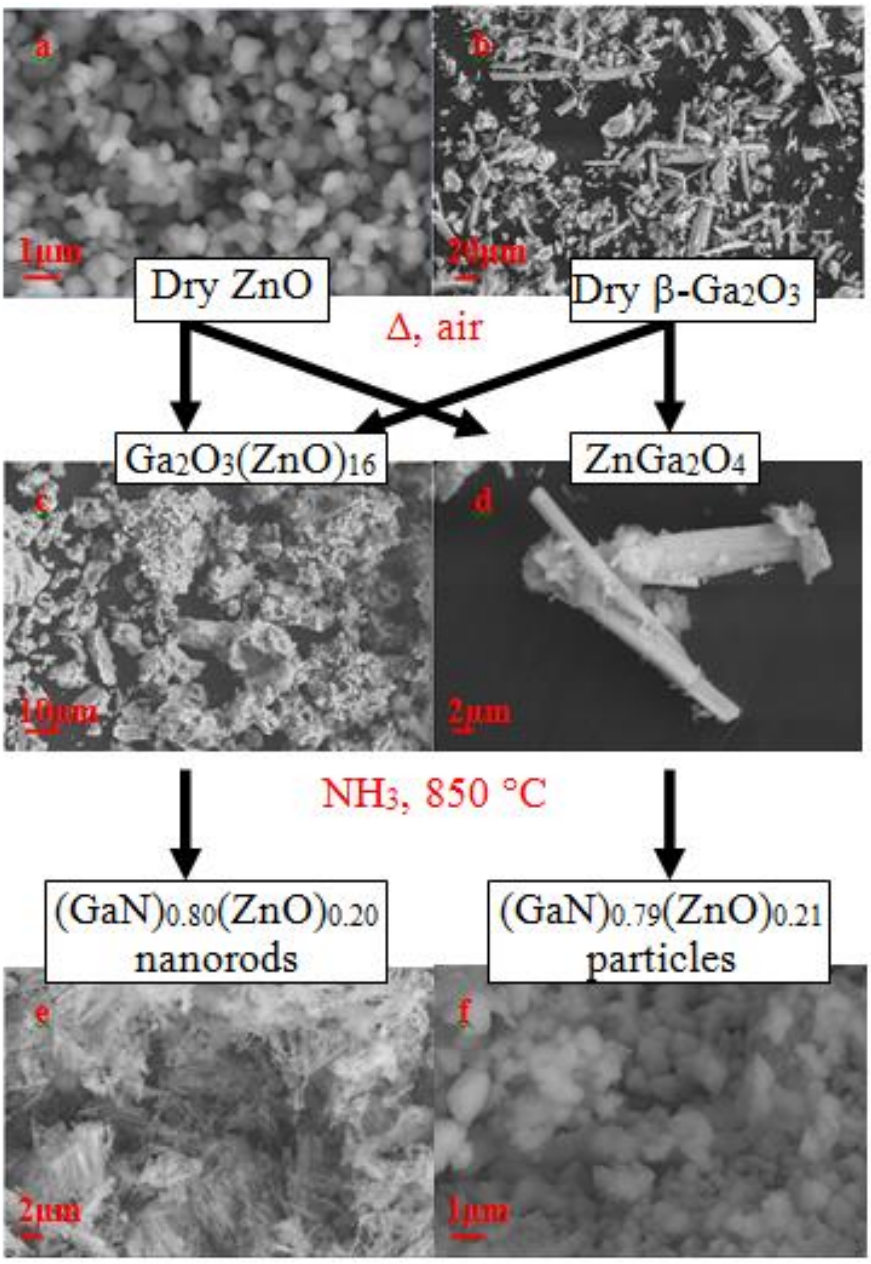

Figure 2.10. SEM images of (a) β-Ga_2O_3 dried at 700°C, (b) ZnO dried at 700°C, (c) $Ga_2O_3(ZnO)_{16}$ synthesized at 1350 °C, (d) $ZnGa_2O_4$ synthesized at 1000°C, (e) $(GaN)_{1-x}(ZnO)_x$ from 2:16 synthesized at 850°C with $x_v = 0.20$, (f) $(GaN)_{1-x}(ZnO)_x$ from $ZnGa_2O_4$ synthesized at 850°C with $x_v = 0.21$.

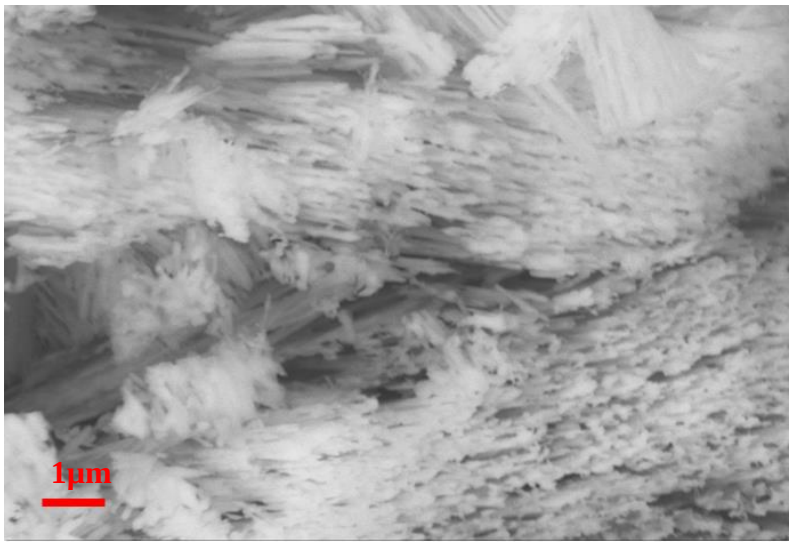

Figure 2.11. The nanorod "carpet" of $(GaN)_{1-x}(ZnO)_x$ with x_v = 0.33 resulting from the nitridation of $Ga_2O_3(ZnO)_{16}$ at 750 °C.

Further morphology studies were carried out using TEM techniques for $(GaN)_{1-x}(ZnO)_x$ samples synthesized from both $Ga_2O_3(ZnO)_{16}$ and $ZnGa_2O_4$ precursors with estimated compositions of x_v = 0.09, 0.21, and 0.54. Consistent with the SEM results, TEM reveals a rod-like morphology of most particles with lengths of 2-6 μm and 100-300 nm widths. It was confirmed by both transmission electron diffraction and high resolution imaging that the non-polar $(1\underline{2}10)$ plane is perpendicular to the long axis of the rod, independent of the Ga/Zn ratio studied. Figure 2.12 shows a series of low resolution and high resolution images and electron diffraction pattern for the x_v = 0.21 $(GaN)_{1-x}(ZnO)_x$ prepared from a $Ga_2O_3(ZnO)_{16}$ precursor, which is representative of the rod morphology for all compositions studied. Extended annealing of the material for over 12 hours resulted in particles of more isotropic shape due to high temperature coarsening, supporting the assertion that kinetic rather than thermodynamic driving forces were responsible for the initial nanorod morphology.

In order to determine the facet of $(GaN)_{1-x}(ZnO)_x$ that is active in solar photochemistry, TEM tomographic studies were carried out on samples prepared using the more common spinel precursor. In addition to being representative of samples whose activities have been studied in depth, the surface

facets for spinel-derived samples are better defined than those of the novel nanorod samples. Tomographic tilt series were collected in medium angle annular dark field Scanning TEM (STEM) mode for three different $(GaN)_{1-x}(ZnO)_x$ particles with $x_v = 0.21$ synthesized from the spinel precursor, and electron diffraction patterns were recorded for selected high symmetry axes. Figure 2.13 shows a selected projection of one of these particles with an accompanying diffraction pattern to determine the facet identities. A tomographic reconstruction was used to distinguish facets viewed in profile from crystal edges viewed obliquely. Using a combination of three dimensional tomographic reconstruction and cross-referenced diffraction data, a total of 22 surface facets from three particles were determined to be of the {10$\underline{1}$1} plane group. This result is surprising because the plane group represents a polar termination, which is expected to exhibit a high surface energy unless compensated by surface adsorbates, atomic reconstruction, or preferential termination of O or N planes to balance the excess valence. It has been previously observed that MgO and NiO form low-energy metastable structures at polar {111} facets through spontaneous dissociative water adsorption. The reported high visible light water splitting activity of $(GaN)_{1-x}(ZnO)_x$ particles suggests that pathways of this type might be accessible.

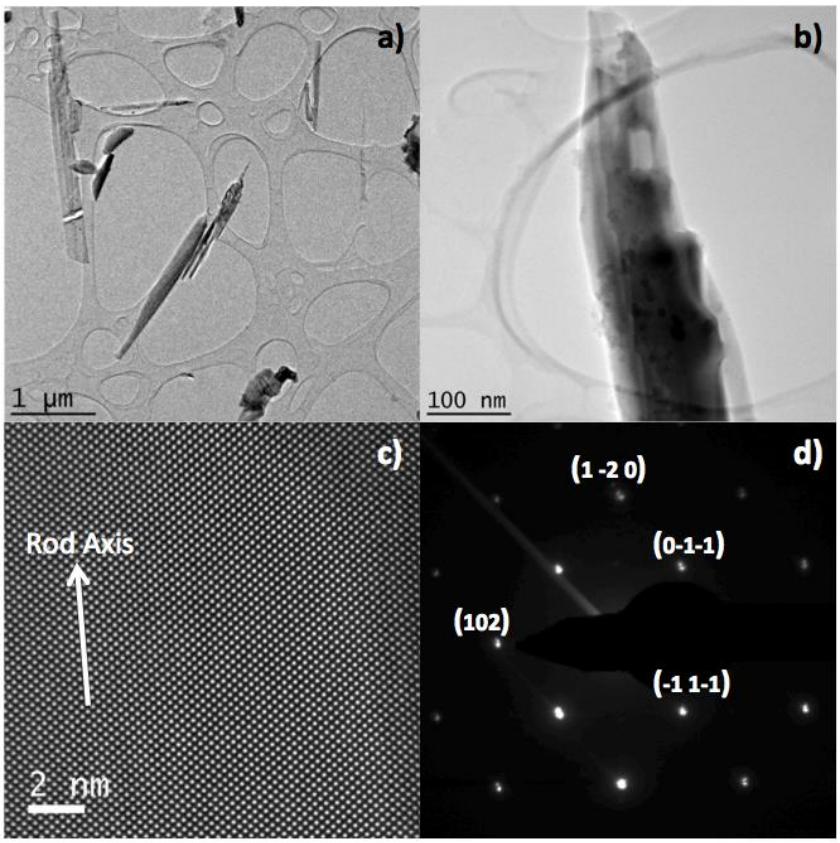

Figure 2.12. TEM images of x_v = 0.21 $(GaN)_{1-x}(ZnO)_x$ from 2:16 precursor (a) low resolution, (b) medium resolution, (c) high resolution, (d) electron diffraction indicating (1$\underline{2}$10) rod growth plane.

The observation of potentially polar facets suggests that the superb photoactivity of $(GaN)_{1-x}(ZnO)_x$ wurtzite for overall water splitting may be enabled by the polar space group (*P6$_3$mc*, #186) of this compound. The possible polarity of the {10$\underline{1}$1} facets can be clearly seen in the alternating layers of cations and anions in the face normal direction (Figure 2.13 d). An internal electrical field will drive photogenerated electrons and holes in opposite directions, resulting in a physical separation of charges that should appreciably reduce the rate of charge recombination processes. Enhanced carrier lifetimes will directly increase the quantum efficiency of the semiconductor-driven photoelectrochemical reactions for water splitting. Charge separation driven by polarity is expected to retain its effectiveness in nanoparticles, unlike the charge separation driven by band-bending, a phenomenon which often requires semiconductor thicknesses on the order of one

micron to fully develop. Internal semiconductor electric fields have been recently utilized to produce junction-free photovoltaics,[71] convincingly demonstrating that internal electric fields can strongly influence charge separation within semiconductors.

Interestingly, many of the best wide band gap semiconductors for driving overall water splitting are titanates, niobates, and tantalates that contain early transition metals whose tendency to displace away from the center of their normal octahedral coordination environment is commonly harnessed in ferroelectric materials such as $BaTiO_3$, indirectly suggesting that polarity may play a large but generally unrecognized role in promoting photoactivity. There have been experiments on $BaTiO_3/TiO_2$ composites which suggest a synergy occurs when the electric field of $BaTiO_3$ interacts with a surface coating of TiO_2.[72] Outside of these transition metals, single crystal photoelectrochemical studies on wurtzite ZnO have found quantum efficiencies for water oxidation/splitting of approximately 65%.[73] While the growth of non-polar GaN films was a critical step in maximizing radiative carrier recombination to promote the efficient emission of blue light in LEDs,[74] the enhancement of polarity in $(GaN)_{1-x}(ZnO)_x$ semiconductors by methods such as producing particles with facets normal to the polar {0001} axis or by minimizing defects or surface reconstructions which suppress the development of an electrical dipole are suggested as promising pathways for inhibiting carrier recombination and substantially improving water splitting quantum yields in this system.

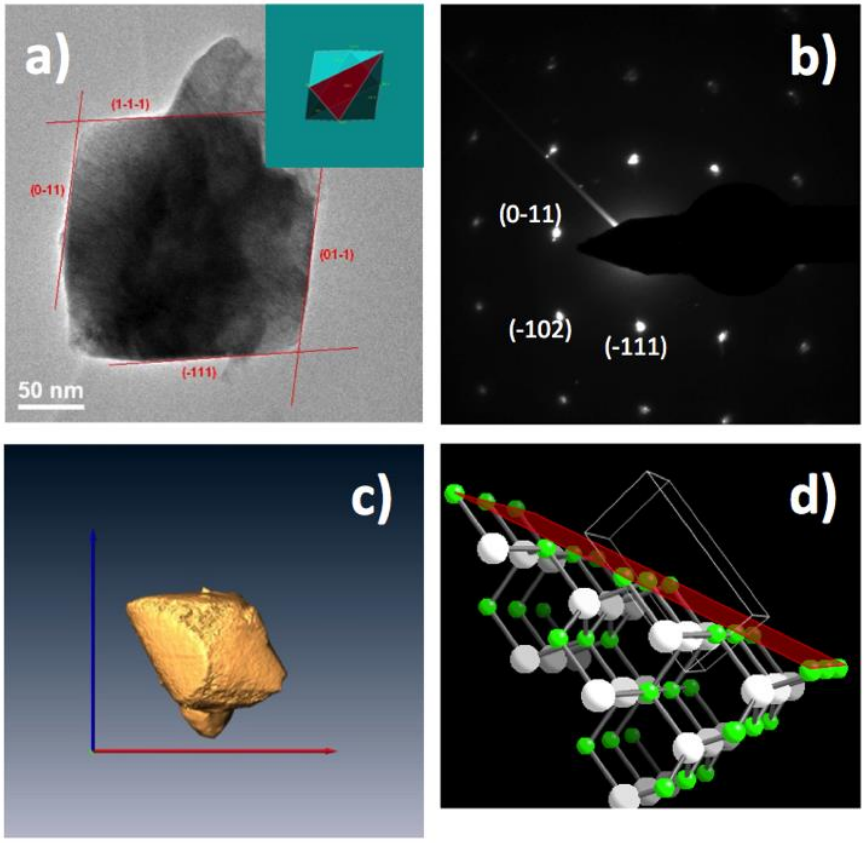

Figure 2.13. $(GaN)_{1-x}(ZnO)_x$ $x_v = 0.21$ from $ZnGa_2O_4$ precursor (a) TEM image (b) electron diffraction pattern collected along [211] direction (c) three dimensional reconstruction of tomographic reconstruction (d) atomic model of polar {10$\underline{1}$1} termination.

2.4 Conclusions

A new synthesis method has been developed for preparing Zn-rich $(GaN)_{1-x}(ZnO)_x$ samples via a Zn-rich $Ga_2O_3(ZnO)_{16}$ compound belonging to the $Ga_2O_3(ZnO)_m$ homologous series. This Zn-rich precursor has a structure with layers that closely resembles the wurtzite structure. Synthesis in this manner has shown to produce $(GaN)_{1-x}(ZnO)_x$ nanorods with band gaps as low as 2.53 eV. Compositional analysis finds Zn contents up to $x \sim 0.55$ with evidence that Ga vacancies may be occurring at the 2-3% level for Ga-rich samples. TEM tomography studies conclusively show that the polar {01$\underline{1}$1} facets are dominant in spinel-derived $(GaN)_{1-x}(ZnO)_x$, making this the active facet on which water splitting occurs, and suggesting that polarity may play an important role in enhancing the charge separation and photoactivity of this phase.

Chapter 3

Cubic intergrowths in wurtzite $(GaN)_{1-x}(ZnO)_x$ semiconductors and methods for their quantification by Rietveld refinement

The $(GaN)_{1-x}(ZnO)_x$ solid solution is an important visible light absorbing semiconductor capable of driving overall water splitting when properly functionalized. While these compounds are well-known to have a wurtzite structure type based on hexagonal close packed (hcp) layers, it is demonstrated through transmission electron microscopy studies that this system can contain abundant cubic close packed (ccp) intergrowths. Furthermore, it is found that these intergrowths exist without giving rise to the Bragg diffraction peaks expected for the zinc blende structure type associated with cubic close packing due to the consistently narrow thickness of these intergrowths. To overcome the absence of characteristic cubic diffraction peaks, a method for quantifying the fraction of the minority ccp intergrowth phase has been developed using the explicit Rietveld refinement of large trial superstructures (up to ~120 layers) that allow different stacking sequences to be tested. Some general geometric rules for constructing viable stacking sequences are presented. It is shown that the explicit superstructure method allows for (1) the fraction and (2) the width of the intergrowths to be separately investigated using powder diffraction data, and that the independent refinement of the crystallographic parameters associated with both the majority hcp and minority ccp phases is possible. Furthermore, it is shown that using an explicit supercell as the majority phase in multiphase refinements (with secondary phases of hcp wurtzite and/or ccp zinc blende) provides the ability to effectively investigate large or small concentrations of the minority phase that would otherwise require prohibitively large supercells to model. For the specific case of $(GaN)_{0.65}(ZnO)_{0.35}$ prepared from a $ZnGa_2O_4$ precursor, it is shown that the average width of the ccp intergrowths is about 4 layers, and that these intergrowths make up about 9% of the sample. The present methods for studying stacking defects should be generally applicable to the study of defects in other important compounds whose structures are built from stacked close-packed

layers, including a variety of technologically important wurtzite and zinc-blende semiconductors as well as the general class of α-$NaFeO_2$-type layered battery materials.

3.1 Introduction to hcp-ccp transition in wurtzite semiconductors

The wurtzite structure is one of the simplest and most common structure types for binary semiconductors, including II-VI, III-V, and I-VII type compounds.[75,76,77] For example, the III-V compound GaN is an extensively studied wide band gap semiconductor whose most common applications are in optoelectronics (especially in LEDs) due to the relatively large band gap of this material (~3.4 eV). The wurtzite structure of GaN is built from two hexagonally close packed (hcp) layers of N anions, with the Ga cations placed in half of the tetrahedral sites in this structure to form GaN_4 tetrahedra (Figure 3.1a). Since the occupied tetrahedral sites all have the same orientation, wurtzite compounds crystallize in a polar space group (*P6$_3$mc*, #186). Although the thermodynamically stable form of GaN is wurtzite, the closely related cubic zinc blende polytype of GaN is only slightly higher in free energy,[76] and can be experimentally observed for samples prepared as epitaxial films under suitable strain conditions,[78,79] or even as single crystals obtained using suitable nucleation and growth conditions.[80,81,82] This same polymorphism behavior is also observed for ZnO.[83,84,85,86] Like the wurtzite structure, the non-polar cubic zinc blend structure of GaN (*F-43m*, #216) also consists entirely of GaN_4 tetrahedral environments with a common orientation (Figure 3.1b), though with a unit cell that spans 3 cubic close packed layers (ABC stacking) rather than the 2 layers of wurtizite (AB stacking). The very close similarity of these two structures is apparent in Figure 3.1, and the analogous geometrical arrangement of the layers in these structures permit a coherent interface to be formed in the $(001)_H$ and $(111)_C$ directions relative to the hexagonal and cubic unit cells, respectively. The present work is concerned with the $(GaN)_{1-x}(ZnO)_x$ solid solution, a semiconductor system which is known to have exceptional properties for overall water splitting driven by visible light due to its medium band gap

(E_g ~ 2.5 – 3.0 eV) [46, 87,35] and whose previously measured diffraction patterns have exclusively been indexed to the wurtzite structure in many prior studies. [88,89,30]

a.

b.

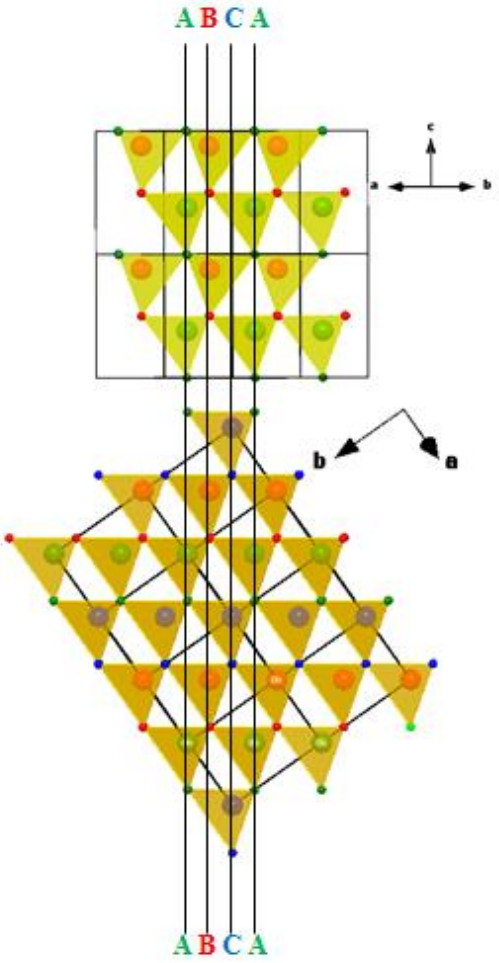

c.

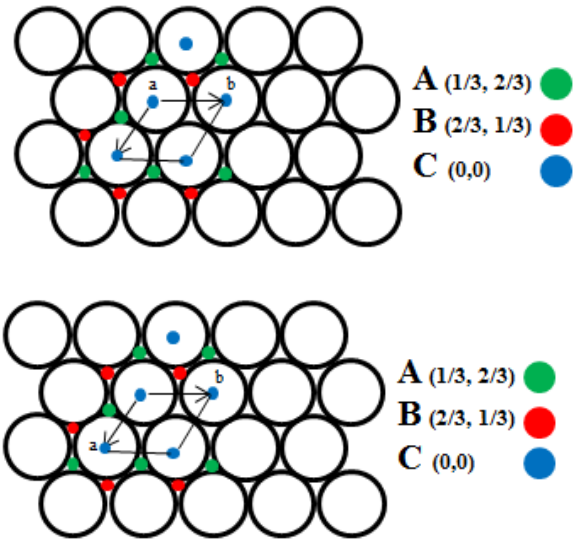

Figure 3.1. Structures of (a) hexagonal wurtzite and (b) cubic zinc blende polymorphs of GaN, both of which are built from close-packed N anion layers. The cubic cell of GaN is shown with the 111_C axis vertical to emphasize the close-packed layers which stack in this direction. Also, (c) an illustration of the relationship of the hexagonal wurtzite unit cell to the three positional choices (A = green; B = red; C = blue) for layers of close-packed spheres.

The relationship of the atom positions in the hexagonal wurtzite GaN structure to the well-known descriptions of close-packed layered structures[87,90] is worth explicitly discussing. A single close-packed anion layer of type **A** is shown in Figure 3.1c, with a green dot at the position of the centers of the atoms, with the standardized wurtzite unit cell superimposed. The anions in this **A** layer have the in-plane fractional coordinates (1/3, 2/3). In a generic close-packed structure, there are two choices for how the next layer in the +z direction can be placed. The red dots indicate the **B** position of (2/3, 1/3), while the blue dots indicate the **C** position of (0, 0). Since the wurtzite structure has an **AB** stacking sequence, no anions will be found in the column of **C** position located at the origin of the marked unit cell. In the standardized wurtzite structure, cations are located only in the tetrahedral voids located directly below the anions, and thus each pair of Ga and N atoms will share the same in-plane fractional coordinates, though by convention a Ga cation is situated in the basal plane with fractional coordinates of (1/3, 2/3, 0) while its paired N anion is at (1/3, 2/3, *z*) with a value of *z* that is near the value of 0.375 expected for ideal tetrahedra. As a result of this convention, each tetrahedron appears to point down (in

the -*c* direction). The second pair of crystallographically equivalent atoms in the hexagonal unit cell have coordinates of (2/3, 1/3, 1/2) and (2/3, 1/3, 1/2 + z) for Ga and N, respectively. It should be noted that all of the atoms positions for the cubic zinc blende polytype of GaN can also be completely specified using a trigonal unit cell with the *a*/*b* dimensions specified in Figure 3.1c , though with a larger c-axis length to accommodate the 3-layer repeat period in this direction. Since a single close-packed layer consisting of 1 N and 1 Ga ion (with the latter residing in a tetrahedral void) is about 2.6 Å in height, the normal hexagonal wurtzite c-axis (**AB** stacking) is about 5.2 Å and the extended c-axis for describing the cubic atom positions (**ABC** stacking) in a trigonal unit cell setting is about 7.8 Å, a length that corresponds to the $(111)_C$ body diagonal of the standard zinc blende cubic cell.

From this analysis, it can be seen that many additional stacking variants can be constructed in which the c-axis length may change, while the *a*- and *b*-axis lengths are preserved. In addition to the hcp (2-layer) and ccp (3-layer) stacking sequences, there are many known mixed closed packed structures in which larger numbers of close-packed layers (4, 6, 8, 9, *etc.*) exist in the fundamental ordered unit cell.[91,92] In addition to these relatively common ordered stacking variants, it is also possible to find close-packed structures in which randomly distributed disordered stacking faults occur. In some cases, these faults occur because the free energy gained from the enhanced entropy outweighs the enthalpic penalty for forming these faults, though it is also possible that the faults represent a kinetically trapped transient state and that these faults will disappear if the system is brought to equilibrium by an appropriate thermal annealing process.

Even when present in small quantities, stacking faults can substantially modify the properties of materials, such as the luminescence response of GaN.[93] This is not surprising since a single stacking fault can reverse the polarity inherent to GaN and other polar wurtzite semiconductors, and thereby impact the recombination of photogenerated electrons and holes. Although there have been some predictions that there are substantial differences in the band gap of wurtzite and zinc blende

polymorphs,[76] comparative experimental measurements have not found significant differences in the band gaps of these two polytypes of GaN and ZnO. It therefore seems likely that mixed closed packed variants of these semiconductors will not have large differences in their band gaps either. Some explicit calculations of the effects of different types of stacking faults in ZnO (Type I, II, III, and extrinsic)[94] on the electronic structure have previously been carried out. It was shown that states at the conduction band minimum are mainly associated with cubic layers, while those at the valence band maximum were mainly associated with hexagonal layers. This was predicted to lead to localization due to the introduction of trap states for minority carriers and diffusion barriers to majority carriers.[95]

Semiconductors in the $(GaN)_{1-x}(ZnO)_x$ system have achieved the highest quantum efficiency (~6%) thus far for a powder suspension driving overall water splitting with visible light irradiation,[35] and have been intensively studied in recent years for this reason. The promise of this system for overall water splitting has inspired many synthetic investigations, though it should be noted that the various powder synthesis methods investigated (using a number of different precursors) have invariably been non-equilibrium techniques due to the strong tendency of Zn to rapidly evaporate under the strongly reducing conditions of these ammonolysis reactions. Because of Zn volatility, initial synthetic work only accessed a portion of the full solid solution ($x \leq 0.42$), though more recent studies have found that essentially the entire solid solution ($0 \leq x \leq 1$) can be accessed using modified synthetic pathways.[30,96] The strong interest in achieving a full solid solution is closely linked to the predictions[26] and observations[97,98,99] that the $(GaN)_{1-x}(ZnO)_x$ band gap strongly varies with composition, since maximizing visible light absorption is important to maximize the overall solar-to-fuel conversion efficiency.

The defect states associated with the $(GaN)_{1-x}(ZnO)_x$ wurtzite solid solution have not previously been investigated in detail, though it is expected that the defects of this system should be closely related to those of the homogenous wurtzite end members ZnO and GaN. It is expected that defects in this

semiconductor system may affect both light absorption (by modifying the band gap) and the rate of carrier recombination (by providing sites for rapid recombination and/or by modifying the internal electric field in these polar semiconductors). Point defects are known for both ZnO and GaN, and indirect circumstantial evidence for similar defects in semiconductors of $(GaN)_{1-x}(ZnO)_x$ has previously been presented.[99] Stacking faults have not previously been identified for the $(GaN)_{1-x}(ZnO)_x$ system. In the present work, it is shown that coherent stacking faults are very abundant in certain preparations of $(GaN)_{1-x}(ZnO)_x$ semiconductors, resulting in ~10% of the phase not adopting the expected wurtzite structure. The observed stacking faults are shown to be best described as cubic intergrowths with a common width, in contrast to the randomly occurring isolated stacking faults (Type I, II, III, etc.) that are most commonly discussed for the wurtzite class of semiconductors. New methodologies for quantifying the average abundance of cubic intergrowths in powder samples through the direct Rietveld refinement of large trial superstructures have been developed, and are shown to be effective even for small concentrations of defects. These general methods for quantifying stacking defects will enable the elucidation of structure-property relationships both in the present system, and in the larger class of industrially important wurtzite semiconductors.

3.2 Experimental

3.2.1 Synthesis of $(GaN)_{1-x}(ZnO)_x$ from $ZnGa_2O_4$

The synthesis of $(GaN)_{1-x}(ZnO)_x$ semiconductors was accomplished using $ZnGa_2O_4$ precursors, which were prepared by reacting stoichiometric amounts of Ga_2O_3 and ZnO (1:1) at 1000 °C in air in a box furnace for a total of 24 h with an intermediate grinding after 12 h to promote reactivity and product homogeneity. Conversion of the $ZnGa_2O_4$ precursor into a wurtzite oxynitride was done at 850 °C under flowing NH_3 (5mL/min) for times of 10-18 h. In order to obtain samples with $x > 0.33$, excess ZnO powder (~2.0g) was placed upstream of the precursor in order to increase Zn vapor pressure above the sample during synthesis. Increasing the vapor pressure allowed for excess Zn to enter the sample

powder and increase the overall zinc content as compared to the $ZnGa_2O_4$ starting material. After heating, the sample was cooled to room temperature under NH_3 flow and the tube was then purged with N_2 gas prior to sample removal. Samples prepared in this method gave powder diffraction patterns whose peaks could be completely indexed using a single wurtzite phase, though the zinc content (and lattice parameters) depended on the details of the synthesis reaction.

3.2.2 Powder X-ray diffraction

X-ray powder diffraction on a Bruker D8 Advance laboratory diffractometer (λ = 1.54059 Å) using 12 mm variable slits and a 192-channel Lynx-Eye linear strip detector was used to identify phases present in all samples and to receive preliminary lattice parameter values. Samples were reacted until the X-ray diffraction patterns showed them to be free of $ZnGa_2O_4$ impurities within the detection limit of the diffractometer, estimated to be less than 1 wt % for this system.

3.2.3 Transmission electron microscopy

Transmission electron microscopy experiments were performed in an FEI Titan 80-300 microscope equipped with a CEOS third order image aberration corrector and dedicated environmental gas cell. All high-resolution images were collected with a residual spherical aberration value of -2 microns, and recorded on a Gatan Ultrascan 1000 CCD detector. All data acquisition and analyses were completed by Dr. James Ciston at the CFN, Brookhaven National Laboratory.

3.2.4 Powder neutron diffraction

Time-of-flight powder neutron diffraction measurements were performed on POWGEN at the Spallation Neutron Source, Oak Ridge National Laboratory during run cycle 2010-B. Data were collected at a 300 K with a pulse rate of 30Hz and a data collection time of about 8 hours (total proton charge of 1.5×10^{14}). Data were collected in a frame with a center wavelength of λ = 1.066 Å, and

covered a *d*-spacing range of $d = 0.28 - 3.1$ Å (merged into a single data set) with a typical $\Delta d/d$ of 2×10^{-3}.

3.2.5 Rietveld refinement

Rietveld refinement of diffraction data was done using the TOPAS software package (version 4.2, Bruker AXS). Samples collected on POWGEN were ground and packed with 1/3 weight % Si standard for peak intensity scaling purposes. This also allows for instrumental versus sample effects on the diffraction pattern due to the intense and sharp peaks exhibited by cubic silicon. Atom occupanices were fixed to describe shared sites dependent on zinc composition, or *x*. Supercell modeling of atom positions was created by expanding a normal wurtzite unit cell in the c direction and calculating z positions accordingly. Careful limitations were put on thermal parameters, interatomic distances, and cation z positions in order to represent a realistic model without overlapping atoms. Automation of printing out atomic positions and implementing the values into a proper INP file for its use in the TOPAS software was implemented using a python script.

3.3 Results

A modified synthesis procedure involving the use of upstream ZnO to generate a near-constant vapor pressure of gaseous Zn was used to prepare samples of the visible light absorbing semiconductors in the $(GaN)_{1-x}(ZnO)_x$ solid solution under near-equilibrium synthesis conditions (reaction times of 10 – 18 h). The powder X-ray diffraction peaks of $(GaN)_{1-x}(ZnO)_x$ samples prepared in this manner could be fully indexed using a hexagonal wurtzite structural model, in accord with all prior studies of this phase. While a variety of phases were prepared and examined, the present report will focus on the detailed analysis of a representative sample of $(GaN)_{0.65}(ZnO)_{0.35}$ sample, whose indexed diffraction pattern is shown in Figure 3.2.

3.3.1 Modeling with average wurtzite structure

All diffraction peaks observed for the $(GaN)_{0.65}(ZnO)_{0.35}$ sample can be fully indexed using a wurtzite structural model, with refined lattice parameters of a = 3.208 Å and c = 5.198 Å in space group $P6_3mc$. While the positions of the peaks are in good agreement with the expected wurtzite structural model, other aspects of the pattern suggest more complex behavior for this sample. The peak breadths are highly angle-dependent, consistent with the presence of size and/or strain broadening. However, the peak shapes cannot be effectively modeled even when both size and strain broadening are included in Le Bail fits of the diffraction data. This is a consequence of the presence of anisotropic peak broadening, whose influence is required to explain the substantially narrower width of the 002 diffraction peak at 33° 2θ relative to nearby peaks at both lower (100 peak at 32°) and higher diffraction (110 peak at 36°) angles. Anisotropic peak broadening often occurs as a result of stacking faults, though other origins for this effect are also possible.[100,101,102]

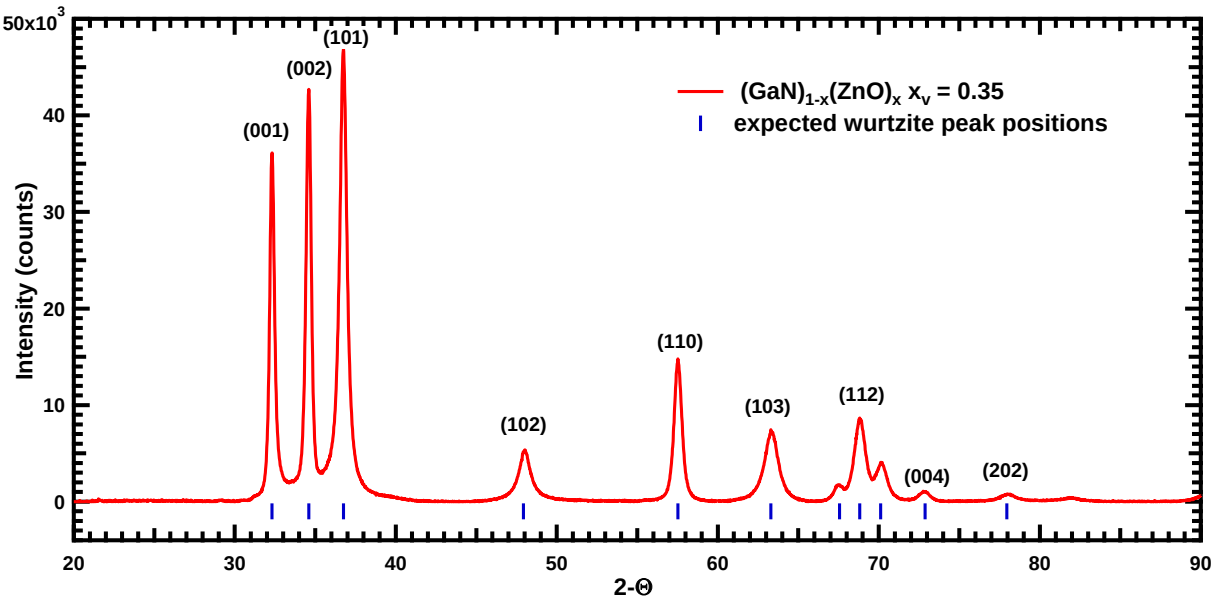

Figure 3.2. Powder X-ray diffraction pattern of $(GaN)_{1-x}(ZnO)_x$. Expected wurtzite peak positions are marked below the diffraction pattern.

In order to obtain the highest quality structural information from this powder $(GaN)_{0.65}(ZnO)_{0.35}$ sample, time-of-flight powder neutron diffraction data were collected (Figure 3.3). This neutron

diffraction data has the advantage of having good sensitivity to all atoms in the structure (coherent neutron scattering lengths in fm of b = 7.288 for Ga, 5.680 for Zn, 9.36 for N, and 5.803 for O). Furthermore, the use of the white neutron beam of the POWGEN beamline enables data with reasonable counting statistics to be collected out to d_{min} ~ 0.19 Å, allowing the intensity of many more peaks to be included in Rietveld refinements than in typical analogous laboratory or synchrotron X-ray powder diffraction studies. Finally, the neutron linear absorption coefficient of the present sample is negligible (μ_L ~ 0.034 cm^{-1} at λ = 1 Å), which facilitates the determination of meaningful displacement parameters for the two different atomic sites in the wurtzite structure. It should be noted that the absorption of the vanadium can used to hold the powder sample during diffraction experiments is non-negligible. An internal Si standard (peaks marked with asterisks) was therefore used in diffraction experiments both as a reference for absorption correction (the displacement parameter of Si is well known, and will be reproduced in Rietveld refinements if absorption corrections are properly implemented) and as a mass reference to permit the direct refinement of the GaN:ZnO ratio in the sample.

Despite the extreme simplicity of the wurtzite structure, it was impossible to effectively model the observed neutron diffraction peak intensities even when all appropriate crystallographic parameters were freely refined (two independent lattice parameters, one positional parameter total for the two crystallographic sites, two independent displacement parameters which could be refined either isotropically or anisotropically). These problems persisted even after the anisotropic peak broadening was treated using the phenomological model of Stephens.[101] Structural refinements carried out in this manner resulted in the modeled peak intensities having errors of 10-20% in many cases, as can be seen in the difference pattern of Figure 3.3.[103] This suggests that the wurtzite structural model is not wholly appropriate for the present sample of $(GaN)_{0.65}(ZnO)_{0.35}$.

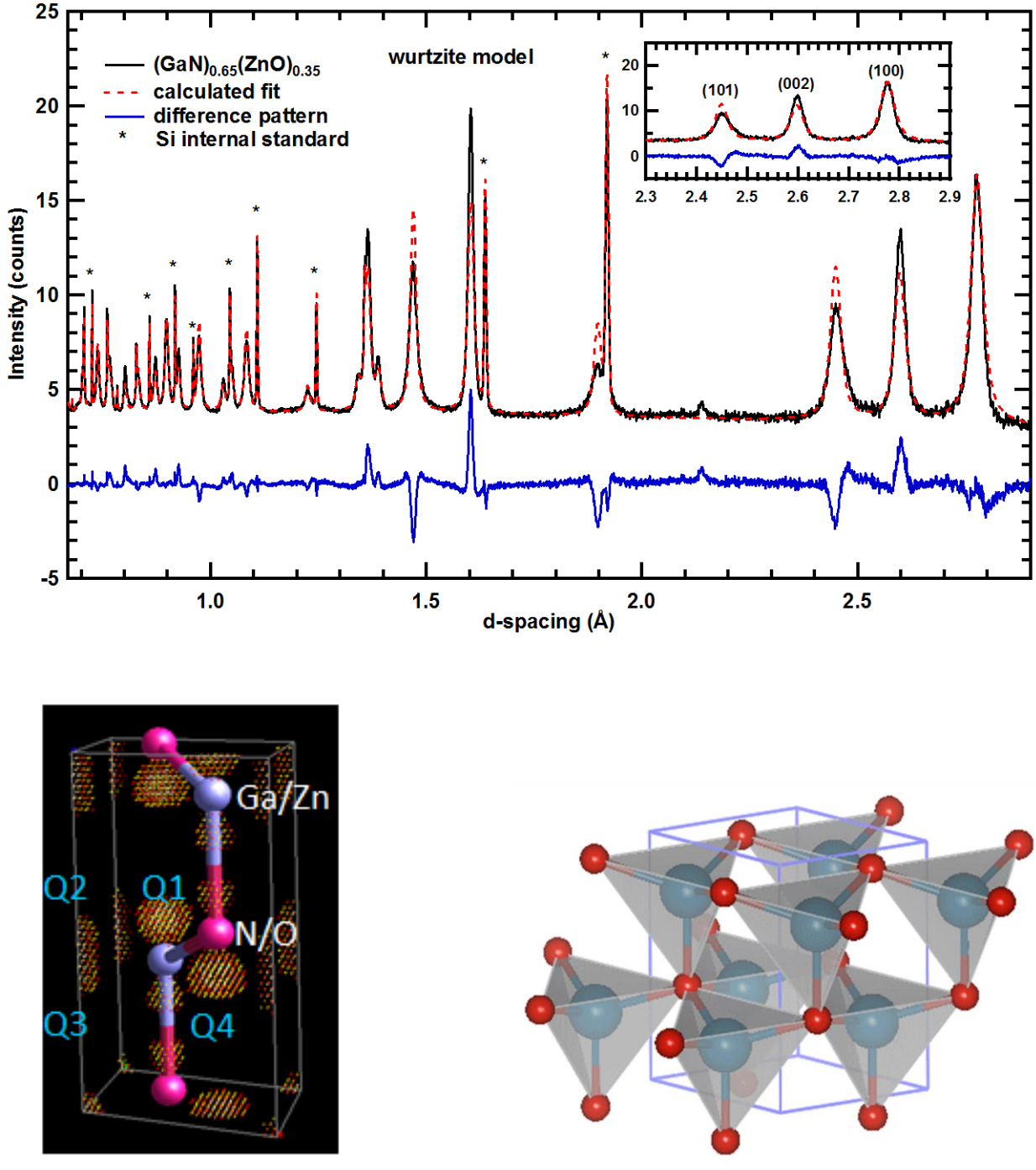

Figure 3.3. Top: Neutron diffraction pattern of $(GaN)_{1-x}(ZnO)_x$ x_v = 0.35 with calculated fit using normal 4 atom wurtzite unit cell model with cations (Ga/Zn) and anions (N/O) having shared sites, R_{wp}

= 4.214. Inset depicts poor fitting of the prominent three wurtzite peaks. (Data collected at ORNL, SNS, POWGEN beamline and analyzed using TOPAS software suite). Bottom: Fourier difference map of $(GaN)_{1-x}(ZnO)_x$ $x_v = 0.35$ from powder neutron Rietveld refinement where positions are labeled as Ga/Zn: (1/3, 2/3, x); N/O: (1/3, 2/3, 0); Q1(N/O): (0, 0, 0); Q2(N/O): (2/3, 1/3, 0); Q3(Ga/Zn): (0, 0, x); Q4(Ga/Zn): (2/3, 1/3, x).

The positions within the wurtzite unit cell most directly responsible for the large differences between the observed and measured intensities were identified using Fourier difference maps calculated from Rietveld refinements, and are shown in Figure 3.3. Four independent crystallographic sites gave rise to positive peaks in the difference map (Table 3.1). Each of these four positions has the spherical shape expected for scattering associated with well-defined atomic sites, suggesting that these positions are associated with minority atomic sites rather than with artifacts of the Fourier transform. Two sites occur at the same *z*-height as N ($z = 0$) but are displaced by vectors of (1/3, 2/3, 0) and (2/3, 1/3, 0). The other two minority sites occur at the same z-height as Ga ($z = 0.383$), and are related to this site by the same displacement vectors. If the original Ga and N majority site positions are taken to be those of an **A** close-packed layer, the positions of the minority sites are exactly those expected for close-packed layers with **B** and **C** positions, and suggest that stacking faults are the physical origin of the scattering intensity at these four minority sites.

It should be noted that minority sites were previously proposed for $(GaN)_{1-x}(ZnO)_x$ based on the maximum entropy method (MEM) analysis of synchrotron X-ray diffraction data for a sample described as $(GaN)_{0.885}(ZnO)_{0.115}$.[88] However, the proposed model of a 50/50 split nitrogen site was not chemically sensible (did not permit a low-energy coherent interface to be formed; two domains were symmetrically equivalent and indistinguishable if present as large domains). In light of the present results, it appears that the two minority sites associated with Ga were incorrectly attributed to scattering from N, and the two minority sites from N were not resolved due to the weak scattering power of N relative to Ga. The good sensitivity of neutrons to all atoms in the $(GaN)_{1-x}(ZnO)_x$ solid solution is in this case critical for

properly identifying the chemical and structural origin of the differences in diffraction peak intensities relative to the simple wurtzite structure.

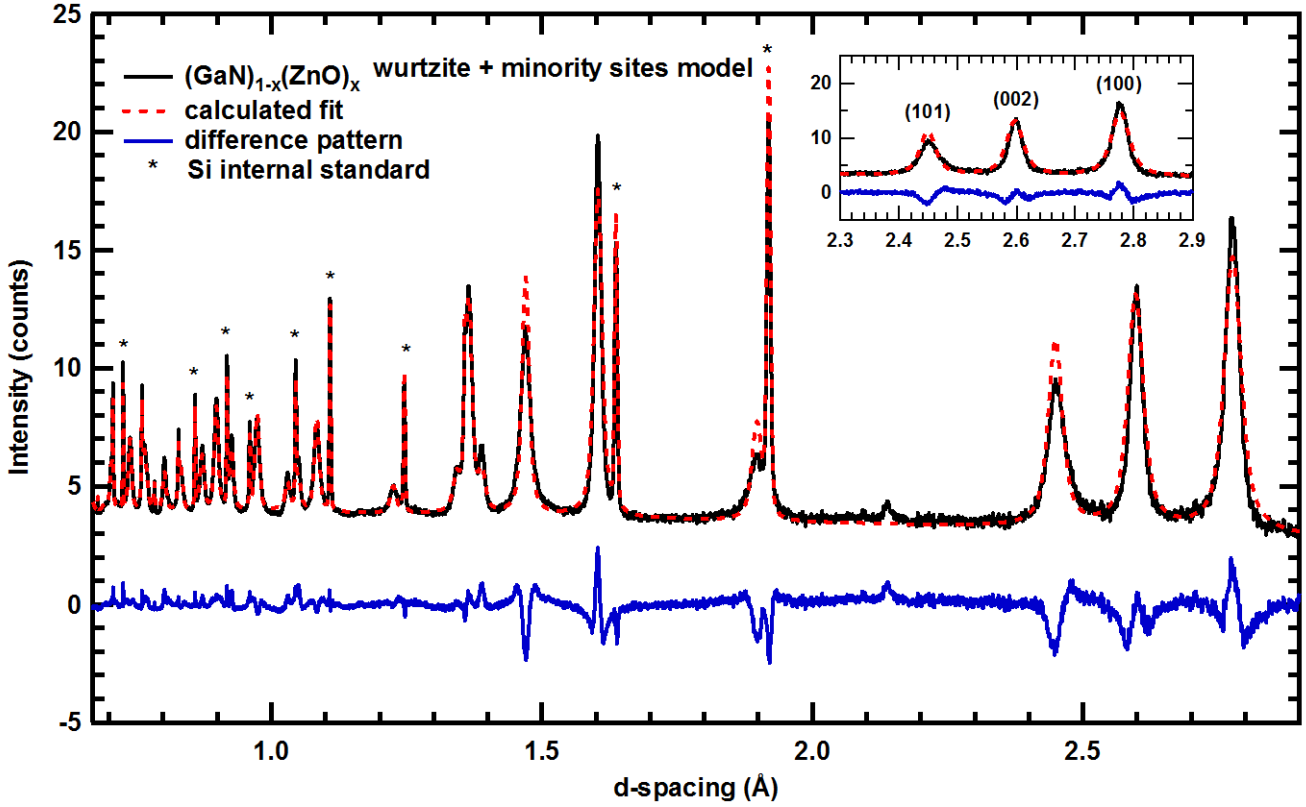

Figure 3.4. Rietveld refinements using the basic wurtzite structure with the addition of four minority sites at positions expected for stacking faults (R_{wp} = 3.779).

These minority sites can be explicitly added to the structural model for Rietveld refinement, and substantially improve the quality of the overall fit (Figure 3.4), with the R_{wp} of the refinement being reduced from 4.21% to 3.78%. The crystallographic parameters obtained from the refinement done in this manner are provided in Table 3.1. The refined occupancy of the minority site corresponding to an A → B stacking defect is 2.7%, while that of the site corresponding to an **A** → **C** stacking defect is 4.2 %. Furthermore, the displacement parameters associated with the Ga site (B_{eq} = 0.10) and N site (B_{eq} = 0.10) are stable in refinements and converge to values which are very consistent with expectations based on prior single crystal diffraction data for chemically related compounds. The well-resolved spherical

peaks in the Fourier difference map at low defect concentrations attest to the superb quality of the present time-of-flight neutron diffraction data, and suggest that isolated anion defects sites with occupancies of only ~1% may be directly resolvable using time-of-flight neutron powder diffraction data. While there are many existing indirect methods for identifying the presence of such defects, there are clear advantages to being able to directly resolve both the nature and abundance of defects in materials of technological importance, especially since powder diffraction techniques can be utilized for both *in situ* and *in operando* experiments.

Table 3.1. Crystallographic parameters obtained from the refinement of $(GaN)_{0.65}(ZnO)_{0.35}$ using a wurtzite model with added minority sites.

		crystal system		Hexagonal		
		space group		$P6_3mc$ (#186)		
		lattice parameters (Å)		*a* 3.2082(1)		
				c 5.1974(3)		
Atom	Wyck	*x*	*y*	*z*	B_{eq}	occ
Ga0	2	1/3	2/3	0.3785(3)	0.10(5)	0.605(1)
N0	2	1/3	2/3	0	0.10(4)	0.605(1)
Zn0	2	1/3	2/3	0.3785(3)	0.10(5)	0.3258(6)
O0	2	1/3	2/3	0	0.10(4)	0.3258(6)
Ga1	2	2/3	1 1/3	0.3785(3)	0.10(5)	0.027(1)
N1	2	2/3	1 1/3	0	0.10(4)	0.027(1)
Zn1	2	2/3	1 1/3	0.3785(3)	0.10(5)	0.0095(4)
O1	2	2/3	1 1/3	0	0.10(4)	0.0095(4)
Ga2	2	1	1	0.3785(3)	0.10(5)	0.042(1)
N2	2	1	1	0	0.10(4)	0.042(1)
Zn2	2	1	1	0.3785(3)	0.10(5)	0.0147(5)
O2	2	1	1	0	0.10(4)	0.0147(5)

A first estimate of the prevalence of stacking faults can be obtained by comparing the ratio of the occupancy of the majority sites with the total occupancy of the two minority sites, and in this manner it

is calculated that 7.4% of the atoms in this sample do not reside in the normal position expected for the wurtzite structure. This is a very high concentration of defects, and suggests that the influence of stacking defects on the physical properties of this system cannot be neglected in experimental and theoretical studies of this system. However, the defect concentration obtained in this manner cannot be considered definitive as there are still substantial deviations between the observed and predicted neutron diffraction peak intensities using this average structural model. This suggests that the stacking faults cannot be considered to be isolated defects, and that the present structural model is incomplete due to either a loss of coherence in the wurtzite structure or that there is coherence in the defect layers.

Additional insights into the stacking faults in this system were obtained from STEM studies in an aberration-corrected transmission electron microscope with atomic resolution (Figure 3.5) which provides the opportunity to directly image the atom positions within $(GaN)_{1-x}(ZnO)_x$ samples. The abundance of stacking faults is clearly confirmed in these direct imaging studies. Furthermore, it can be seen that the stacking defects are better described as coherent intergrowths rather than as random stacking faults. These intergrowths commonly have a consistent width of approximately 6 layers (or equivalently, about 2 nm), as seen for the regions marked by yellow arrows. However, a close inspection shows that the width of these planar intergrowths can vary by about 1 layer across their span, and that other types of defects also exist in $(GaN)_{1-x}(ZnO)_x$ samples.

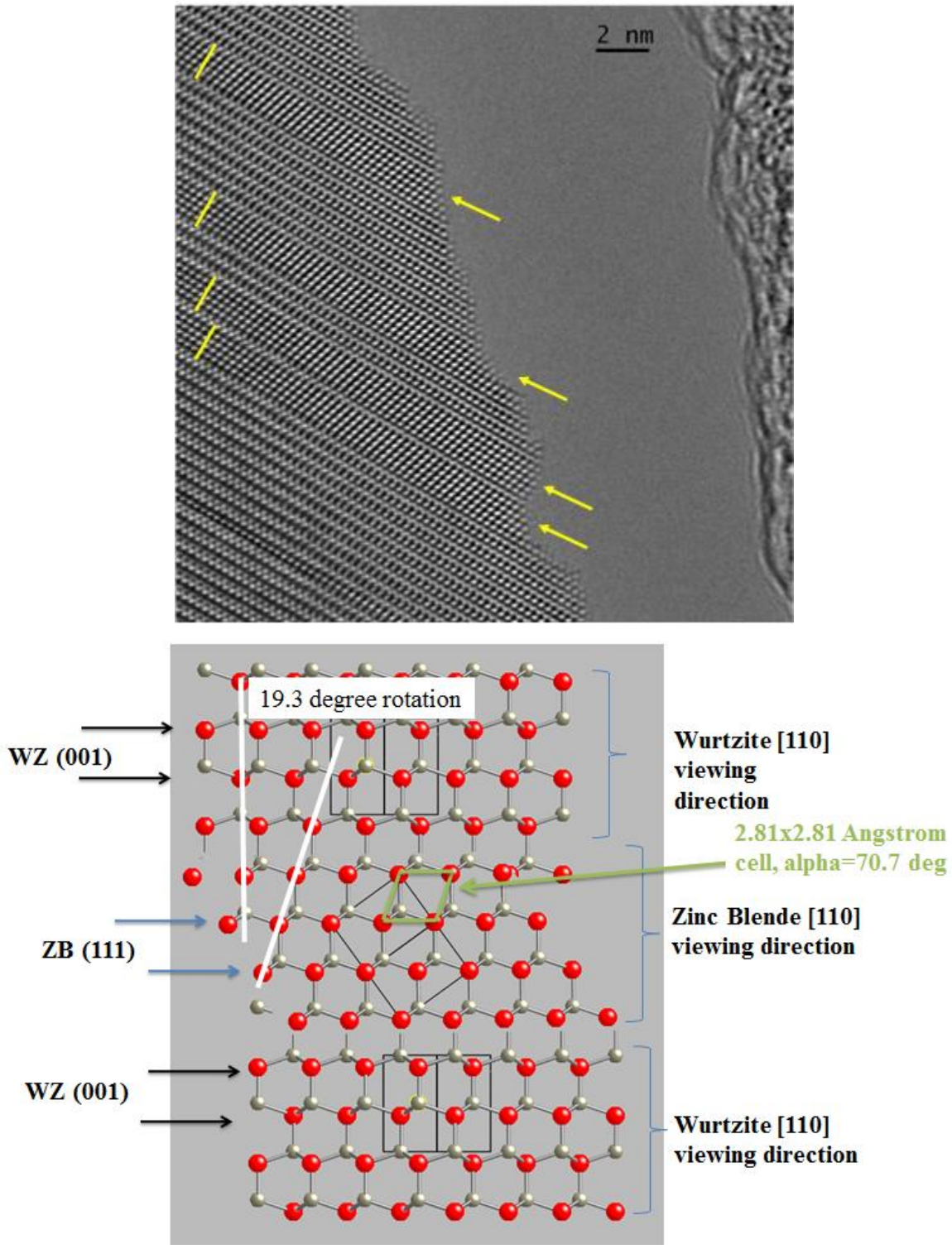

Figure 3.5. Top: STEM image illustrating stacking faults in a $x = 0.20$ sample of $(GaN)_{1-x}(ZnO)_x$. Most faults consist of cubic intergrowths about 6 layers wide (yellow arrows). These intergrowths can be attributed to zinc blende intergrowths based on the comparison of experimental data to expectations from this structural model (bottom).

When a careful analysis of the lattice metrics of the intergrowth regions is carried out, these stacking defects can be confidently assigned as ccp zinc blende intergrowths that form a coherent interface with the majority hcp wurtzite phase. The zinc blende $(111)_C$ direction is found to be parallel to the wurtzite $(001)_H$ direction, as is generally expected for mixed-closed packed structures. As such, an intergrowth width of 6 layers might be expected to be particularly favorable as it is compatible with both the native stacking period of both ccp (3-layer) and hcp (2-layer) layers. The next most common intergrowth width might be expected to be 3 layers. Based on the observed STEM images, the classical formation mechanism for isolated stacking faults seems to be strongly disfavored in the present systems for reasons that will be discussed later. While the STEM imaging studies are very effective for identifying the type of defects that may be present, these electron microscopy studies are not well suited to accurately quantifying the abundance of defects for a series of powder samples.

3.3.2 Stacking rules for generating trial superstructures

These preliminary Rietveld refinements demonstrate that it is impossible to effectively model the structure of $(GaN)_{1-x}(ZnO)_x$ in a simple wurtzite unit cell (a ~ 3.2 A; c ~ 5.2 A). This is consistent with STEM observations, which show that the stacking defects are both abundant and coherent (mainly present as cubic intergrowths). Larger unit cells must therefore be explored in order to accurately model the observed diffraction patterns. While software methods for probing random stacking faults have been explored before, the present work aims to explicitly construct and test very large supercells in which different models for stacking faults can be evaluated, an approach for which literature precedent could not be found. This work takes advantage of recent developments in software for Rietveld refinement, which in our trials proved capable of dealing with superstructures of up to about 120 close packed layers (a ~ 3.2 A; c ~ 300 Å), and was motivated by other recent diffraction studies using superstructures to study materials with imperfectly developed translational symmetry.[104,105,106,107,108,109,96] Since it is critically important to have a complete understanding of the requirements for generating periodic unit

cells when generating large trial superstructures, we revisit the stacking rules for close packed structures with an emphasis on this specific consideration.

Table 3.2. Stacking sequences resulting from the insertion of 0 to 6 ccp layers into a hcp matrix.

W	h/c	A/B/C	Shift	
0	hhhhhhhhhh	ABABABABAB	AB→AB	0+
1	hchhhhhhhh	ABCBCBCBCB	AB→CB	2-
2	hcchhhhhhh	ABCACACACA	AB→CA	2+
3	hccchhhhhh	ABCABABABA	AB→BA	1-
4	hccchhhhhh	ABCABCBCBC	AB→BC	1+
5	hcccchhhhh	ABCABCACAC	AB→AC	0-
6	hccccchhhh	ABCABCABAB	AB→AB	0+

The simple conceptual approach this problem is to build up a superstructure in which a cubic slab (1 to 10 ccp layers in width) is inserted into a base wurtzite structure (consisting of 10 – 100 hcp layers) to form a periodic block containing a large number of total layers, with some details of the method provided in Tables 3.2 and 3.3. This was generally accomplished by working in a lattice with simple trigonal (*P3*) symmetry that reflects the 3-fold rotational symmetry of each close-packed layer, and in which the atom positions of any type of close-packed layer (**A**, **B**, or **C**) can be simply specified. The fractional coordinates associated with each of these three possible types of layers in the present study are specified in Table 3.3 with reference to the N^{th} layer (out of a total of L layers) in the periodic unit cell. It is thus possible to specify any mixed-closed pattern involving mixtures of hcp and ccp layers within this unit cell, and a simple program was written to automatically specify the atomic site positions in each layer when given as input an arbitrary stacking sequence, such as "**ABCABCABAB**".

Table 3.3. Atom Positions of wurtzite and zinc-blende A,B, and C type layers.

Layer	Atom	*x*	*y*	*z*
A	Ga/Zn	1/3	2/3	N/L + 0.383/L
	N/O	1/3	2/3	N/L
B	Ga/Zn	2/3	1/3	N/L + 0.383/L
	N/O	2/3	1/3	N/L
C	Ga/Zn	0	0	N/L + 0.383/L
	N/O	½	½	N/L

Every mixed closed packed sequence of layers must avoid the duplication of site choices in successive layers (**AA**, **BB**, or **CC**) in order to avoid prismatic environments, which will not be considered in the present work. Any individual layer **X** will be a hexagonal (*h*) layer if the nearest neighbor layers above and below are of the same type (**AXA**, **BXB**, or **CXC**), and the layer **X** will be a cubic (*c*) layer if the nearest neighbor layers are different from each other (**AXB**, **AXC**, **BXC**, **BXA**, **CXA**, or **CXB**), following the classic nomenclature.[87] When periodic boundary conditions are considered, the sequence "**ABCABCABAB**" can be rephrased as "*hccccchhh*", and can be seen to consist of a cubic intergrowth that is six layers wide.

When calculating atomic coordinates, it is also useful to also work with in the notation of Hägg, in which a "+" is used to denote a shift between consecutive layers of **A→B**, **B→C**, or **C→A**, and a "-" shift denontes the transitions **A→C**, **B→A**, and **C→B**). The "+" shift corresponds to an in-plane translation of atoms by (1/3, 2/3), while the "-" shift corresponds to translation by the inverse of this vector, which can be written as either as (-1/3, -2/3), or as (2/3, 1/3) due to the periodic boundary conditions of the unit cell. It is also possible to define a "0" shift of (0,0). It should be noted that the application of three consecutive "+" or three consecutive "–" translations leads to a net "0" shift, as does the application of a paired "+" and a "–" shift. In the purely hcp block such as "**ABABAB**", the Hägg pattern is "+-+-+-". The only other possible Hägg pattern for a hcp block of this size is the opposite "-+-+-+" pattern generated by a layer sequence of "**BABABA**".

Unfortunately, when inserting a single cubic slab into a hcp host most combinations of cubic slab width (W) and the total number (B) of close-packed layers in a block are incompatible with periodic boundary conditions. Specific care needs to be taken to avoid these limitations when constructing trial cells. As illustrated in Table 3.4, the introduction of a ccp slab into a hcp host lattice with $B = 10$ results in six possible amounts of shifts between the hcp slab that precedes the cubic layer (set to be **AB** in all cases) and the hcp slab that follows the cubic layer. Five of these six shifts (for $W \neq 6n$) prohibit translational symmetry in the c-axis direction, and four of these five (for $W \neq 3n$) additionally result in the latter hcp block encompassing **C** positions not used in the initial **AB** block. On continuing to add to the width of the cubic blocks, it can be seen that the shift patterns for widths of W and ($W + 6n$) are necessarily identical.

There are two criteria which must be followed for maintaining periodic boundary conditions in a mixed-closed packed system with L layers. The first is that the L total vectors associated with the "+" and "–" shifts must sum to a value equivalent to zero shift (periodic boundary conditions must apply, so it is required that 0^{th} and N^{th} layers have the same position). This first condition is the reason why a pure ccp lattice has minimum period of three layers and not just one layer (Table 3.4). Secondly, the direction of the shifts must not be inverted when translating from one unit cell with L total layers to the next, as would happen for any cell consisting of an odd number of hcp layers. This second condition prevents a pure hcp lattice from have period of less than two layers (Table 3.4). The combined effect of these two conditions is the reason why five-sixths of the arrangements of a single cubic block and a single hexagonal block lack translational symmetry.

Table 3.4. Unique stacking sequences possible for close-packed repeat blocks of 1 - 5 layers*.

h/c	B	L	R	A/B/C	+ / –	1st block shift	Modified Zhadanov	Lattice
$(h)_2$	1	2	2	(AB)	+/-	1-	$[1]_2$	hex/trig
$(c)_3$	1	3	3	(ABC)	+/+/+	1+	∞	cub/trig
$(hc)_2$	2	4	2	(A**B**C**B**)	++/--	2-	$[2]_2$	hex/trig
$(hhc)_3$	3	9	3	(ABA**C**ACB**C**B**B**)	+--/+--/+--	2+	$[12]_3$	rhomb
$(hcc)_2$	3	6	2	(A**BC**A**CB**)	+++/---	0-	$[3]_2$	hex/trig
$(hhhc)_2$	4	8	2	(ABA**B**CBC**B**)	+-++/-+--	2-	$[112]_2$	hex/trig
$(hhcc)_3$	4	12	3	(ABA**C**BC**BA**CA**CB**)	+---/+---/+---	1+	$[13]_3$	hex/trig
$(hccc)_2$	4	8	2	(ABCABACB)	++++/----	1-	$[4]_2$	hex/trig
$(hhhhc)_3$	5	15	3	(ABAB**A**CACA**C**BCBC**B**)	+-+--/+-+--/+-+--	2+	$[1112]_3$	rhomb
$(hhhcc)_2$	5	10	2	(ABA**BC**ACA**CB**)	+-+++/-+---	0-	$[113]_2$	hex/trig
$(hhchc)_2$	5	10	2	(ABA**C**ABA**B**C**B**)	+--++/-++--	1-	$[122]_2$	hex/trig
$(hhccc)_2$	5	5	1	(ABA**CB**)	+----	0+	14	hex/trig
$(hchcc)_2$	5	15	3	(ABCBACABACBCACB)	++---/++---/++---	2+	$[23]_3$	rhomb
$(hcccc)_2$	5	10	2	(ABCABCBACB)	+++++/-----	2-	$[5]_2$	hex/trig
(hhhchc)	6	6	1	(ABA**BC**B**B**)	+-++--	0+	1122	hex/trig

*The block width (B), layer width (L), and # of blocks required to form a periodic cell ($R = L/B$) are specified. Cubic layers are indicated in bold in the A/B/C sequence. Block shift is defined in text, was calculated for the first block only. Slightly non-standard Zhadanov notation is used, always describing the full unit cell contents and demarcating the contents of the repeated building blocks in brackets. Lattice refers to the crystal systems compatible with these stacking patterns.[92]

In order to generally understand how a block of L layers is affected by these two requirements for translational symmetry, we assign a 2-character symbol in which the first character represents the net shift introduced by the block as an integer of 0 (**A→A**), 1 (**A→B**), or 2 (**A→C**), and the second character indicates whether or not the layers in the second repeat of the block will have the same (+) or inverted (-) shifts as corresponding layers in the original block. The labels associated with all unique block widths of $B = 1 – 5$ are presented in Table 3.4, together with the minimum number of layers (L) to have a periodic unit cell with translational symmetry. The net shift (s) can be obtained by taking $s = p –$

n modulo 3, which is the difference between the number of positive (*p*) and negative (*n*) shifts. The sign associated with the shift is + if there are an even number of hexagonal layers, and – otherwise, since only hexagonal layers invert shift vectors. It can be seen that the number of repeats of a block (specified as *h*/*c* or +/- shifts) needed to achieve periodic symmetry in all cases is $R = 1$, 2, or 3.

The conditions giving rise to different values of R are also apparent in this analysis. For all blocks with an inverted (-) shift, $R = 2$. For characters of 1- and 2- (e.g. *hc*), the shift generated by the first instance will be exactly reversed in the second instance of the block due to this inversion, and the two blocks therefore perfectly compensate to give a zero net shift. For a character of 0- (e.g. *hhhcc*), a repeat period of two is still needed despite the lack of a shift in position between the start of the first and second blocks since the direction of the shifts is inverted. In contrast, a character of 0+ (e.g. *hhccc*) will not have this inversion between successive blocks, and thisrepresents the only case for which $R = 1$. The other non-inverted cases of 1+ and 2+ (e.g. *hhhcc*) both result in $R = 3$ since the triple application of these shift vectors is required to return to the original lattice position.

While it is impossible in many cases to construct a single periodic supercell block with one cubic slab with C ccp layers and one hexagonal slab with H hcp layers, it is always possible to construct a periodic cell when the block contents are doubled so that there are two cubic slabs with a total of $2C$ layers and two hexagonal slabs a total of $2H$ layers. The two cubic slabs are taken to have identical widths of C, while the two hexagonal slabs are chosen to have equal (H) or nearly equal width ($H \pm 1$). Since there will be an even number of hexagonal layers in this construction, the net shift due to the hcp layers must be zero since the shift direction is always reversed between successive hcp layers. If the hexagonal slabs each contain an odd number of layers, the shifts of the cubic slabs will be inverted and thus must sum to a zero shift. If this condition does not naturally occur, it can always be obtained by increasing the width of one hexagonal slab (+1 layer) while reducing the width of the other slab (-1 layer), a change that should negligibly impact the resulting diffraction pattern when the width of the

hexagonal layers is large. This construction is designed to ensure that the two halves of the doubled cell have shift characters that cancel (0-/0-, 1-/2-, or 2-/1-), leading to a net 0+ shift for the full doubled unit cell in a manner that is entirely analogous to the behavior observed for the simpler blocks in Table 6 with $R = 2$ unit cells resulting from their "-" shift character (0-, 1-, 2-).

3.3.3 Modeling with explicit superstructures

The goal of the present analysis of $(GaN)_{1-x}(ZnO)_x$ is to use powder diffraction data to obtain insights into the three parameters of (P1) the abundance of the cubic fraction, (P2) the widths of the cubic intergrowths, which are also termed cubic slabs in the notation of the previous section, and (P3) the width of the hexagonal slabs separating the cubic slabs. These three parameters represent only two independent variables since they are related by the relationship: P1 = P2 / (P2 + P3). The present investigation focused on the values of P1 and P2, since P3 was not expected to provide valuable chemical insights into the chemical driving forces for randomly distributed dilute cubic intergrowths in $(GaN)_{1-x}(ZnO)_x$. The validity of different structural models in which these two parameters are varied can be tested in each case by examining the agreement between the calculated and observed diffraction patterns. However, it should be noted that changing the structure to vary one parameter invariably affects other parameter, so there are no simple independent tests for the values of P1 and P2.

A single sample whose composition was assessed to be $(GaN)_{0.65}(ZnO)_{0.35}$ was used to investigate the viability of modeling cubic intergrowths in wurtzite $(GaN)_{1-x}(ZnO)_x$ sample using explicit superstructures, and to develop methodologies for extracting the parameters of interest. A preliminary assessment of the abundance of cubic layers in $(GaN)_{0.65}(ZnO)_{0.35}$ was obtained by using trial structures whose total height was constrained to be about 100 layers, distributed between one cubic and one hexagonal slab (Figure 3.6). For superstructures with an even number of total layers ($L = 100$), it was only possible to vary the cubic intergrowth width in steps of six with $C = 6n$ (solid symbols) for the reasons discussed in the previous section. Additional points for $C = 6n + 3$ (open symbols) were

generated using a unit cell of odd width (L = 101), and resulted in refinement R_{wp} values that were general consistent with the L = 100 results. Fits to these results suggested the abundance of the cubic phase was about 10 %. However, it should be noted that the width of the cubic slab could not be preserved in these trials (strongly varied from C = 3 to 27), and the minimum R_{wp} obtained in this method is expected to only approximately estimate the true fraction of ccp layers in the $(GaN)_{0.65}(ZnO)_{0.35}$ sample for this reason. Furthermore, this method is very limited in both the minimum cubic fraction that can be probed (~3%) and the increment in this quantity between trials (~3%) as a result of the present computational limits on the size of the supercell width (~120 layers).

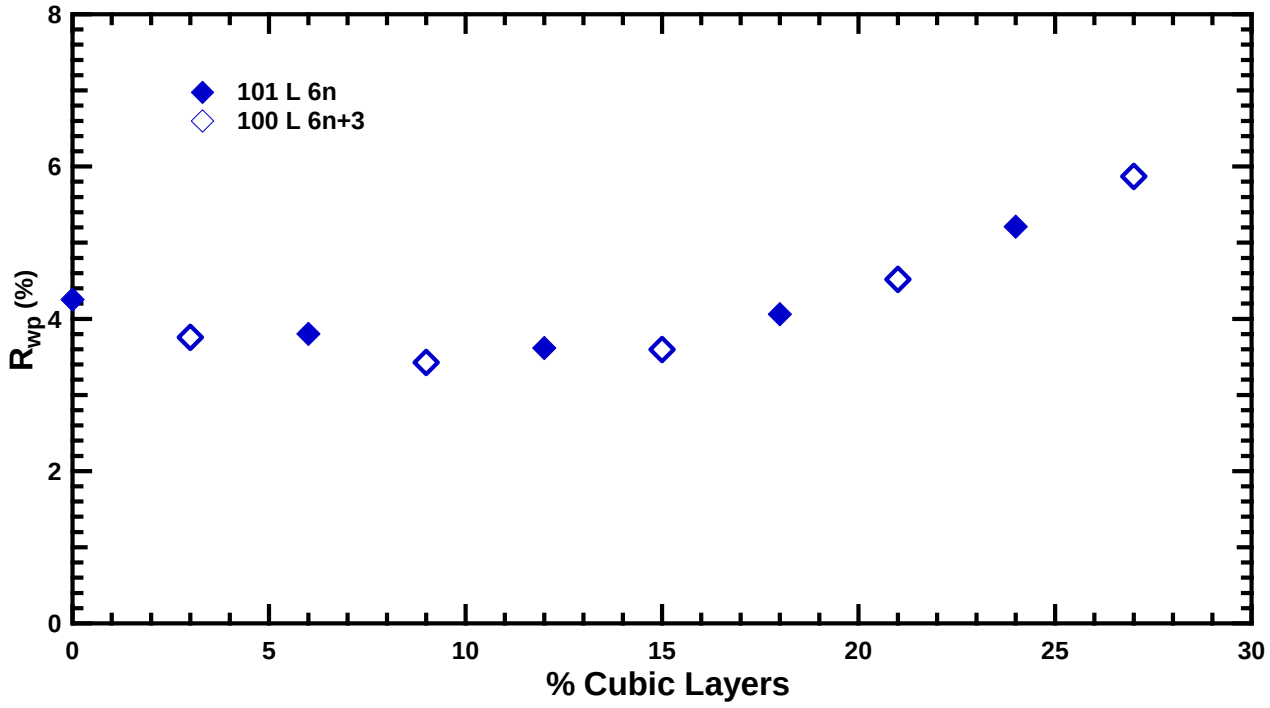

Figure 3.6. R_{wp} vs. % cubic layers of 100/101 total layer supercells with varying number of cubic layers. Fully cubic supercell gave rise to R_{wp} ~ 17.5.

An improved approach to separately obtaining information about the cubic fraction (P1) and the size of the block width (P2) was carrying trials in which the cubic block width (C) was fixed while the size of the entire superstructure (L) was varied. In order to permit the ccp slab width to be incremented

in steps of one (C = 1, 2, 3, .. 12) rather than steps of three, the superstructure contents were doubled to consist of two identical width ccp slabs and two equal or nearly equal hcp slabs. The results of these series of trials were then combined into a single plot summarizing the results of ~75 independent Rietveld refinements (Figure 3.7), from which the local minimum R_{wp} for each size cubic slab could be determined together with the global minimum R_{wp} for all sizes of C. It can be seen that the different width cubic slabs generally give very different local minima, confirming that good knowledge of the layer width is required in order to obtain an accurate measure of the overall ccp fraction. The lowest R_{wp} values are generally seen for ccp fractions of 7 – 14 %, with the lowest R_{wp} obtained for cubic slab widths of C = 4.

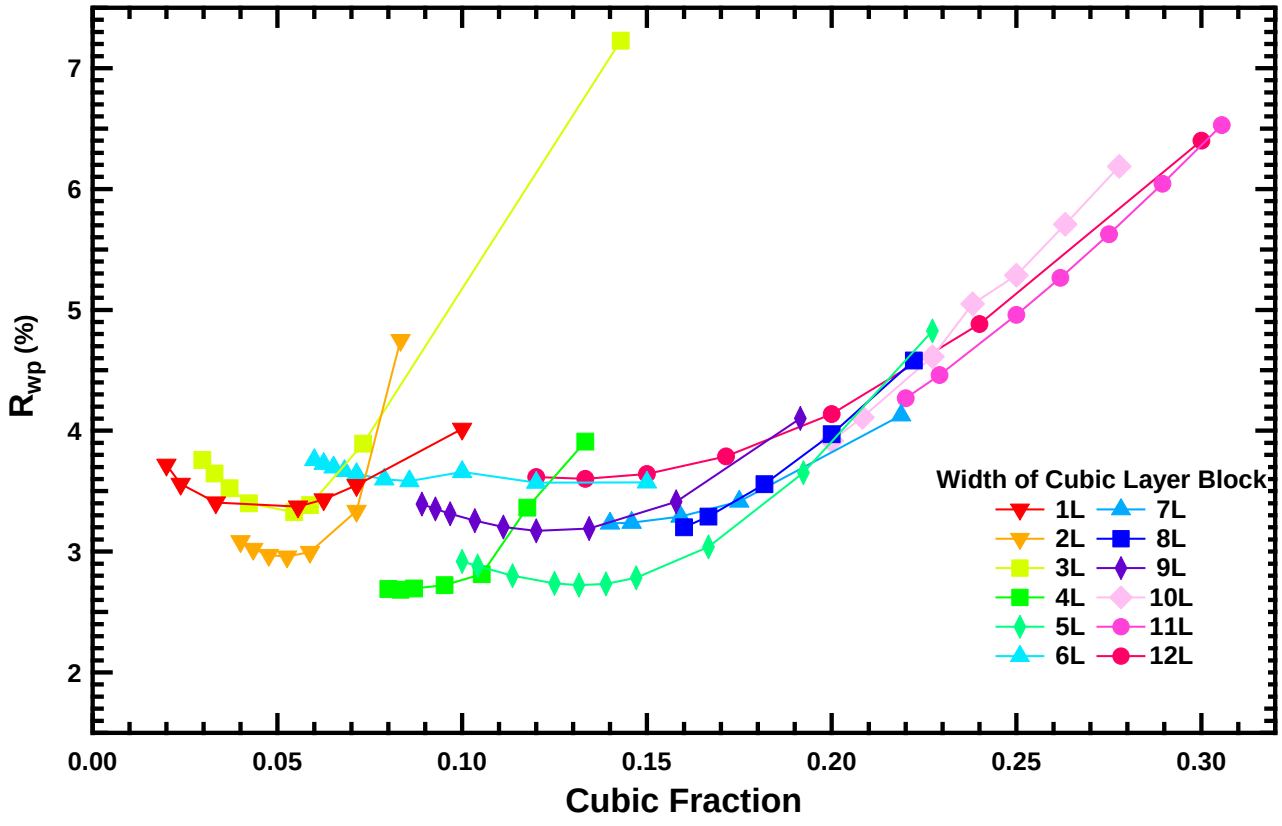

Figure 3.7. Plot of R_{wp} vs. cubic fraction from fixing cubic block width (double blocks are used) in range of 1 to 12 layers and varying the total number of layers in the supercell.

While this method of analysis gives some very good general insights, a close inspection of the results shows two potential limitations of this approach. First of all, the minimum ccp fraction which can be probed scales linearly with the block width. In the 100 or 101 layer supercells used for the double-slab studies of Figure 3.7, the minimum cubic fraction that can be probed starts at 2% for a 1 layer ccp slab but rises to 10% by the time $C = 5$ and rises to 24% for a $C = 12$. Second, it can be seen that the R_{wp} values for layers with $C = 3n$ appear to be substantially larger than those with $C \neq 3n$, and thus R_{wp} varies non-monotonically with C. Alternate modeling methods have been developed to circumvent both of these limitations.

The non-monotonic behavior with respect to C indicates that structural factors indirectly impacted by the cubic block width (but which are not associated with scattering from the cubic slab) can strongly affect the quality of the fit. This suggests the interactions between hexagonal slabs on opposite sides of a cubic slab are particularly poorly modeled when $C = 3n$. A review of Table 3.4 shows that the $C = 3n$ cases represent the only two of the six possible translations between hcp blocks in which the same close-packed positions are utilized on both sides of the ccp slab (**AB→AB** due to a 0+ shift of the ccp slab, or an **AB→BA** transition due to a 1- shift). Although we cannot directly investigate the effect of different hcp/hcp interactions for the same width of cubic layers using physically plausible trial structures due to the geometric limitations inherent in the construction of valid mixed closed packed structures, the influence of hcp/hcp interactions on diffraction patterns can be directly probed using trial structures which are aphysical.

Three different types of aphysical structures were used to test the influence of the hcp/hcp translation on the refinement R_{wp} for trial structures. In all cases, the intervening cubic slabs were held constant while the hcp translations were varied. All trials were done using an $L = 84$ double block structure with a 36/6/36/6 block pattern of cubic slabs with W = 6 and very thick intervening hcp slabs. The six different transitions between a hcp slab with a second hcp slab with an AB repeat pattern were

artificially introduced into these structures using the three different violations of the stacking rules illustrated in Figure 3.8. First, all six ccp layers were left empty (**VVVVVV**), leaving only scattering from the hcp atomic sites. Second, the first five ccp layers were built up as expected (**CABCAV**) for cubic layers following AB type hcp layers while the final sixth ccp layer was left empty to avoid a stacking fault at the tail end of the ccp slab. Third, all six layers in the nominal ccp slab were fully occupied in the expected pattern (**CABCAB**) without regard to the fact that the sixth layer is actually ccp for only 1/3 of the choices of the starting position of the following hcp slab, and is otherwise hcp (1/3 of time) or even prismatic (1/3 of the time), and that the first layer of the following hcp slab is also suffers from the same type of interface problems. However, these defects only affect at most 4% of the total layers in the supercell, and thus should have a minimal impact on the overall Bragg diffraction pattern calculated for these aphysical trial structures.

physical	aphysical		
	#1	#2	#3
A	A	A	A
B	B	B	B
C	V	C	C
A	V	A	A
B	V	B	B
C	V	C	C
A	V	A	A
B	V	V	B
A	X	X	X
B	X	X	X

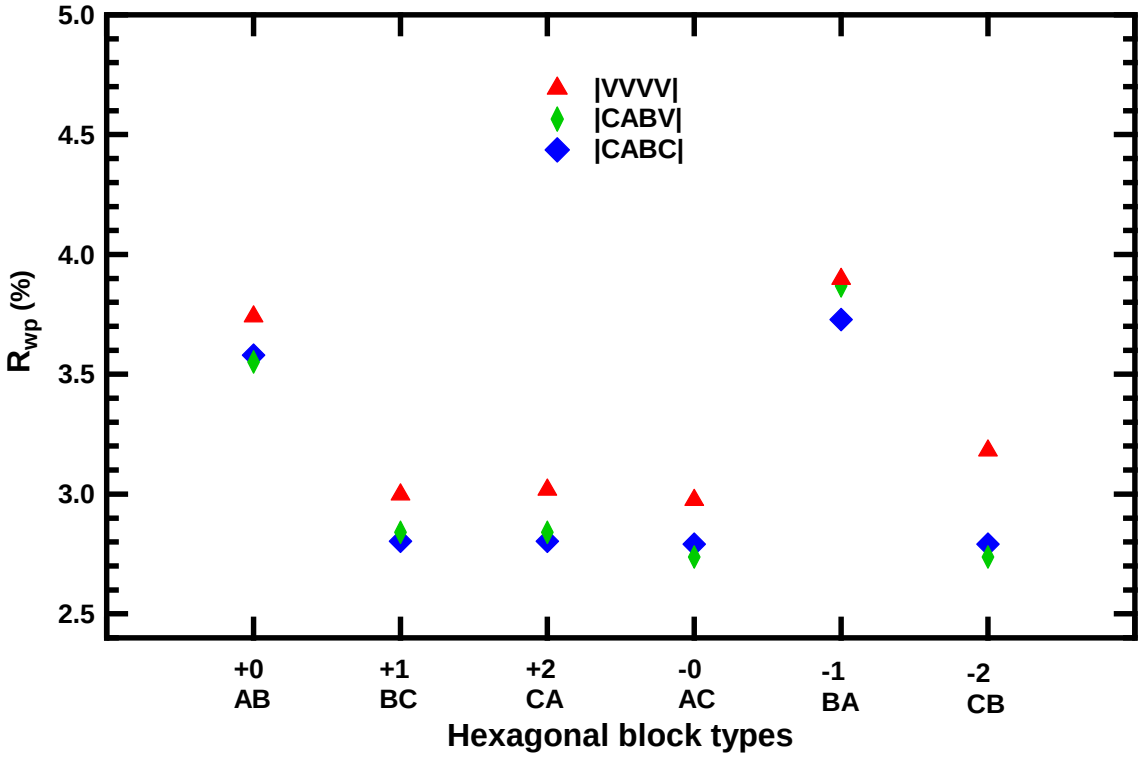

Figure 3.8. Diagram of physical and aphysical 6L cubic block manipulations. XX symbolize the 6 different transitional hexagonal block layer types; AB, BA, CA, AC, BC, CB (top). Results of cubic block aphysical model manipulations using 4L blocks (below).

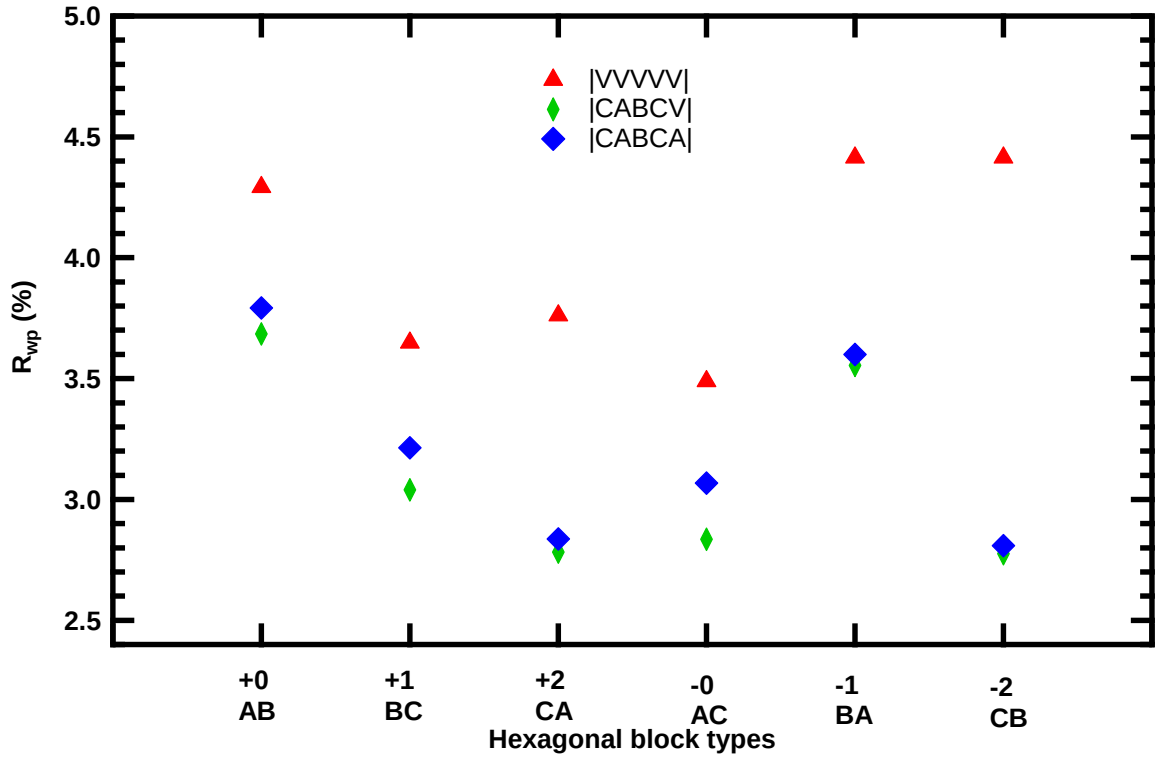

Figure 3.9. Results of cubic block aphysical model manipulations using 5L cubic double block model.

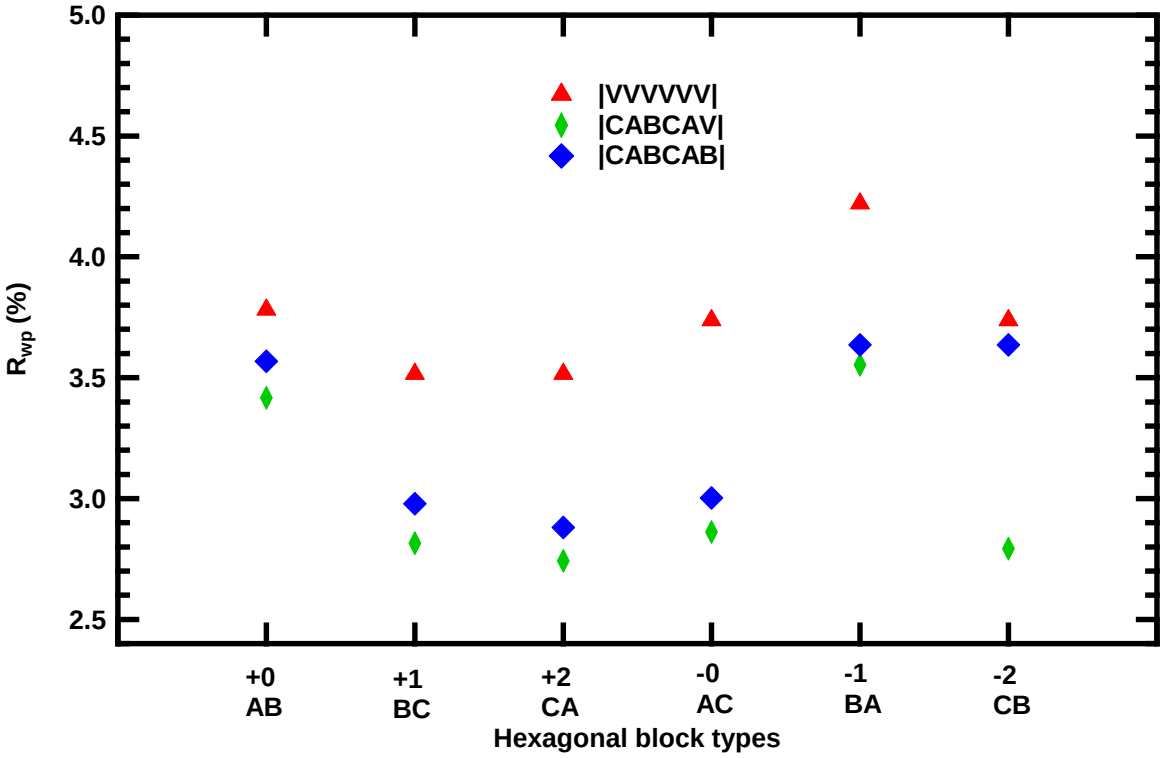

Figure 3.10. Results of cubic block aphysical model manipulations using 6L cubic double block model.

The results of these trials using aphysical superstructures for cubic slabs with $C = 4$ are given in Figure 3.8, with additional data for $C = 5$ (Figure 3.9) and $C = 6$ (Figure 3.10). The relatively small contribution of the cubic slabs to the quality of the overall refinement is reflected in the similar R_{wp} values found using the three different aphysical models. As expected, the model which has only vacancies in the cubic layers has the highest R_{wp}, though it is only about 0.2% (absolute) higher than for the other two aphysical models for testing hcp/hcp transitions. The nature of the transition has a much larger impact on the overall refinement. The two trial structures with hcp/hcp transitions of **AB→AB** and **AB→BA** have R_{wp} values which are 1% (absolute) lower than that the other four transitions are generally indistinguishable in the quality of their fit. This clearly indicates that effectively modeling the majority hcp layers is more important than effectively modeling the minority ccp layers, and that the anomalous behavior observed in Figure 3.7 for the $W = 3n$ layers was due to the particularly poor models for the hcp layers that resulted from from the limited set of hcp positions implied by the ccp layer widths.

These aphysical models offer the best possibility for distinguishing between the relative quality of the fits for cubic layers with W = 4 to 6. A comparison of these fits suggests that the best results are obtained when W = 4. This is shown in both the aphysical and physical modeling of supercells (Figures 3.8 and 3.9). However, it is important to keep in mind that these superstructure models provide better approximants of the sample structure than the 2-layer wurtzite unit cell, but are still approximants. It is therefore very possible that the average width of $C = 4$ reflects a mixture of layers which are both wider and narrower.

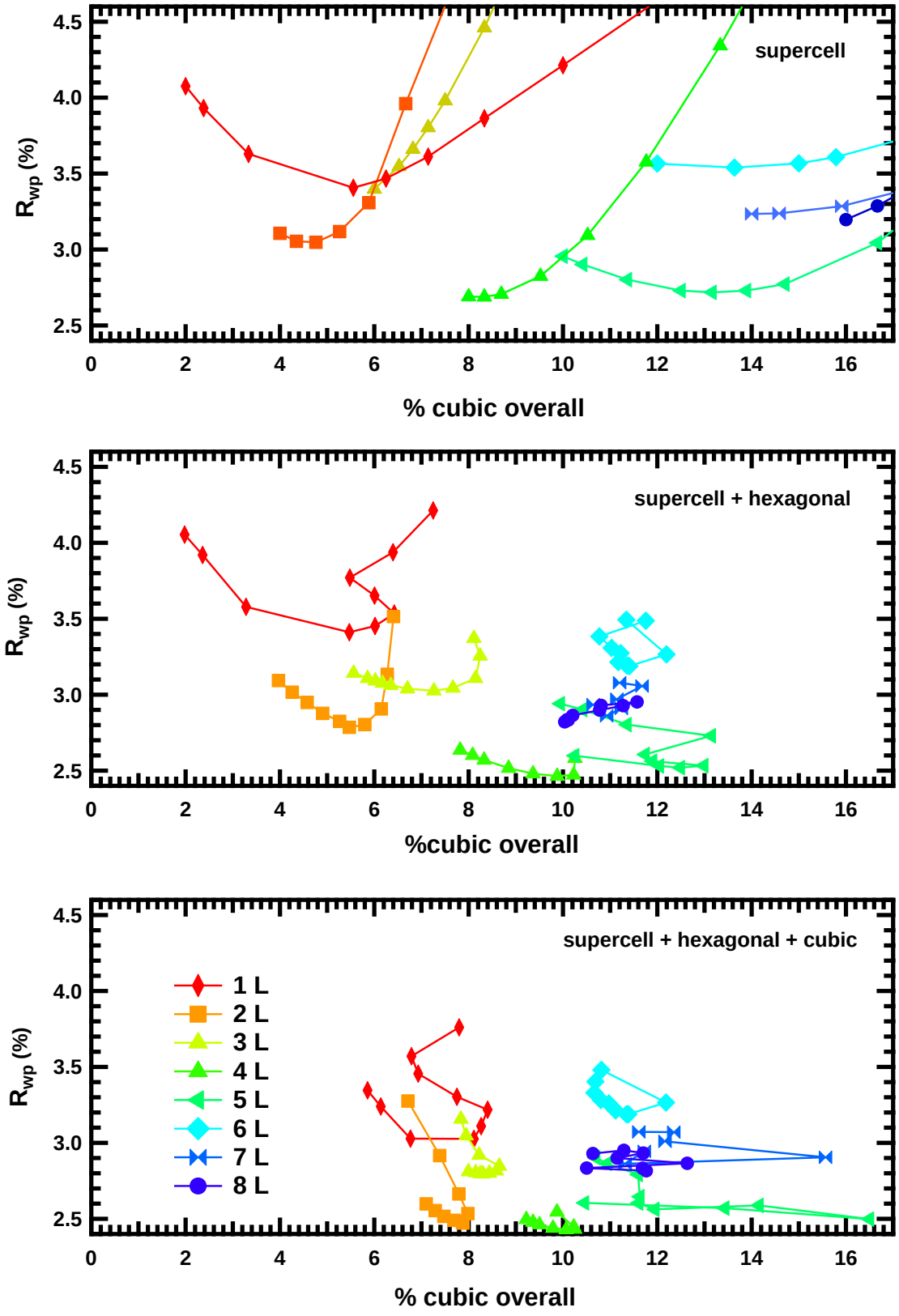

Figure 3.11. One, two, and three phase model results of 100 layer supercells with double cubic block regions ranging in width from 1L to 8L.

When the optimal layer width of $C = 4$ is used with a double-block supercell of maximal width (L ~ 120 layers), the minimum cubic fraction that can be tested is unfortunately only about 6.7%. In order to test for the presence of smaller fractions of the cubic phase, 2-phase refinements were carried out in which one phase is an explicit supercell and the other is a purely hcp wurtzite phase in its standard two-layer unit cell. By allowing the superstructure phase to be diluted, it is possible to gain sensitivity to much smaller fractions of the cubic phase, and to reduce the influence of the specific superstructure choice on the refined cubic fraction. Two-phase refinements were therefore carried out for structures with ccp slabs with widths of 1 to 8 layers. It is important to note that the addition of a second phase added to the computational limitations for supercell size and decreased the maximum width of the supercell (L = 100 layers). Furthermore, a variety of different sizes of double-block superstructures were investigated ($12 < L < 100$), in order to assess the sensitivity of the refinement results to the details of the trial superstructure. The results of these refinements are graphed in Figures 3.11 and 3.12.

From Figure 3.11, it can be clearly seen that the 2-phase refinements (middle panel) on the whole give better fits than the 1-phase refinements (top panel). This can be seen in both the improved overall fits (lower R_{wp} values) and in the enhanced sensitivity to the layer width (cluster narrowly when plotted as % cubic). This methodology can also be extended to a 3-phase refinement, in which the superstructure model is refined together with the average structures of both the hexagonal wurtzite and cubic zinc blend polymorphs. While the addition of a purely hexagonal wurtzite phase in 2-phase refinements allows the cubic fraction to be reduced as needed, the use of a purely cubic zinc blende phase in the 3-phase refinement allows the cubic fraction to also be increased if needed. As such, the third phase most strongly impacts the trial structures with low cubic fractions ($W \leq 3$), and increases the refined cubic fraction for these trial structures up to 7 – 8%. The 3-phase approach further narrows the refined distribution of the cubic fraction across the various trial structures, with the values generally

concentrated in the range of 7 – 12 %, and this value should provide a good measure of the actual properties of the present sample of $(GaN)_{1-x}(ZnO)_x$.

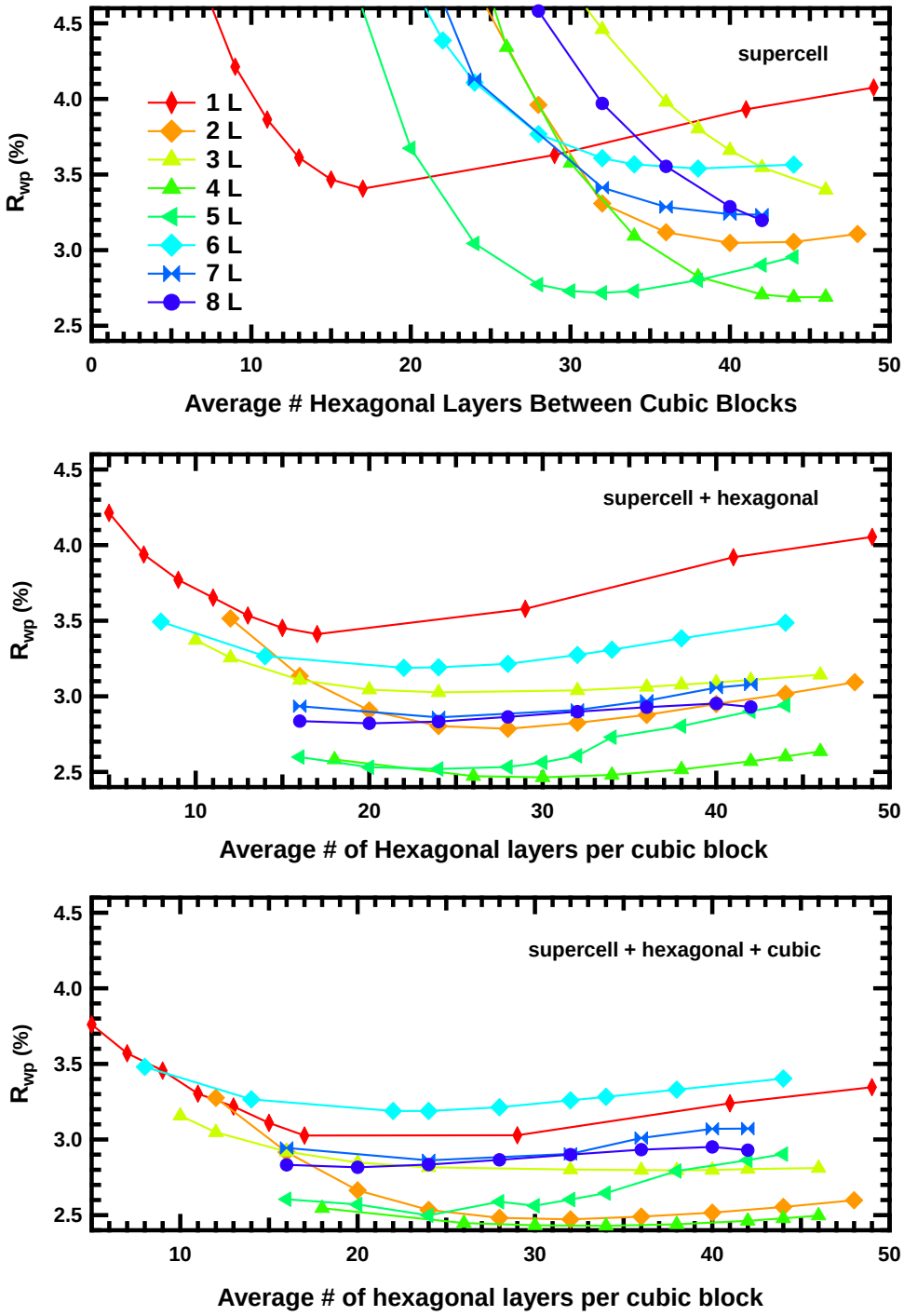

Figure 3.12. One, two, and three phase model results of 100 layer supercells with double cubic block regions ranging in width from 1L to 8L represented as a function of hexagonal block width.

The reason for the strong dependence of the refined cubic fraction on the layer width can be understood when these Rietveld refinement results are plotted with the hexagonal slab width (*H*) as the horizontal axis, as shown in Figure 3.12. The minimum R_{wp} for both 2-phase and 3-phase refinementsis robustly obtained for hcp slab widths of ~30 layers (or alternatively, ~8 nm), and shows much less dependence on the width of the cubic slab. This likely reflects the coherence length for the hcp stacking before being perturbed by stacking faults. The refinement may therefore exhibit good sensitivity to this parameter due to the hcp layers being the major component of this phase, and due to the substantially different diffraction patterns between fault-free and faulted hcp layers, as was seen in Figure 3.8. In contrast, the 1-phase refinements are insensitive to the width of the hexagonal layers (P3) since this parameter cannot be varied independently of the cubic fraction (P1) when refinements are carried out in this manner.

3.3.4. Optimized final fit to $(GaN)_{0.65}(ZnO)_{0.35}$

The approaches described in the previous sections enabled good initial estimates of both the fraction of the ccp layers and width of the cubic intergrowths. Based on these insights, the final modeling of $(GaN)_{0.65}(ZnO)_{0.35}$ was carried out using a double-block superstructure with cubic slabs that are four layers thick. Although a number of constraints (equal thickness for all layers, common offsets between the cation and anion position in all layers) were implemented in the preliminary trials across different ccp layer widths and fractions to ensure that the refinements were primarily sensitive to these parameters, these constraints were relaxed in the final analysis. Different parameters were assigned for three types of close-packed layers within the structure: those inside hcp slabs (hh), those inside ccp slabs (cc), and those at the interface between hcp and ccp slabs (hc), with the parameters for the hc interfaces constrained to be the average of the hh and cc layers. This superstructure model was tested for 1-phase (R_{wp} = 2.690, 8.0% ccp), 2-phase (R_{wp} = 2.636, 7.8% ccp), and 3-phase (R_{wp} = 2.496, 9.2% ccp) Rietveld refinements, as shown in Figure 3.13a. The differences between these three refinements are

small. This is because the basic superstructure model fortuitously has both a nearly correct cubic fraction and hcp slab width, though it is believed that the 3-phase refinement is most representative of the true behavior of $(GaN)_{0.65}(ZnO)_{0.35}$. Previous 3-phase refinement trials for C = 4 cubic slabs embedded in a wider range of total superstructure widths (Figure 3.8) gave a cubic fraction clustered between 9.0 and 10.5 %, and was in the midpoint of the 7 – 12 % range of cubic fractions refined across all trial ccp slab widths. This gives us additional confidence that the phase fraction of 9.2% obtained in the final 3-phase structural model is very likely representative of the true sample properties.

The structural model obtained from this three-phase refinement is therefore the optimal model for the final structural analysis of $(GaN)_{0.65}(ZnO)_{0.35}$. It can be seen that the stacking fault model provides a very substantially improved fit (R_{wp} = 2.50%) relative to alternative fits using a fully relaxed average structural model (R_{wp} = 4.21%), and even to an average structural model with the minority sites associated with stacking faults explicitly added in (R_{wp} = 3.78%), as shown in Figure 3.13. Thus the explicit superstructure effectively captures the coherence of interactions between hcp and ccp layers, as well as the coherence between hcp and hcp layers. The latter are particularly important, as refinements greatly improved relative to the average structure models can be obtained even when completely omitting scattering from all of the atom sites in the ccp layers but still preserving the shifts in hcp layers that the ccp intergrowths induce (R_{wp} ~ 3.0%).

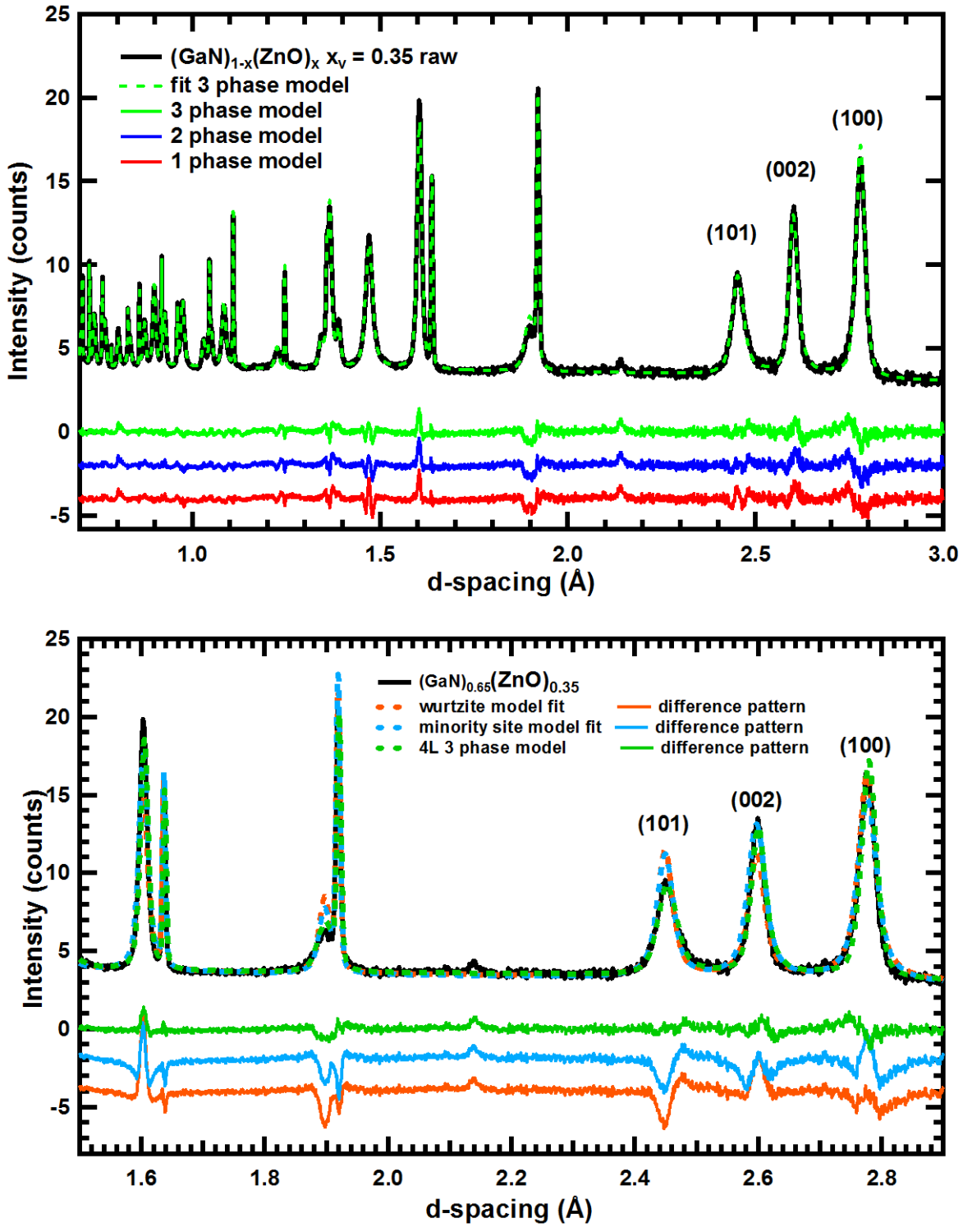

Figure 3.13. (top) Neutron diffraction pattern of $(GaN)_{1-x}(ZnO)_x$ $x_v = 0.35$ with one ($R_{wp} = 2.690$), two ($R_{wp} = 2.636$), and three ($R_{wp} = 2.496$) phase fitting results of Rietveld refinements. (bottom) Neutron diffraction pattern of $(GaN)_{1-x}(ZnO)_x$ $x_v = 0.35$ with normal wurtzite model ($R_{wp} = 4.214$), wurtzite with added minority sites model ($R_{wp} = 3.779$), and 4L double cubic block 3 phase optimal model ($R_{wp} = 2.496$).

The refined crystallographic parameters from the 3-phase refinement are provided in Tables 3.5 and 3.6. For the binary compounds GaN and ZnO, slight differences exist in the layer height inferred for the hexagonal wurtzite and cubic zinc blende polytypes. A normal wurtzite GaN layer height would be half of its c lattice parameter, or 2.598Å while a zinc blende GaN layer height is slightly larger at 2.769Å. The 3-phase Rietveld refinement of $(GaN)_{0.65}(ZnO)_{0.35}$ indicates that the internal ccp layers (cc) are about 0.01 Å thicker than the internal hcp layers (hh). This result is robustly obtained over many trial refinements for this specific phase, and is also observed for similar refinements of $(GaN)_{1-x}(ZnO)_x$ samples with other compositions. It therefore appears that this method of explicit refinement of large supercell structural models is able to provide precise insights into the internal coordinates of atoms within the layers, as well as important providing broader insights into the nature and abundance of stacking faults. As such, the methods described in this manuscript provide very powerful tools for understanding complex materials which are not appropriately described using an average structural model due to the effects of stacking faults.

Table 3.5. Refined lattice parameters and weight percents of phases in 3 phase optimal 4L fit (Si wt% = 32.4(5) not shown).

4L double block 3 phase fit $(GaN)_{0.65}(ZnO)_{0.35}$ R_{wp} = 2.483 Space group P3			
phase	supercell	hexagonal	cubic
a (Å)	3.2083(9)	3.2078(5)	3.216(1)
c (Å)	259.87(2)	5.198(3)	7.7964(5)
wt %	63.8(6)	2.1(1)	1.5(6)

Table 3.6. Parameter results of Rietveld refinement using 3 phase 4L optimal fit to $(GaN)_{0.65}(ZnO)_{0.35}$.

4L double block 3 phase fit $(GaN)_{0.65}(ZnO)_{0.35}$ R_{wp} = 2.483 Space group P3			
phase	supercell	hexagonal	cubic
hh	2.596(8)	2.596(8)	--
hc	2.597(4)	--	--
cc	2.599(8)	--	2.599(8)
B_{eq} Ga/Zn	0.19(8)		
B_{eq} N/O	0.73(9)		
Ga/Zn *hh z* offset	0.7527(7)		
Ga/Zn *hc z* offset	0.771(6)		
Ga/Zn *cc z* offset	0.8(1)		

3.4. Conclusions

It is demonstrated that the use of explicit superstructures can provide very detailed insights into structures with minority stacking faults, allowing both the abundance of the faults and the width of the faulted blocks to be determined. Although these parameters cannot be obtained from a single Rietveld refinement, they can be very effectively deduced when a series of refinements are carried out on trial structures including both physical and aphysical stacking models. A set of stacking rules for constructing minimally sized periodic structures have been identified. Furthermore, it is shown that multi-phase refinements can provide computational advantages for investigating both small and large components of the minority layer types. The methods can now be applied to investigate the systematic dependence of stacking fault abundance on the composition and synthesis method of the important class of visible-light absorbing $(GaN)_{1-x}(ZnO)_x$ semiconductors, and other layered structures which are important for a variety of technological applications (batteries, optoelectronics, thermoelectrics, superconductors, etc.).

Cubic block width	AB Hex block	Cubic block	Transition Hex block	Cubic block
6L	ABABAB	CABCAB	BCBCBC (+1)	CABCAB
			CBCBCB (-2)	
			ACACAC (-0)	
			CACACA (+2)	
			ABABAB (+0)	
			BABABA (-1)	
		CABCAV	BCBCBC (+1)	VABCAB
			CBCBCB (-2)	
			ACACAC (-0)	
			CACACA (+2)	
			ABABAB (+0)	
			BABABA (-1)	
		VVVVVV	BCBCBC (+1)	VVVVVV
			CBCBCB (-2)	
			ACACAC (-0)	
			CACACA (+2)	
			ABABAB (+0)	
			BABABA (-1)	
5L	ABABAB	CABCA	BCBCBC (+1)	CABCA
			CBCBCB (-2)	
			ACACAC (-0)	
			CACACA (+2)	
			ABABAB (+0)	
			BABABA (-1)	
			BCBCBC (+1)	
		CABCV	BCBCBC (+1)	VABCA
			CBCBCB (-2)	
			ACACAC (-0)	
			CACACA (+2)	
			ABABAB (+0)	
			BABABA (-1)	
		VVVVV	BCBCBC (+1)	VVVVV
			CBCBCB (-2)	
			ACACAC (-0)	
			CACACA (+2)	
			ABABAB (+0)	
			BABABA (-1)	

Table S3.1. 6L and 5L cubic block manipulation explanations.

AB Hex block	Cubic block	Transition Hex block	Cubic block
ABABAB	CABC	BCBCBC (+1)	CABC
		CBCBCB (-2)	
		ACACAC (-0)	
		CACACA (+2)	
		ABABAB (+0)	
		BABABA (-1)	
	CABV	BCBCBC (+1)	VABC
		CBCBCB (-2)	
		ACACAC (-0)	
		CACACA (+2)	
		ABABAB (+0)	
		BABABA (-1)	
	VVVV	BCBCBC (+1)	VVVV
		CBCBCB (-2)	
		ACACAC (-0)	
		CACACA (+2)	
		ABABAB (+0)	
		BABABA (-1)	

Table S3.2. Manipulation of sequences for 4 layer cubic block width. X is indicative of a purposely created vacancy in the supercell

Chapter 4

Quantification of cubic intergrowths using supercell models in Rietveld refinements on $(GaN)_{1-x}(ZnO)_x$ $x = 0.10 - 0.95$

4.1 Introduction

The $(GaN)_{1-x}(ZnO)_x$ solid solution system is well known as having the wurtzite structure which is based on hexagonal close packed layers, as maintained from its end members GaN and ZnO. However, previous transmission electron microscopy studies of $(GaN)_{1-x}(ZnO)_x$ samples synthesized from a $ZnGa_2O_4$ precursor showed evidence of zinc blende (cubic close packed) type intergrowths in abundance. These intergrowths have been shown to exist without the addition of Bragg peaks in powder diffraction patterns expected for a zinc blende structure type. A detailed analysis on the quantification of this intergrowth in a $(GaN)_{0.65}(ZnO)_{0.35}$ sample using a supercell approach implemented into a bulk Rietveld refinement analysis was discussed in the previous chapter. The analysis shed light on optimal superstructure sequencing and width of cubic fault. A set of stacking rules for constructing periodic structures, based on earlier studies of stacking sequences, was created for this type of superstructure modeling and will be used in this study.

For the specific case of $(GaN)_{0.65}(ZnO)_{0.35}$ it was discovered that the average width of a cubic close packed type intergrowth is about 4 layers and that these intergrowths make up approximately 9% of the sample. In all preliminary studies it was shown that 4 and 5 layer cubic block widths were optimal in modeling neutron diffraction patterns, and therefore will act as the starting points for modeling samples shown here $x = 0.10 – 0.95$. In particular we implement the previously optimized supercell type modeling on a number of $(GaN)_{1-x}(ZnO)_x$ samples produced from both a common $ZnGa_2O_4$ and a newly implemented layered double hydroxide (LDH) precursor. This study aims to probe the versatility of this model and its ability to be applied to multiple samples, and also to investigate correlations between sample and amount of intergrowth present.

4.2 Experimental

4.2.1 Synthesis of $(GaN)_{1-x}(ZnO)_x$

$Ga_2O_3(ZnO)_m$ phases were carried out by mixing stoichiometric amounts of Ga_2O_3 (Alfa Aesar, 99.999%) and ZnO (Alfa Aesar, 99.99%), grinding with an agate mortar and pestle, and placing the mixture in a dense alumina crucible (CoorsTek). The m = 16 phase used as a precursor for $(GaN)_{1-x}(ZnO)_x$ syntheses was obtained by reacting stoichiometric amounts of Ga_2O_3 and ZnO (1:16) in a sealed alumina tube held at 1350 °C (1623 K) under flowing oxygen (~60 ml / min) for a total of 144 h with intermediate grinding steps every 48 h to promote reactivity and product homogeneity. Conversion of the $Ga_2O_3(ZnO)_{16}$ precursor into a wurtzite oxynitride was typically done at 1123 K under NH_3 flow (5mL/min) for times of 10-18 h, resulting in single phase wurtzite samples with varying zinc contents. After heating, the sample was cooled to room temperature under NH_3 flow and the tube was then purged with N_2 gas prior to sample removal.

$ZnGa_2O_4$ samples were obtained by reacting stoichiometric amounts of Ga_2O_3 and ZnO (1:1) in a box furnace held at 1000 °C (1273K) in air for a total of 24h with an intermediate grinding after 12 hr to promote reactivity and product homogeneity. Conversion of the $ZnGa_2O_4$ precursor into a wurtzite oxynitride was typically done at 1123K under NH_3 flow (5mL/min) for times of 10-18h, resulting in single phase wurtzite samples with varying zinc contents. After heating, the sample was cooled to room temperature under NH_3 flow and the tube was then purged with N_2 gas prior to sample removal. Higher zinc contents were synthesized with the aid of ZnO powder placed upstream from the sample boat during reactions to allow the vapor pressure of zinc to increase above the sample and settle into the sample. The use of a $ZnGa_2O_4$ precursor alone limits the zinc content of a synthesized $(GaN)_{1-x}(ZnO)_x$ to a maximum of $x = 0.33$.

Syntheses of $Zn/Ga/CO_3$ layered double hydroxides (LDHs) were carried out by dissolving stoichiometric gallium (III) nitrate (Alfa Aesar, 99.9%) and zinc nitrate (Alfa Aesar, 99%) in distilled

water to obtain a Zn^{2+}/Ga^{3+} solution. Sufficient Na_2CO_3 was added to ensure precipitation and NaOH was added until the pH reached approximately 8.0. The solution was allowed to precipitate at 85 ℃ for 6-12 hours with stirring followed by filtering of the precipitate and washing with hot de-ionized water. Finally the remaining sample was allowed to dry in air at 80 ℃ overnight. To synthesize $(GaN)_{1-x}(ZnO)_x$ samples, $Zn/Ga/CO_3$ LDHs were placed in a quartz boat in the hot zone of a tube furnace at 800 ℃ (1073 K) along with ZnO powder in another boat further upstream with a NH_3 flow rate of 10 ml/min. Both of the boats are contained in a one-side sealed reaction tube that is sealed on the downstream side. Reactions times ranged from 5-10h.

4.2.2 Powder X-ray diffraction

Progression of reactions was monitored using X-ray powder diffraction on a Bruker D8 Advance laboratory diffractometer (Cu K_α λ = 1.54059Å, 7-120° 2θ, 0.02 step size, 300 mm radius, 12 mm variable slits, 2.5º Soller slits and a 192-channel Lynx-Eye 1D position sensitive Si detector). Scans for phase identification were done at a rate of 0.1s/step (19.2 s/point) while Rietveld scans were collected using a scan rate of 3 s/step (576 s/point). Zero background silicon slides were used as sample holders. The JADE software package (Materials Data, Inc.) was used for preliminary unit cell refinements and for phase identification. Rietveld refinements were carried using TOPAS v4.2 (Bruker AXS)

4.2.3 Powder neutron diffraction

Neutron diffraction experiments were conducted on the NOMAD instrument at Oak Ridge National Laboratory. The high-resolution total-scattering powder diffractometer is located 19.5 meters from the moderator and has a wavelength range of 0.1 – 3Å. The instrument has 6 banks of detectors with an angular scattering range of 3 – 175°. With a Q range of up to 50Å and a δQ/Q of 0.8% this instrument provides high resolution data and is the fastest data acquisition measurement instrument for pair distribution function analysis. Samples were packed in 3mm quartz capillary tubes, were typically 50mg – 300mg in mass, and were collected twice each for 45 minutes at room temperature.

4.3 Results and Discussion

4.3.1 Implementation of supercell model on $(GaN)_{1-x}(ZnO)_x$ from $ZnGa_2O_4$ precursor

The purpose of this study is to use superstructure modeling on multiple samples and to study its application to samples synthesized from varying precursors. From preliminary studies in Chapter 3 and observations on intergrowth width by TEM, it was decided that 4L, 5L, and 6L cubic width supercells be implemented for samples in this study. It is important to note that due to computational limitations from multi-bank data and multi-phase modeling, a maximal supercell of size 80 layers was used in this work for multiphase fitting.

As a reminder of stacking sequence, layers are labeled as **A** (1/3, 2/3, *z*), **B** (2/3, 1/3, *z*), or **C** (0, 0, *z*) where **ABAB** layering represents hexagonal close packing and **ABC** layering represents cubic close packing. The 80 layer superstructures were created with either 4L, 5L, or 6L double cubic blocks and were tested first among $(GaN)_{1-x}(ZnO)_x$ samples synthesized from a typical $ZnGa_2O_4$ precursor. As in previous studies, B_{eq} values for Ga/Zn are constrained to be equal in all phases, as are B_{eq} values for N/O. The *c* lattice parameter is dependent on interlayer spacings (*hh, hc, cc*) and is calculated based on these values and the total number of layers in the structure. Before moving towards using the superstructure models for these samples, a typical 4 atom wurtzite structure model was implemented into Rietveld refinements. The results to these fits are shown in Table 4.1. As a first approximation it seems the higher zinc content samples may not contain as much, or any, intergrowth at all due to their better fit value as compared to lower zinc content samples. In order to test this, our 4L, 5L, and 6L superstructure models were used for Rietveld refinements of all samples involved. The overall fit as a function of R_{wp} (%) of samples synthesized from a $ZnGa_2O_4$ precursor to the three selected model types for this study are shown in Table 4.2 and the refined values for each phase fractions weight percent are available in Table 4.3. By allowing our separate phases to refine but with particular constraints, the weight percent of each individual phase was calculated. With this information we were able to calculate

the overall percentage of cubic intergrowth in each sample (Table 4.3). What we find is that samples with $x < 0.30$ tend to have approximately 10% cubic intergrowth, which is comparable to studies of $x = 0.35$. Samples with $x = 0.43$ and 0.49 calculate to have much smaller cubic fractions. It clearly shows the advantage of using a three phase model versus a supercell structure model alone. In addition, we again see similar values for 4L versus 5L superstructure models and can discard a 6L superstructure model as a viable candidate for modeling these samples. To hold with the previous study on $(GaN)_{0.65}(ZnO)_{0.35}$ we will focus on using a 4L three phase model for these samples and are encouraged by the R_{wp} values that this is a valid decision.

Table 4.1. Rietveld refinement results using normal hexagonal wurtzite unit cell model on samples synthesized from a $ZnGa_2O_4$ precursor.

Hexagonal Wurtzite Unit Cell Model	
$(GaN)_{1-x}(ZnO)_x$	R_{wp}
x = 0.10	7.378
x = 0.30	7.909
x = 0.43	4.805
x = 0.49	4.975

Table 4.2. Rietveld refinement results, R_{wp} (%), for 4L, 5L, and 6L wide cubic block widths using one, two, and three phase models on samples synthesized using $ZnGa_2O_4$ precursor.

Cubic block width	4L			5L			6L		
$(GaN)_{1-x}(ZnO)_x$	1 phase	2 phase	3 phase	1 phase	2 phase	3 phase	1 phase	2 phase	3 phase
x = 0.10	10.9	3.62	3.32	10.9	3.50	3.44	11.5	4.59	4.52
x = 0.30	11.5	3.20	3.19	11.4	3.32	3.43	12.1	4.68	4.65
x = 0.43	15.47	3.47	3.45	12.7	3.62	3.67	12.8	4.02	4.01
x = 0.49	12.5	3.62	3.62	17.4	3.68	3.83	17.5	4.20	4.17

Table 4.3. Rietveld refinement results of phase specific wt% values and calculated overall % cubic in samples synthesized using a $ZnGa_2O_4$ precursor and using 3 phase models with 4L and 5L cubic block widths.

Cubic block width = 4L				
$(GaN)_{1-x}(ZnO)_x$	wt% supercell	wt% hex	wt% cubic	% cubic overall
x = 0.10	65.64	32.12	2.241	8.81
x = 0.30	79.87	17.61	2.528	10.5
x = 0.43	32.73	66.70	0.562	3.84
x = 0.49	30.14	69.31	0.546	3.56
Cubic block width = 5L				
$(GaN)_{1-x}(ZnO)_x$	wt% supercell	wt% hex	wt% cubic	% cubic overall
x = 0.10	66.62	32.19	1.193	9.52
x = 0.30	67.64	30.54	1.189	9.70
x = 0.43	27.54	72.46	0.002	3.45
x = 0.49	25.593	74.45	0.002	3.20

The powder neutron diffraction patterns of all samples from a $ZnGa_2O_4$ precursor fit using a three phase 4L cubic double block model are shown in Figure 4.1. As a comparison to our starting point for modeling this data, we fit all samples to a normal 2 layer (4 atom) wurtzite structure model (Figure 4.2) and compared it to our best sample fit to a 4L double cubic block superstructure model (x = 0.30). The superstructure model helps to fix a number of peak shape and intensity problems unable to be resolved using a normal wurtzite unit cell model. From this overlay of fits and the R_{wp} values for all samples fit to a wurtzite unit cell model (Table 4.1) we are confident that our superstructure modeling is viable for understanding the size and amount of cubic intergrowths present in samples in this $(GaN)_{1-x}(ZnO)_x$ system.

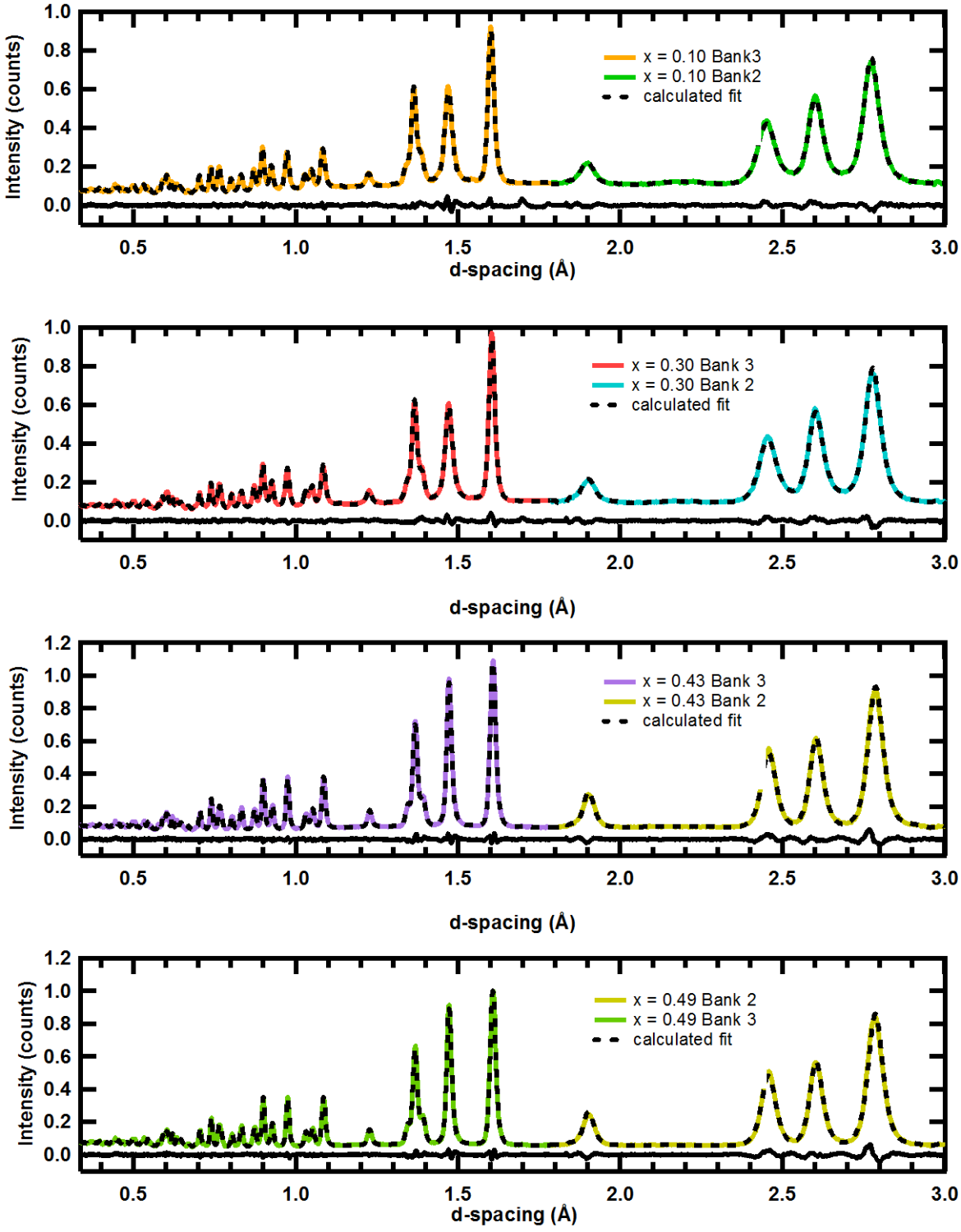

Figure 4.1. Powder neutron diffraction pattern fit of $(GaN)_{1-x}(ZnO)_x$ samples synthesized from $ZnGa_2O_4$ precursor and measured on NOMAD. Full patterns implemented data from banks 2 and 3 and were fit using Rietveld refinement models with optimal 4L double block cubic sections and a three separate phases.

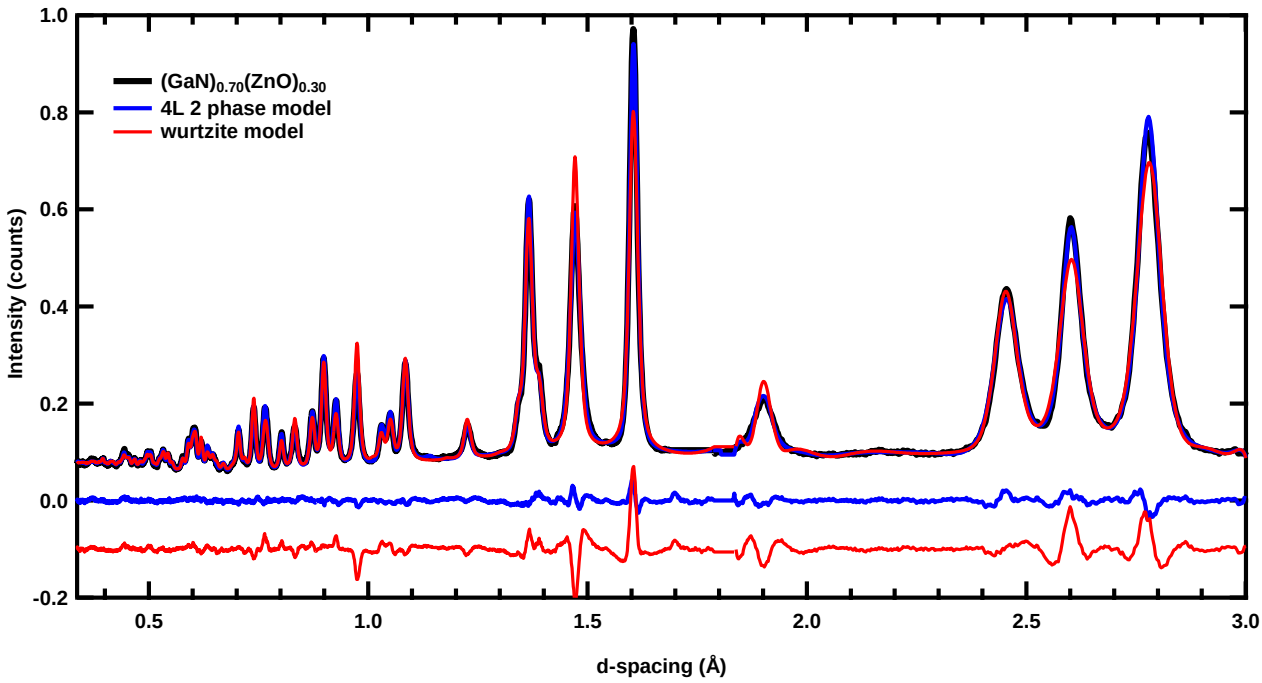

Figure 4.2. Neutron diffraction pattern of $(GaN)_{0.70}(ZnO)_{0.30}$ fit to an optimized 4L double cubic block superstructure and also to a normal wurtzite unit cell structure model showing clear improvement to fit using superstructure model.

Figure 4.3 shows a closer look at a $(GaN)_{0.70}(ZnO)_{0.30}$ sample fit using the 4L superstructure model, along with the differences patterns for all other samples. It seems that this model fits lower zinc content samples $x < 0.30$ better than those of higher zinc content $x > 0.43$. As there are improvements that can be made for particular samples, it is important to note that this is still a clearly improved fit as compared to past studies using a normal wurtzite unit cell model or a wurtzite unit cell model with added minority sites. These models showed clear peak shape and intensity problems for the three major wurtzite peaks, a phenomenon that is taken care of with the use of superstructure models. The refined values of parameters from Rietveld refinements using a 4L double cubic block superstructure can be found in Table 4.4. Automated calculations were used for running refinements with identical and sensible starting values for all refining parameters from sample to sample, as was done in the previous work. The values obtained for the refined parameters are sensible and give us confidence that this is still a plausible model for these samples. While we cannot explicitly say that cubic fraction is dependent on zinc content as of yet, there does seem to be that correlation from this individual study.

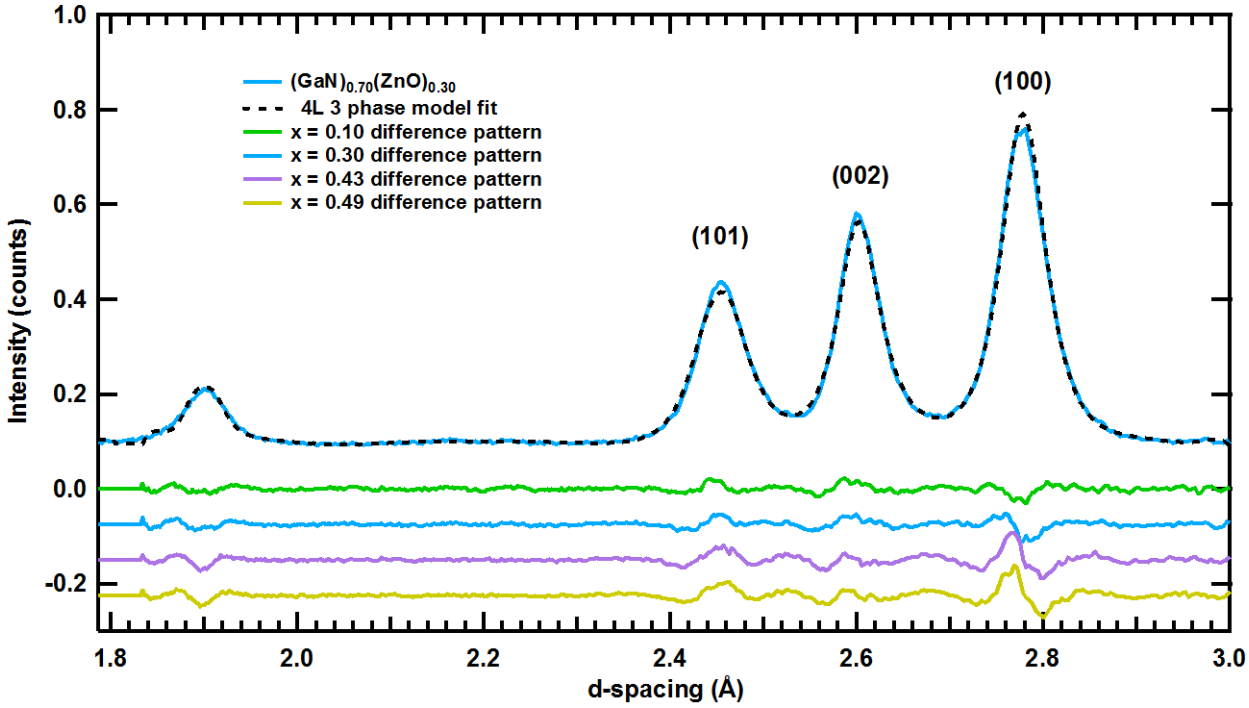

Figure 4.3. Optimal fit to the neutron diffraction pattern of $(GaN)_{0.70}(ZnO)_{0.30}$ using a 4L double cubic block superstructure with separate hexagonal and cubic phases. Difference patterns for three other samples synthesized from a $ZnGa_2O_4$ precursor are shown and complement the poorer R_{wp} values as compared to the x = 0.30 sample.

Table 4.4. Rietveld refinement lattice parameter, interatomic distance, and B_{eq} results of $(GaN)_{1-x}(ZnO)_x$ samples from a $ZnGa_2O_4$ precursor using a 4L three phase superstructure model.

4L double block 3 phase fit results $(GaN)_{1-x}(ZnO)_x$ from $ZnGa_2O_4$ precursor Space group *P3*				
	phase	supercell	hexagonal	cubic
x = 0.10	*a* (Å)	3.1991(3)	3.2100(7)	3.240(2)
	c (Å)	207.84(2)	5.1960(4)	7.7941(6)
	hh	2.5977(1)	2.5977(1)	--
	hc	2.5979(1)	--	--
	cc	2.5980(2)	--	2.5980(2)
	B_{eq} Ga/Zn	0.34(3)		
	B_{eq} N/O	0.64(3)		
x = 0.30	*a* (Å)	3.2062(2)	3.2100(5)	3.240(2)
	c (Å)	207.92(4)	5.1989(4)	7.7983(5)
	hh	2.5987(2)	2.5994(2)	--
	hc	2.5991(3)	--	--
	cc	2.5994(9)	--	2.5994(2)
	B_{eq} Ga/Zn	0.51(3)		
	B_{eq} N/O	0.76(4)		
x = 0.43	*a* (Å)	3.2187(2)	3.2134(1)	3.200(1)
	c (Å)	207.960(8)	5.2027(2)	7.8040(3)
	hh	2.5978(4)	2.5978(4)	--
	hc	2.5995(1)	--	--
	cc	2.6012(7)	--	2.6012(7)
	B_{eq} Ga/Zn	0.54(4)		
	B_{eq} N/O	0.79(4)		
x = 0.49	*a* (Å)	3.2184(3)		
	c (Å)	207.904(8)		
	hh	2.5982(3)	2.5982(3)	--
	hc	2.5988(5)	--	--
	cc	2.5993(1)	--	2.5993(1)
	B_{eq} Ga/Zn	0.52(3)		
	B_{eq} N/O	0.77(3)		

4.3.2 Implementation of supercell model on $(GaN)_{1-x}(ZnO)_x$ from LDH precursor

We are confident that our superstructure models are adequate for $(GaN)_{1-x}(ZnO)_x$ samples synthesized from a $ZnGa_2O_4$ precursor and ranging in zinc content from x = 0.10 - 0.49. In this next section we attempt to implement our superstructure modeling into samples synthesized both with higher zinc content and from a different precursor type (layered double hydroxides). Identical constraints and parameter starting values were used for these samples as before and all three model types were used (4L, 5L, 6L). We again see that a 6L cubic double block width is not optimal for samples and have not included these refinements in this study. We are now entirely confident that this 6L model type is not necessary as we now have proven this for a range of zinc content samples and various precursor types. It is also clear that 3 phase refinements were not necessary for samples produced from LDH precursors. 2 phase refinements were optimal as refinements continuously refined the cubic phase as 0 wt%. This also indicates that all samples from an LDH precursor in this study are expected to have cubic intergrowth contents of < 10% (4L model) or < 12.5% (5L model). A 2 phase model allows for cubic intergrowth amounts of less than in the superstructure model phase with the presence of a purely hexagonal phase added.

Table 4.5. Rietveld refinement results using normal hexagonal wurtzite unit cell model on samples synthesized from an LDH precursor.

Hexagonal Wurtzite Unit Cell Model	
$(GaN)_{1-x}(ZnO)_x$	R_{wp}
x = 0.60	6.181
x = 0.64	4.872
x = 0.81	4.968
x = 0.90	5.142
x = 0.95	5.238

As an initial study all samples were fit using a typical 4 atom (2 layer) wurtzite unit cell model. The results of these refinements are shown in Table 4.5 and indicate a better model is needed to fit the data from these samples. When using our superstructure multi-phase models, by allowing our separate phases to refine but with particular constraints, the weight percent of the two individual phases (supercell and hexagonal 2 layer cell) was calculated. With this information we were able to then calculate the overall percentage of cubic intergrowth in each sample (Table 4.6 and 4.7) for both the 4L and 5L superstructure models. We see a good agreement in cubic percentage from model to model, but in general find an overall better fit to data using the 4L double cubic block model. In addition, we find these higher zinc content samples to contain much lower amounts of cubic intergrowth (~1-3%), if any at all.

Although all samples refined to contain low values of cubic intergrowth amount, we do believe them to be real as long as the normal hexagonal wurtzite unit cell model fit is worse than the superstructure model fit. In order to truly test this hypothesis, the fits to the normal wurtzite unit cell model were compared to superstructure models. From R_{wp} values alone, we question the superstructure models on our x = 0.95 sample, as the superstructure refinement value does not seem to improve. A fit of this sample to a normal wurtzite unit cell along with difference patterns for fits using both a 4L and 5L superstructure model is shown in Figure 4.4. What we find is nearly identical fits for all three models, suggesting that this sample does not behave in the same manner as others studied. Further studies of modeling, perhaps starting over and implementing 1 to 12L cubic block width studies, and electron microscopy should allow us to gain further insights into this particular sample. Conversely, an example of the superstructure model aiding in fit quality can be seen in Figure 4.5. A normal wurtzite model clearly does not fit the data well, and although an optimized fit may not have been found here, improvements have been made by implementing a superstructure type model.

Table 4.6. Rietveld refinement using a two phase 4L cubic block width supercell model on samples synthesized using an LDH precursor.

Cubic block width = 4L				
$(GaN)_{1-x}(ZnO)_x$	supercell + hex R_{wp}	wt% supercell	wt% hex	% cubic overall
x = 0.60	4.23	12.08	87.92	1.21
x = 0.64	4.12	17.87	82.13	1.79
x = 0.81	4.32	11.91	88.09	1.91
x = 0.90	4.54	17.97	82.03	1.80
x = 0.95	6.12	34.18	65.82	3.42

Table 4.7. Rietveld refinement results using a two phase 5L cubic block width supercell model on samples synthesized using an LDH precursor.

Cubic block width = 5L				
$(GaN)_{1-x}(ZnO)_x$	2 phases R_{wp}	wt% supercell	wt% hex	% cubic overall
x = 0.60	3.97	11.91	88.09	1.49
x = 0.64	4.61	12.08	87.92	1.51
x = 0.81	4.43	12.28	87.72	1.54
x = 0.90	4.75	22.96	77.04	2.87
x = 0.95	5.82	45.29	54.71	5.66

Table 4.8. Rietveld refinement lattice parameter, interatomic distance, and B_{eq} results of $(GaN)_{1-x}(ZnO)_x$ samples from an LDH precursor using a 4L two phase superstructure model.

4L double block 3 phase fit $(GaN)_{1-x}(ZnO)_x$ from LDH precursor space group *P3*			
x = 0.60	phase	supercell	hexagonal
	a (Å)	3.2122(6)	3.2279(1)
	c (Å)	208.316(9)	5.2079(2)
	hh	2.6030(4)	2.6030(4)
	hc	2.6047(3)	--
	cc	2.6044(9)	--
	B_{eq} Ga/Zn	0.70(6)	
	B_{eq} N/O	0.95(7)	

x = 0.64	*a* (Å)	3.2404(5)	3.2293(1)
	c (Å)	208.334(8)	5.2084(2)
	hh	2.6036(8)	2.6036(8)
	hc	2.6040(1)	--
	cc	2.6044(3)	--
	B_{eq} Ga/Zn	0.78(8)	
	B_{eq} N/O	1.00(8)	
x = 0.81	*a* (Å)	3.2575(9)	3.2399(1)
	c (Å)	208.376(8)	5.2094(2)
	hh	2.6038(7)	2.6038(7)
	hc	2.6044(5)	--
	cc	2.6049(2)	--
	B_{eq} Ga/Zn	0.76(8)	
	B_{eq} N/O	1.0(1)	
X = 0.90	*a* (Å)	2.563(6)	3.2400(1)
	c (Å)	208.321(8)	5.2080(2)
	hh	2.6032(1)	2.6032(1)
	hc	2.6037(5)	--
	cc	2.6041(1)	--
	B_{eq} Ga/Zn	0.77(8)	
	B_{eq} N/O	1.0(9)	
X = 0.95	*a* (Å)	3.2532(3)	3.2400(2)
	c (Å)	208.13(1)	5.2033(3)
	hh	2.6010(3)	2.6010(3)
	hc	2.6013(5)	--
	cc	2.6016(2)	--
	B_{eq} Ga/Zn	0.73(8)	
	B_{eq} N/O	1.0(9)	

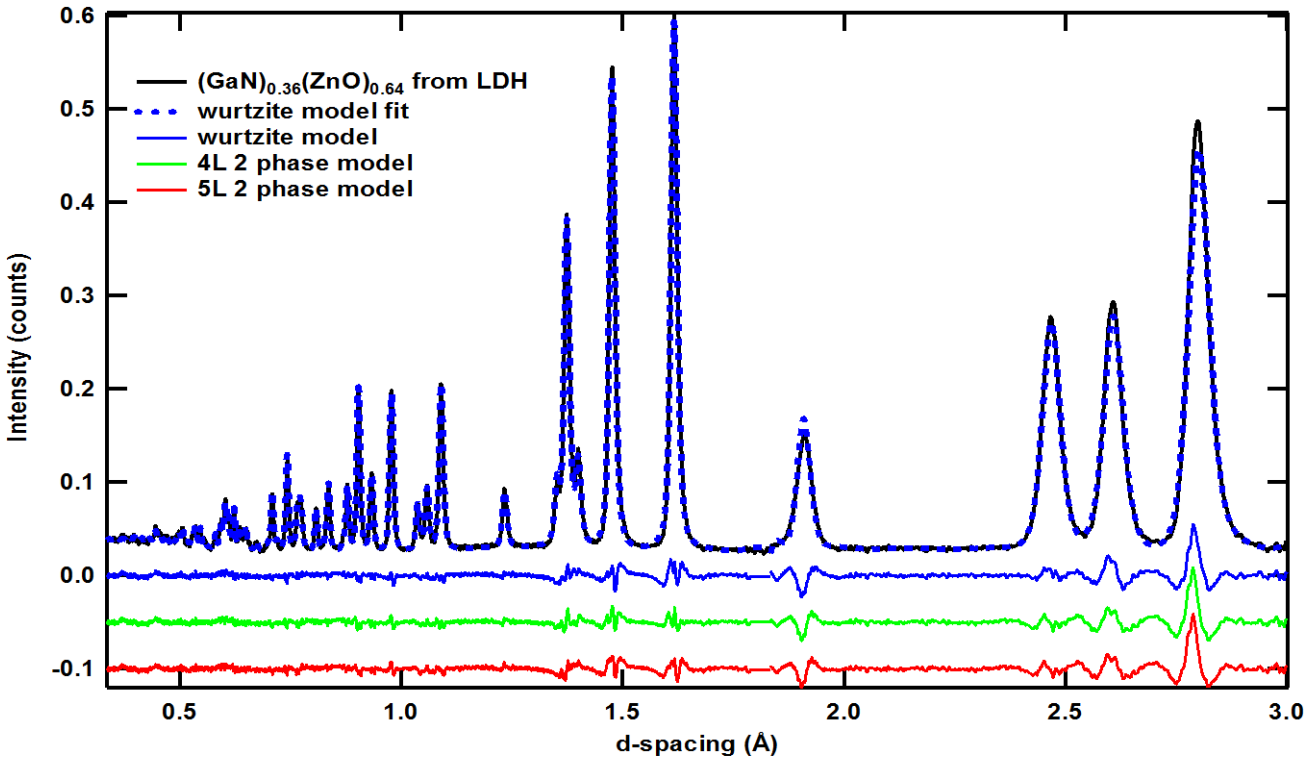

Figure 4.4. Neutron diffraction pattern of $(GaN)_{0.36}(ZnO)_{0.64,}$ synthesized from a LDH precursor, fit using a wurtzite, 4L, and 5L model showing improved fits using superstructure models.

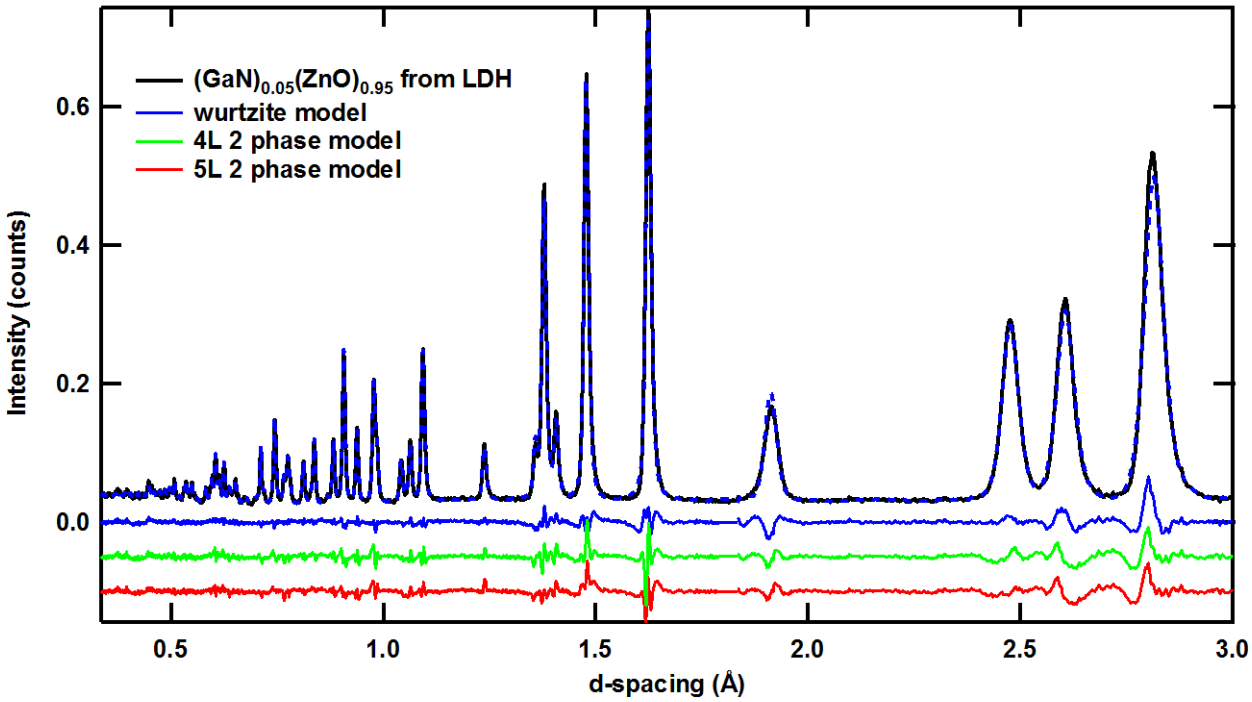

Figure 4.5. Neutron diffraction pattern of $(GaN)_{0.05}(ZnO)_{0.95}$ from LDH precursor showing failure of superstructure modeling to improve fit quality as compared to wurtzite hexagonal unit cell model.

4.3.3 Refinement comparisons $ZnGa_2O_4$ vs. LDH

Refined parameters for samples ranging from x = 0.60 – 0.95 and produced from an LDH precursor are shown in Table 4.8. We again see viable refined parameter values giving us confidence in this model type for gallium zinc oxynitrides synthesized in multiple manners. Overall it seems that samples with $x > 0.42$ contain a smaller amount of cubic intergrowth than is represented by a 4L double block superstructure regardless of precursor type. These samples therefore do not need a 3 phase refinement, but should be sufficiently modeled using a 2 phase refinement with an explicit superstructure and a separate hexagonal phase. Both precursors were used to synthesize $(GaN)_{1-x}(ZnO)_x$ samples in a similar manner, and details of the synthesis conditions for each sample are given in Table 4.9. For samples synthesized from a $ZnGa_2O_4$ precursor, intermediate grindings to promote homogeneity were implemented for higher zinc content samples and can be a reason for smaller values of cubic intergrowth in these two samples. In order to test this hypothesis, samples with lower zinc contents will need to be synthesized with intermediate grindings as well. This does not hold true for samples produced from a LDH precursor, as these were also higher zinc content samples that contained smaller amounts of cubic intergrowth according to our refinement results and were not subjected to intermediate grindings. It would be necessary to also have lower zinc content samples produced from a LDH precursor in order to draw direct comparisons to samples synthesized from a $ZnGa_2O_4$ precursor. Higher zinc content samples from $ZnGa_2O_4$ were attempted and are limited to approximately x = 0.65.

Table 4.9. Reaction conditions for $(GaN)_{1-x}(ZnO)_x$ $x = 0.10 – 0.95$ from $ZnGa_2O_4$ and LDH precursors.

$(GaN)_{1-x}(ZnO)_x$	precursor	Excess ZnO?	Reaction Temp (°C)	Reaction time (h)	Flow rate ml/min	Intermediate grindings (h)
x = 0.10	$ZnGa_2O_4$	No	850	23	5	--
x = 0.30	$ZnGa_2O_4$	No	850	17	5	--
x = 0.43	$ZnGa_2O_4$	Yes	850	42	5	22
x = 0.49	$ZnGa_2O_4$	Yes	850	42	5	22
x = 0.60	LDH	Yes	800	4.5/15	10	--
x = 0.64	LDH	Yes	800	0.5/10	10	--
x = 0.68	LDH	Yes	800	0.5/5	10	--
x = 0.81	LDH	Yes	800	0.5/5	10	--
x = 0.90	LDH	Yes	800	0.5/4	5	--
x = 0.95	LDH	Yes	800	0.5/5	10	--

4.4 Conclusion

We find that our superstructure modeling can be applied to a large range of $(GaN)_{1-x}(ZnO)_x$ samples synthesized from different precursor. The optimal 4L double cubic block superstructure continues to be the optimal model for all samples shown in this study, suggesting that cubic intergrowth width is uniform from sample to sample. We were able to make some direct comparisons of zinc content to cubic intergrowth, as it seems lower zinc content samples contain much higher amounts of intergrowth. We are encouraged that this method for quantifying cubic intergrowth amount is robust. A larger range of samples synthesized from an LDH precursor will be necessary for further analysis and careful synthesis condition stability is to be implemented. Transmission electron microscopy analysis of these samples should also shed light on the presence of intergrowths in these samples. It is important to note that samples synthesized from our $Ga_2O_3(ZnO)_{16}$ precursor discussed in Chapter 2 did not exhibit signs of intergrowth existence in either TEM or Rietveld studies.

Chapter 5

Local Structure Investigations of $(GaN)_{1-x}(ZnO)_x$

5.1 Introduction to local structure

The $(GaN)_{1-x}(ZnO)_x$ solid solution has gained much attention for its potential as a photocatalyst in visible light solar water splitting. Previous studies have provided an extensive analysis of this compound's average structure, including defects such as cation vacancies and cubic intergrowths, as found through compositional and structural techniques. The local structure of this solid solution however has yet to be discussed further. Crystallographic studies in general require a periodic lattice and complex materials often have small deviations from perfect periodicity. These deviations can have a large effect on the material's properties and are important for understanding a structure in its entirety.[45] Local structural probes such as x-ray absorption fine structure (XAFS) and nuclear magnetic resonance (NMR) offer local structural information but only in a very short range. Imaging such as transmission electron microscopy (TEM) can be a complementary tool for these short range local probes, but does not offer average information with high accuracy, since changes can occur from particle to particle.

More specifically, solid state NMR provides a local probe for specific atoms and their structural environment in solid materials. An atom in a particular coordination bonding to specific ligand atoms will provide a chemical shift relative to a chosen standard. For example, a Ga atom bound to four N atoms will provide a chemical shift of 330 ppm in a hexagonal structure, while in a cubic structural formation will provide a chemical shift of 357.5 ppm.[110] In addition, if that same Ga cation were not bound to N atoms exclusively a chemical shift with a differing value would appear. This type of analysis therefore allows for not only coordination number to be determined, but also ligand atom types to be determined. While this type of analysis can provide a clear picture of specific atomic

environments, quantification of these differences in local environment is difficult, and calculations of specific information such as deviations in bond lengths must be found using other techniques.

Common crystallographic analysis includes X-ray or neutron diffraction techniques which take into account Bragg peaks only. Often deviations in atomic positions can be described as lattice defects when these deviations are few and far between. Bragg's law allows for an extremely large number of atoms and their positions to be described through translational symmetry of a much smaller unit cell. Through diffraction measurements the lattice coherence length of an atom is measured not the actual lattice constant, and there exist uncertainties in this value which can be as small as 10^{-5}Å.[45] This is a nanoscale value which is not probed through classic diffraction methods. If the amount of defects is high however they cannot be described as lattice defects. They are in fact deviations from the long range order of the material and cannot be analyzed with Bragg diffraction only. Pair distribution function analysis allows for diffuse scattering to also be analyzed. This technique was originally implemented for non-crystalline materials where there is no structural periodicity present.[45] It was later discovered that average crystalline materials can also have locally non-crystalline structures or locally differing structures from the average. Since this is really a nanoscale technique, the uncertainties that come from Bragg diffraction can be analyzed to reveal local deviations if present. In general, the pair distribution function analysis is a technique used for the investigation of short-range structure in amorphous and crystalline materials. High-resolution beamline instruments allow for facile data collection for these measurements and an instrument with Q > 30Å will provide data with minimal error.

Semiconductors such as GaN and ZnO have the same wurtzite structure but differing band gaps (3.4eV vs. 3.2eV respectively). As was discussed in Chapter 2, the band gap can be engineered by alloying these two wide band gap semiconductors to form a solid solution, $(GaN)_{1-x}(ZnO)_x$, with lattice values that changes approximately linearly with *x* as described by Vegard's law. Crystallographically,

when *x* is changed, the number of Ga-N and Zn-O bonds changes linearly, providing the average bond distances. Locally however, there may be differences in particular bond lengths as a function of x. In addition, there may be clustering of specific types of tetrahedra, as wurtzite GaN is a Ga cation tetrahedrally coordinated to four N anions. NMR studies will allow for variations of GaN_4 to be studied as Zn and O are also present in these oxynitrides and local clustering may be present. Specific probes to the nitrogen and gallium local environments allow for these specific studies. In addition, PDF studies will allow for nearest neighbor bond distances to be determined to show, if present, local deviations from average structural bond lengths.

In this study the local structure of a range of $(GaN)_{1-x}(ZnO)_x$ samples is investigated through ^{71}Ga and ^{14}N solid state NMR spectroscopy and neutron pair distribution function analysis. These methods provide complementary data to previously published TEM studies showing cubic intergrowths in average wurtzite structure samples. Bond valence sum analyses compliment PDF data analyses indicating changes in local bond lengths as a function of specific tetrahedral cluster type.

5.2 Experimental

5.2.1 Synthesis

$Ga_2O_3(ZnO)_m$ precursors were carried out by mixing stoichiometric amounts of Ga_2O_3 (Alfa Aesar, 99.999%) and ZnO (Alfa Aesar, 99.99%), grinding with an agate mortar and pestle, and placing the mixture in a dense alumina crucible (CoorsTek). The m = 16 phase used as a precursor for $(GaN)_{1-x}(ZnO)_x$ syntheses was obtained by reacting stoichiometric amounts of Ga_2O_3 and ZnO (1:16) in a sealed alumina tube held at 1350 °C (1623 K) under flowing oxygen (~60 ml / min) for a total of 144 h with intermediate grinding steps every 48 h to promote reactivity and product homogeneity.

$ZnGa_2O_4$ samples were obtained by reacting stoichiometric amounts of Ga_2O_3 and ZnO (1:1) in a box furnace held at 1000 °C (1273K) in air for a total of 24h with an intermediate grinding after 12 hr to promote reactivity and product homogeneity.

Conversion of the $Ga_2O_3(ZnO)_{16}$ precursor or the $ZnGa_2O_4$ precursor into a wurtzite oxynitride was typically done at 1123 K under NH_3 flow (5ml/min) for times of 10-18h, resulting in single phase wurtzite samples with varying zinc contents. After heating, the sample was cooled to room temperature under NH_3 flow and the tube was then purged with N_2 gas prior to sample removal. Higher zinc contents were synthesized with the aid of ZnO powder placed upstream from the sample boat during reactions to allow the vapor pressure of zinc to increase above the sample and settle into the sample.

GaN samples were obtained from the reaction of Ga metal (Alfa Aesar, 99.999%) in a large tube furnace under flowing NH_3. Ga metal was spread in an alumina boat to ensure maximum surface area, which was subsequently placed in a 3" diameter mullite tube for synthesis. The samples were ramped from room temperature to 700°C in flowing NH_3 (300 ml/min) and held for 30 min. Immediately following, the program was ramped to 1100°C and held for 2 hr. At its completion the furnace was allowed to cool. A light grey powder was produced.

5.2.2 Powder XRD

Progression of reactions was monitored using X-ray powder diffraction on a Bruker D8 Advance laboratory diffractometer (Cu K_α λ = 1.54059Å, 7-120° 2θ, 0.02 step size, 300 mm radius, 12 mm variable slits, 2.5º Soller slits and a 192-channel Lynx-Eye 1D position sensitive Si detector). Scans for phase identification were done at a rate of 0.1s/step (19.2 s/point) while Rietveld scans were collected using a scan rate of 3s/step (576 s/point). Zero background silicon slides were used as sample holders. The JADE software package (Materials Data, Inc.) was used for preliminary unit cell refinements and for phase identification. Rietveld refinements were carried using TOPAS v4.2 (Bruker AXS)

5.2.3 Diffuse reflectance spectroscopy

Optical properties of samples were measured using ultraviolet-visible diffuse reflectance spectroscopy (uv-vis DRS; PerkinElmer Lambda950). Powder samples were loaded into a cylindrical powder holder with a circular quartz window 16.60 mm in diameter and 1.50 mm thick. A scan range of 200 – 1000 nm (6.20 – 1.24 eV with a detector change at 860.80 nm and a lamp change at 319.20 nm) was used with a data interval of 1.30 nm and a scan rate of 182.25 nm/min and a $BaSO_4$ (Alfa Aesar, 99.998%) 100% reflectance standard.

5.2.4 Solid state NMR

^{14}N MAS NMR experiments were conducted on a Varian 11.7 Tesla spectrometer at 36.095 MHz resonance frequency and a sample rotation speed of 14 kHz on a 4mm probe. The spectra were acquired using a rotor synchronized echo pulse sequence ($\pi/2$ - τ_1 -π - τ_2- acq.), where $\tau = 1/\nu_r$ (spinning frequency), with a 5.5 μs $\pi/2$ pulse width and an acquisition delay of 10 s. All data were referenced to NH_4Cl at 0 ppm.

^{71}Ga MAS NMR experiments were conducted on a Varian 11.7 Tesla spectrometer at 152.42 MHz resonance frequency and a sample rotation speed of 14 kHz on a 4mm probe. The spectra were acquired using a rotor synchronized echo pulse sequence ($\pi/2$ - τ_1 -π - τ_2- acq.), where $\tau = 1/\nu_r$ (spinning frequency), with a 1.1 μs $\pi/2$ pulse width and an acquisition delay of 4 s. All data were referenced to gallium nitrate at 0 ppm.

5.2.5 Neutron pair distribution function

Neutron PDF experiments were conducted on two separate beamlines. Original experiments were conducted on NPDF at Los Alamos National Laboratory. The high-resolution total-scattering powder diffractometer is located 32 meters from the spallation neutron target and has 20 detector panels

with 160 position-sensitive detectors in the backscattering region of the instrument. With a *Q* range of 0.8 – 51.1Å and a Δd/d range of 0.15-0.70% depending on detector bank this beamline provides high-resolution and low background data. Data was collected at 15K and 300K and showed no difference from temperature dependence. Samples were packed in vanadium cans and were typically 2-3g. Data shown in this study are from 300K measurements.

Recent experiments were conducted on the NOMAD instrument at Oak Ridge National Laboratory. The high-resolution total-scattering powder diffractometer is located 19.5 meters from the moderator and has a wavelength range of 0.1 – 3Å. The instrument has 6 banks of detectors with an angular scattering range of 3 – 175°. With a Q range of up to 50Å and a δQ/Q of 0.8% this instrument provides high resolution data and is the fastest data acquisition measurement instrument for pair distribution function analysis. Samples were packed in 3mm quartz capillary tubes, were typically 50mg – 300mg in size, and were collected for 45 minutes at room temperature. Both neutron data sets were reduced using PDFgetN and all data was analyzed using PDFGui software.

5.3 Results and Discussion

5.3.1 Preliminary XRD studies

X-ray diffraction experiments using a Bruker D8 Advance laboratory diffractometer were conducted for phase analysis and cell refinements during syntheses on all samples. The work presented here encompasses $(GaN)_{1-x}(ZnO)_x$ semiconductor powders synthesized from both a $ZnGa_2O_4$ and a $Ga_2O_3(ZnO)_{16}$ precursor. All samples were shown to be single phase wurtzite $(GaN)_{1-x}(ZnO)_x$ unless otherwise indicated to have $ZnGa_2O_4$ impurities from unreacted starting material. The diffraction patterns for all samples measured for PDF studies are shown in Figure 5.1. For samples ranging in zinc content from $x = 0.10 – 0.65$ there is a clear shift in peak position to lower values of d-spacing with an increase in zinc. This relates well with past studies using a $Ga_2O_3(ZnO)_{16}$ precursor and is indicative of

an increase in lattice parameter as a function of zinc content. In addition, a GaN powder was synthesized via ammonolysis of Ga metal. XRD confirmed a wurtzite structure with sharp peaks, indicative of a highly crystalline homogenous sample. As a comparison, the XRD pattern of GaN from Alfa Aesar is included in Figure 5.2 showing broadening of peaks and clear impurities as compared to our synthesized sample. It is because of this that the as synthesized GaN sample was used for end member comparisons in this work.

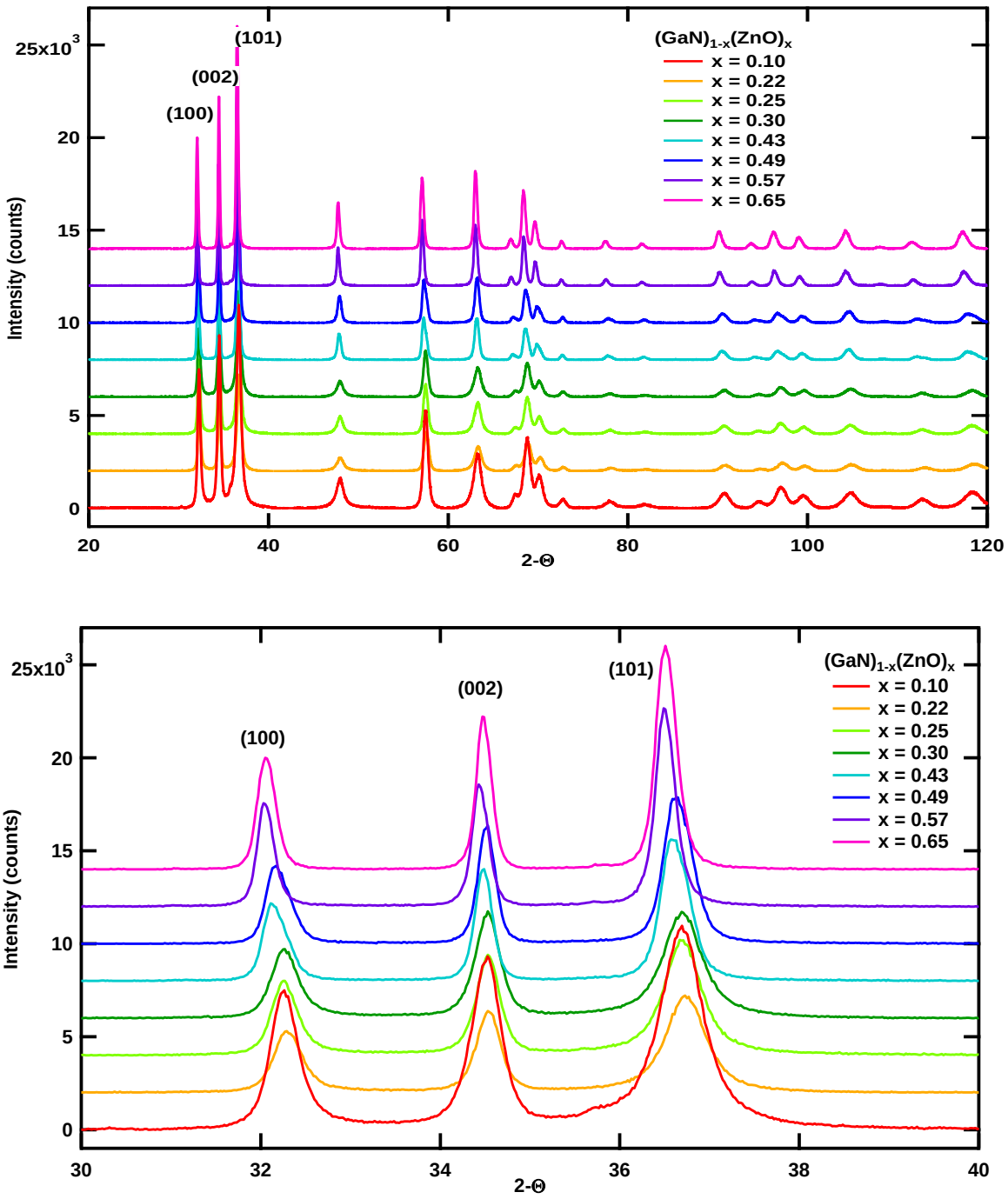

Figure 5.1. Powder x-ray diffraction pattern of $(GaN)_{1-x}(ZnO)_x$ samples of x_v = 0.10 - 0.65 (above). Below is a zoom of the three prominent wurtzite peaks with hkl's of (100), (002), and (101) respectively showing a clear shift in peak position to lower 2-θ with increase in lattice parameter (increase in zinc content).

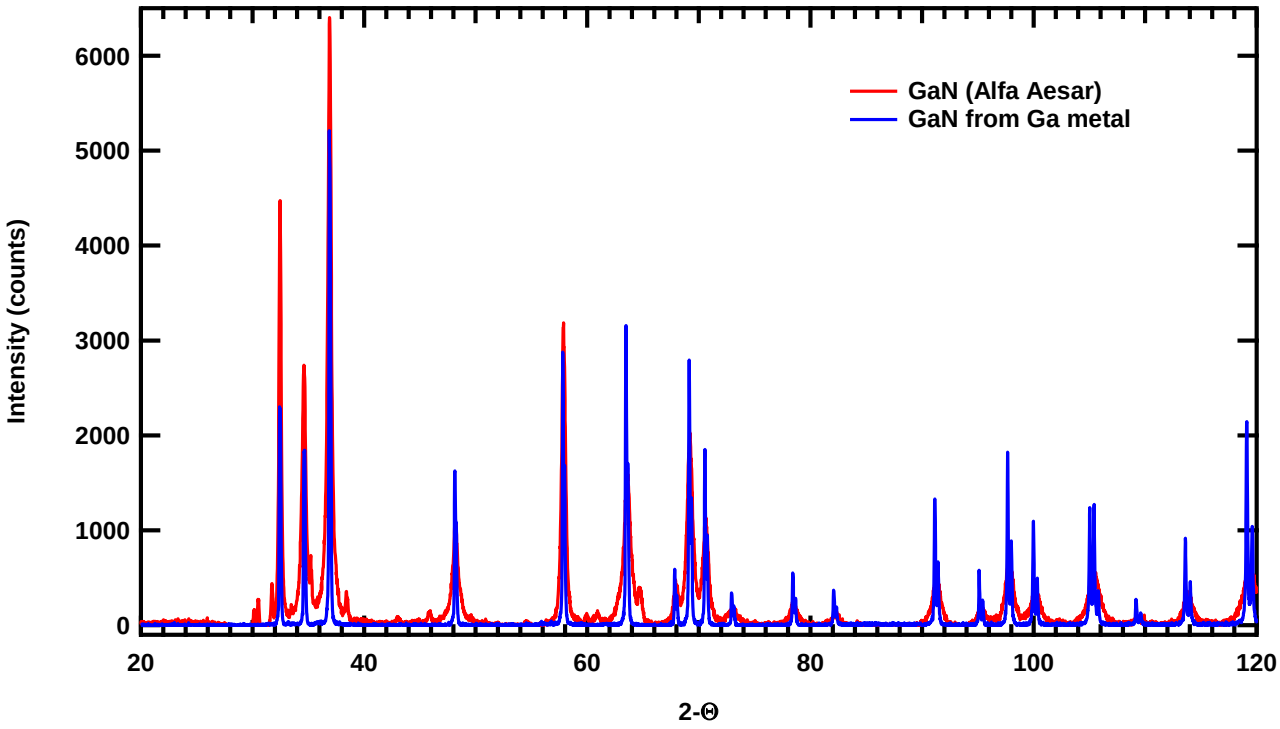

Figure 5.2. Powder x-ray diffraction pattern of GaN synthesized from Ga metal and GaN from bottle (Alfa Aesar 99%).

5.3.2 Optical studies of $(GaN)_{1-x}(ZnO)_x$ for band gap determination

As was discussed earlier, it has been reported that an increase in zinc content results in improved visible light absorption for $(GaN)_{1-x}(ZnO)_x$ samples with modest Zn contents ($x \leq 0.42$),[55,60] and this trend has more recently been seen in Zn-rich samples.[56,61] The optical properties of a range of $(GaN)_{1-x}(ZnO)_x$ samples prepared using a $ZnGa_2O_4$ precursor were determined by diffuse reflectance studies (Figure 5.3). The optical properties of $(GaN)_{1-x}(ZnO)_x$ samples prepared using a $Ga_2O_3(ZnO)_{16}$ precursor were discussed in detail in Chapter 2 and compare well to the data shown here. The relative absorbance (α_{KM}) obtained from a Kubelka-Munk transform of the reflectance data showed increasing visible light absorption with increasing Zn content ($x_v \leq 0.65$), and similar behavior was observed for the band gaps (E_g) calculated from quantitative fits to the functional form expected for direct band gap

absorption. Explanations of diffuse reflectance data curve fitting can be found in previous studies as described in Chapter 2.[99]

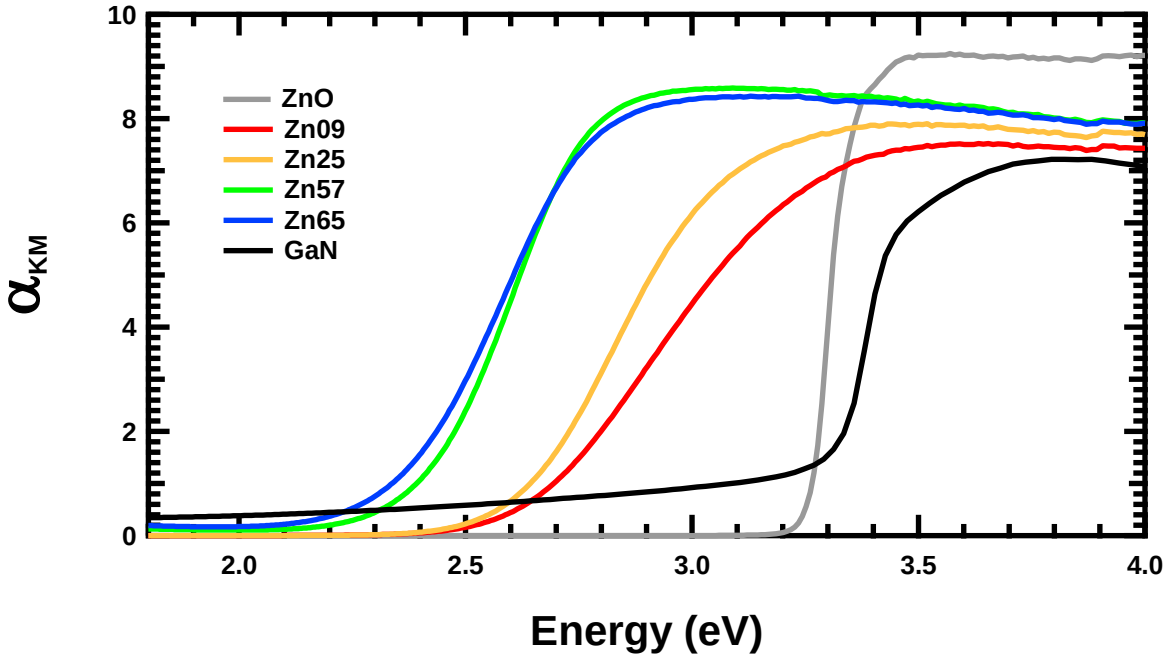

Figure 5.3. Diffuse reflectance data of $(GaN)_{1-x}(ZnO)_x$ samples for x_v up to 0.65 synthesized from a spinel $ZnGa_2O_4$ precursor. A shift to lower energy is observed with increasing Zn content.

Table 5.1. Band gaps of various $(GaN)_{1-x}(ZnO)_x$ samples synthesized from a $ZnGa_2O_4$ precursor by direct band edge fitting as was described in detail in Chapter 2.[99]

$(GaN)_{1-x}(ZnO)_x$	E_g (eV)
x = 0.09	2.98
x = 0.25	2.86
x = 0.57	2.60
x = 0.65	2.59

5.3.3 ^{14}N and ^{71}Ga NMR studies for nitrogen and gallium local environment

NMR has the ability to detect defects and impurities unable to be seen by methods such as X-ray and neutron powder diffraction. Solid state NMR provides us with the ability to probe element specific environments to understand the local structure around a certain atom. Both gallium (^{71}Ga, 39.89%, spin

3/2) and nitrogen (^{14}N, 99.63%, spin 1) have high-abundance quadrupolar nuclei applicable for solid-state NMR studies.[111] Changes in local environment such as defects or dopants should produce new peaks with differing chemical shifts. Knight shifts are specific peaks due to conduction electrons present in a sample.[111] Peak broadening can also occur and is generally attributed to dipolar couplings to other nuclei present in the sample or to the presence of defects. NMR capabilities were originally limited for solid nitrogen compounds to using a rare spin ½ isotope ^{15}N. With a natural abundance of 0.33% the use of this isotope requires expensive isotope enrichment for solid state NMR studies. However, with the use of high-resolution MAS NMR techniques ^{14}N experiments can be implemented.[112] Specifically, solid-state ^{14}N NMR studies allow characterization of the chemical environment of the nitrogen nucleus by the chemical shift and its anisotropy.

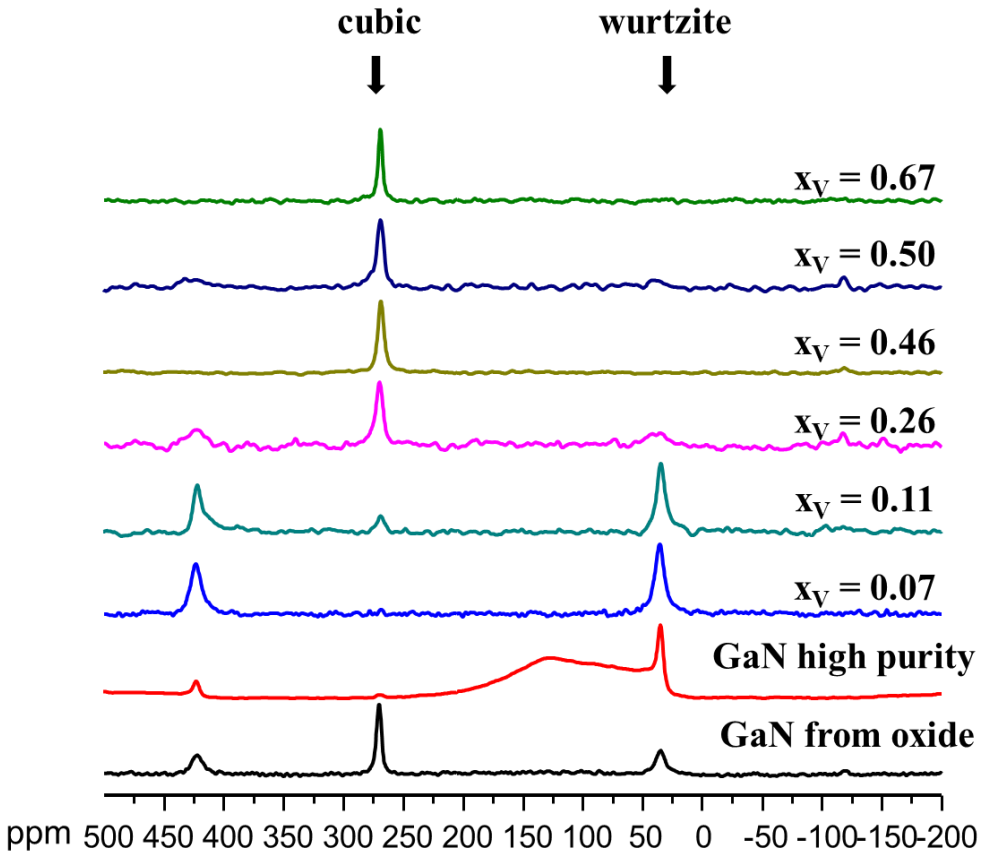

Figure 5.4. ^{14}N NMR at 500MHz depicting two different nitrogen environments. Introduction of a cubic environment is seen with an increase in zinc content in samples.

^{14}N NMR data was collected on a number of samples ranging from x_v = 0.07 to 0.67. Figure 5.4 shows two different chemical environments for nitrogen, a "wurtzite" = 40 ppm, and a putative "cubic" defect = 260 ppm. The 40 ppm resonance, while indicative of a wurtzite environment, shows slight line broadening as zinc content in the samples increase. This may be due to the cubic GaN environment forming, which has a similar chemical shift value. The 260 ppm resonance observed seems to be highly symmetric as it does not show spinning sidebands and is not affected by quadrupolar coupling or chemical shift anisotropy. Previous studies interpret similar data on wurtzite GaN samples in two different ways. One interpretation with identical peak positions as in this current study assigns the 52 ppm peak as a nitrogen environment with single bonds and the 287 ppm peak as nitrogen environments with double bonds.[44,113] While this study by Schwenzer *et al*. used similar synthesis conditions, it is important to note that enriched ammonia gas ($^{15}NH_3$) was used in their reactions and not in ours.

The second interpretation explains a hexagonal and a cubic GaN environment.[111] While the chemical shifts from this previous study are different, we can use them as a comparison since $Ga(NO_3)_3$ was used as a reference while our study used NH_4Cl. The two studies (ours and Yesinowski) are merely 200.0 ppm apart. This study found a shift value of 333.0 ppm as the value for hexagonal GaN that is not perturbed by defects or Knight shifts.[111] We believe that the slight line broadening observed in our patterns, as zinc content increases, is due to the formation of a cubic GaN environment which is consistent with previous studies using ^{14}N NMR.

^{71}Ga MAS NMR at 500MHz data was collected on a range of oxynitride samples including a comparison of an x = 0.50 sample from our 2:16 precursor, from the $ZnGa_2O_4$ precursor, and from a high-pressure synthesis by our collaborator William Woerner. Figure 5.5 shows the observed patterns for these samples along with an as prepared GaN from Ga metal and GaN from Alfa Aesar, used both for analysis and as the reference for chemical shift. There is a clear difference in peak shape for samples from our precursors versus that from a high-pressure synthesis route. Observable peak

broadening is seen for all samples except for the high pressure synthesis sample and our as prepared GaN. The sharp peaks for the high pressure sample and GaN from metallic Ga are indicative of high symmetry of the Ga sites on the atomic level.[44] Peaks were also observed at lower chemical shift values for samples of higher zinc content from our syntheses. Figure 5.6 shows faster spinning speed NMR data of these samples for the purpose of resolving these peaks further. Scans on our gallium containing starting materials (Figure 5.7) match well to the observed excess peaks and indicate two phase samples at $x_v > 0.46$.

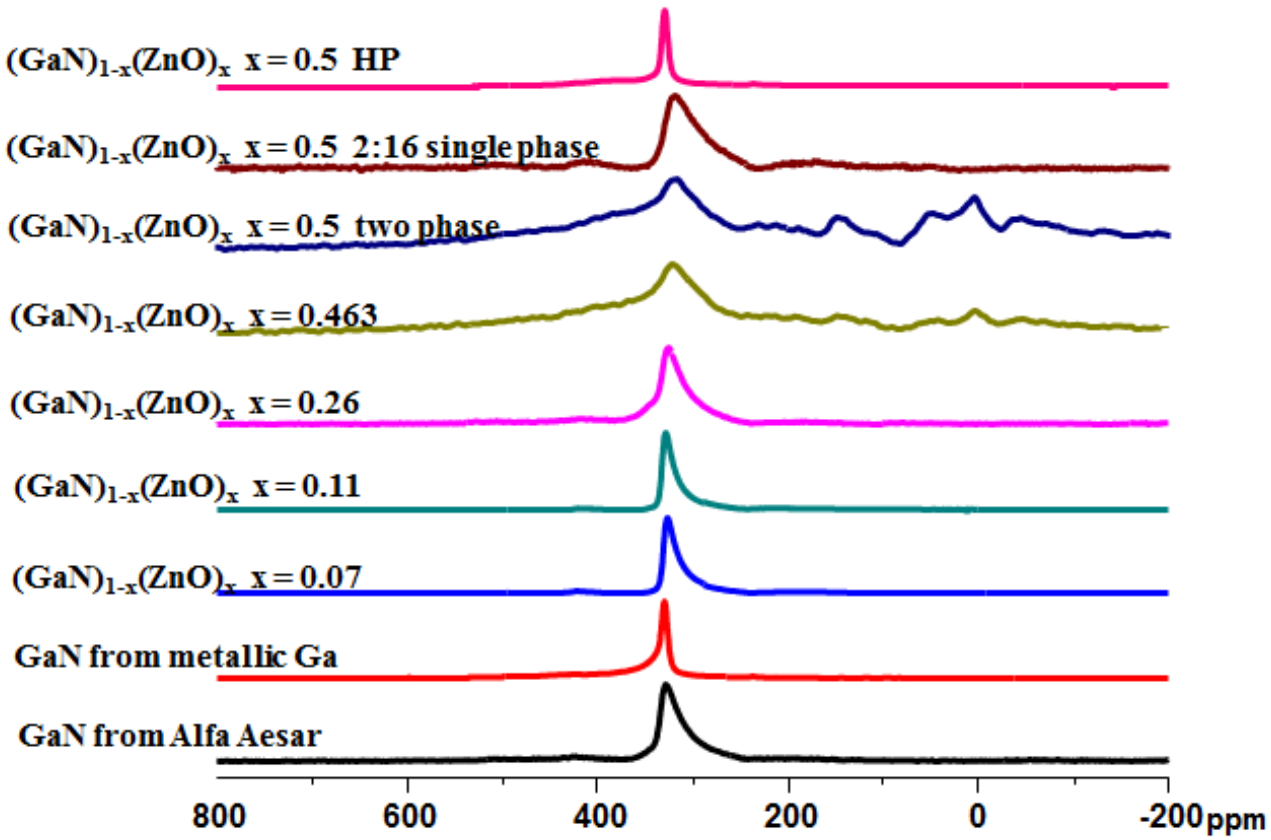

Figure 5.5. Spectra of ^{71}Ga MAS NMR at 500MHz of samples of $(GaN)_{1-x}(ZnO)_x$ $x_v = 0.07 – 0.50$.

Work by Yesinowski also shows an observable difference in chemical shift peak position for cubic and hexagonal GaN environments using ^{71}Ga NMR.[110] The observed chemical shifts are as follows: ^{71}Ga NMR at 900MHz hexagonal 301.8 ppm and cubic 297.0 ppm. Jung *et al*. observe

similarly small differences in peak positions for what they assign a hexagonal and cubic GaN environment. The study does not show a clear resolution of two separate peaks, but shows the start of the splitting of a peak.[114] A closer look at our samples in Figure 5.8 does not show two separate peaks as was reported in previous studies. However, we believe a broadening of the single peak is indicative of the formation of a cubic GaN environment. It is clear that this broadening is increased with increasing *x* value, which may correspond to larger amounts of cubic GaN present in the higher zinc samples.

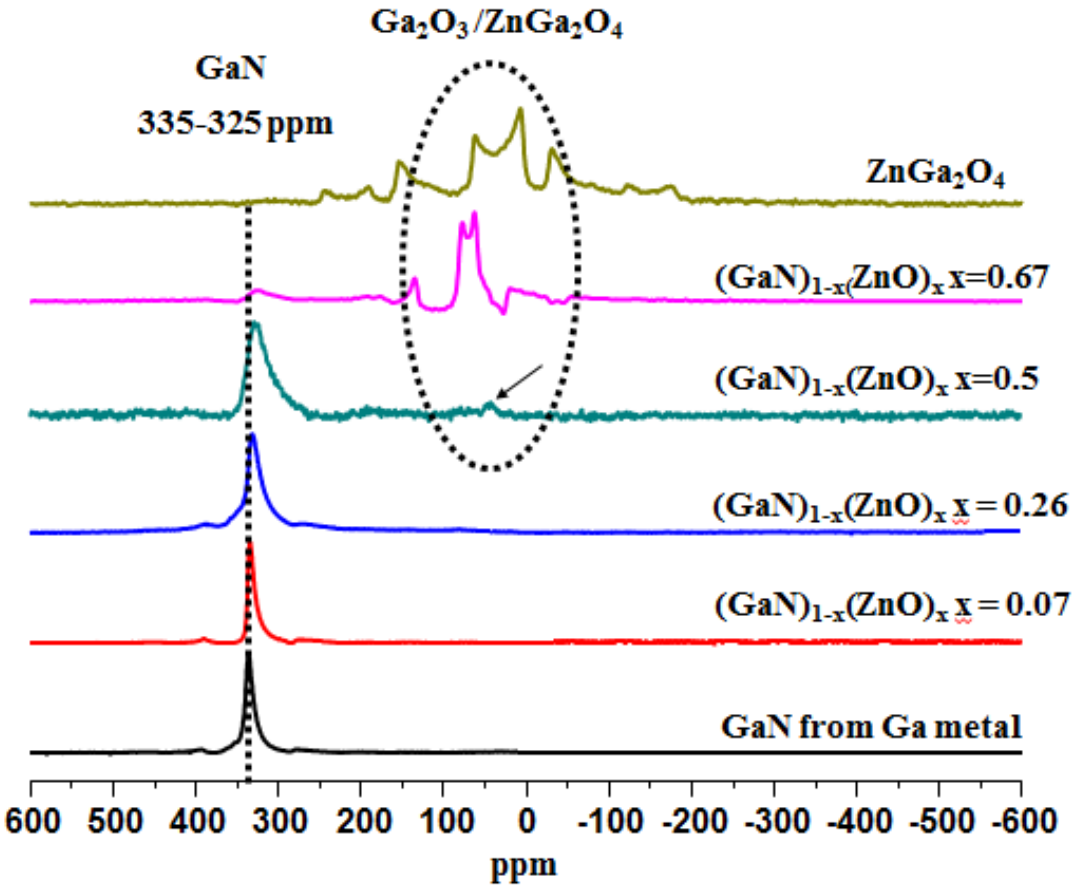

Figure 5.6. [71]Ga MAS NMR at 900MHz with δiso Ga(IV)= 200-220 ppm δiso Ga(VI)=40-50 ppm for pure gallium oxides.

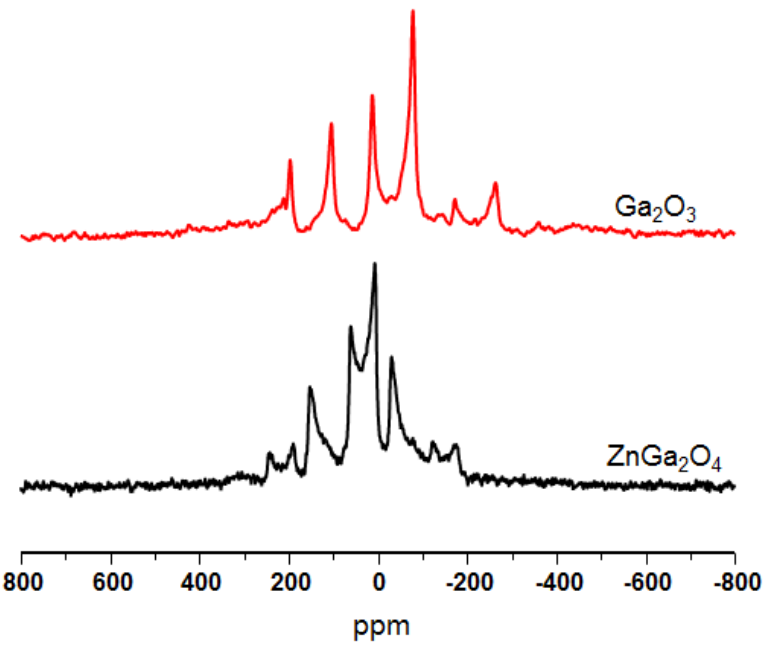

Figure 5.7. ^{71}Ga NMR at 900MHz of Ga_2O_3 and $ZnGa_2O_4$ gallium containing starting materials.

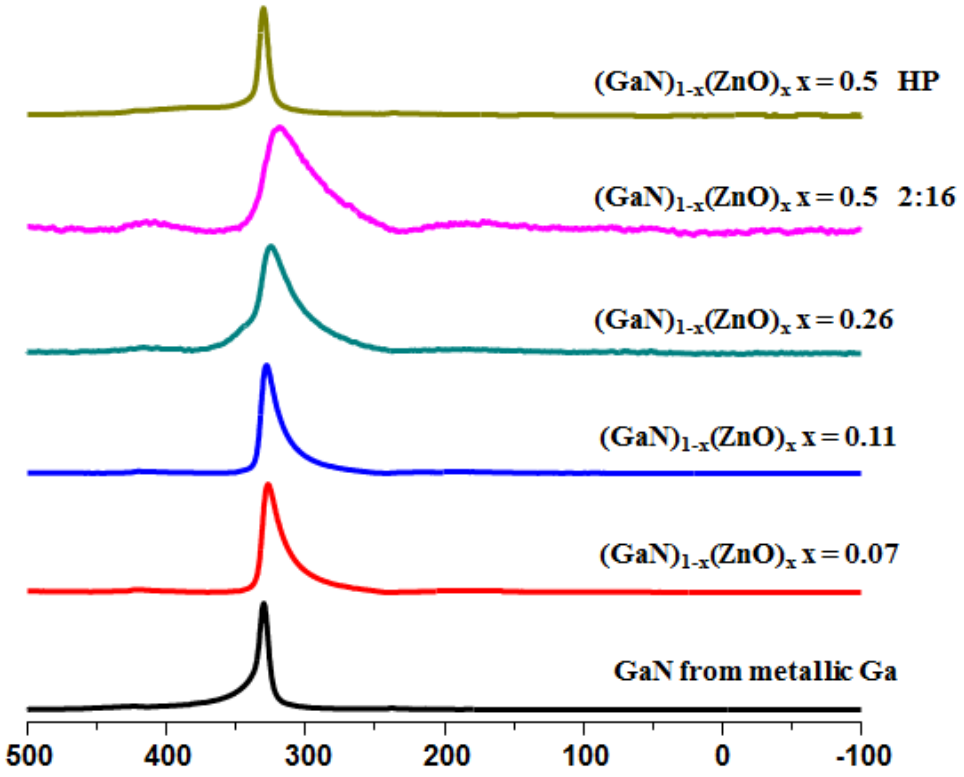

Figure 5.8. ^{71}Ga MAS 500MHz NMR. Broadening indicative of the formation of a cubic GaN component to certain samples.

Broadening of hexagonal GaN peaks can also be indicative of local clustering around the gallium atom. Figure 5.9 shows a closer look at the peak shape of a number of samples with varying zinc content and marks the expected hexagonal GaN peak along with the theoretically calculated peak shift for a Ga attached to four oxygen atoms instead of nitrogens. Since we have a solid solution of $(GaN)_{1-x}(ZnO)_x$ there are oxygen atoms present in the sample which may attach to gallium instead of zinc. Table 5.1 shows the calculated chemical shifts for Ga-N/O variations from collaborator Dr. Derek Middlemiss. We see a clear indication that most gallium atoms in our samples are bound to only nitrogens, or from the broadened component of these peaks, three nitrogen atoms and one oxygen atom for higher zinc content samples. This suggests that locally we have a clustering of GaN-like tetrahedra, however we would see a sharp peak if the site was completely symmetric meaning Ga attached to 4 tetrahedrally coordinated nitrogens.[44] Previous studies on GaN samples suggest that this broadening downfield from the expected 330 ppm hexagonal GaN chemical shift is due to a decreasing coordination number for Ga, or nitrogen deficiency.[44, 113,114] However, with this solid solution we expect not a nitrogen deficiency, but an introduction of non-symmetric GaN clusters. Overall, if the Yesinowski work suggests a separate peak position that is only merely a few ppm away from the hexagonal chemical shift for a cubic shift, we can conclude that both our ^{14}N and ^{71}Ga NMR data suggest small amounts of cubic GaN environments in some of these $(GaN)_{1-x}(ZnO)_x$ samples. Clustering of GaN_4 and GaN_3O allow for pair distribution function analysis to be interpreted as such for specific Ga-N and Ga-O distances and will be discussed in the next section.

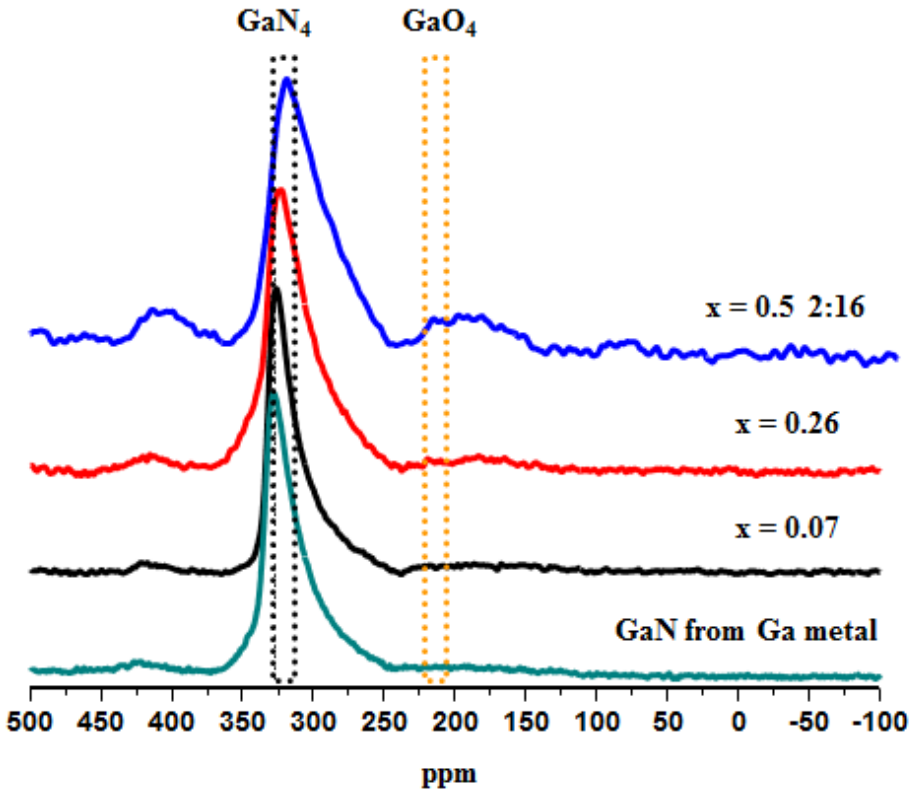

Figure 5.9. Local clustering of chemical shifts shown in ^{71}Ga MAS NMR 360MHz spectra.

Table 5.2. Theoretical chemical shifts for tetrahedra of Ga cations and oxygen/nitrogen anions.

Species	Calculated chemical shift
GaO_4	208 ppm
$GaNO_3$	212 ppm
GaN_2O_2	261 ppm
GaN_3O	309 & 305 ppm
GaN_4	322ppm

5.3.4 Bond valence sum analysis of $(GaN)_{1-x}(ZnO)_x$

Due to the insights into local clustering of specific bond types found in our NMR experiments, bond valence sum analyses were conducted in order to calculate what specific cluster-type bond lengths would be for the $(GaN)_{1-x}(ZnO)_x$ system. Bond valence has been found to be an excellent approximation for bond lengths in a crystal structure allowing for initial insights into local bonding to be

made and later on compared to experimental PDF data. According to Brese and O'Keeffe, the bond valence is defined as the sum of all valences from a given atom *i* with valence v_i according $v_i = \sum s_{ij}$, where v_i is the oxidation state of atom *i* and S_{ij} is the valence of the bond between atoms *i* and *j*.

The variation in length of a bond, or d_{ij}, with valence is described as follows,

$$v_{ij} = \exp[(R_{ij} - d_{ij})/b] \quad (5.1)$$

where *b* is a universal constant that shows the variation in length of a bond with valence and is equal to 0.37Å and R_{ij} is known as the bond valence parameter.[115] If there are *n* equivalent bonds around a central atom with valence *m*, then the valence of each bond is equal to $s_{ij} = m/n$. If the central atom is bound only to atoms of the same kind the valence equation is as follows, $R_{ij} = b\ln [v_i/\sum j\exp(-d_{ij}/b)]$. To predict bond distances independent of coordination number, the actual distance, $d_{ij} = R_{ij} - b(\ln(S_{ij}))$ where R_{ij} is the Brese and O'Keeffe empirical bond distance is used. From this we get $S_{ij} = \exp [(R_{ij} - d_{ij})/b]$ or the (Brese and O'Keeffe – experimental)/b to find S_{ij} then finally solve for d. As an example, the Brese and O'Keeffe bond valence value (R_0) for Zn^{2+} bound to an oxygen atom is equal to 1.704Å. With an S_{ij} of 2/4, or 0.5, we simply enter in all values and are able to solve for *d,* giving us a bond length value of 1.9605Å for Zn^{2+} bound to 4 oxygens. In general it was discovered that if you have an oxide and would like to know the distance of the corresponding nitride the following relation is used, $R_{iN} = -0.027 + 1.090R_{iO}$Å.[115] In this system we do not need to use this relation because we want to look at Ga-O and Zn-O as well as Ga-N and Zn-N.

The above explained calculations were implemented using the published R_{ij} values for the $(GaN)_{1-x}(ZnO)_x$ system in order to quantify differences between cluster types ranging from GaN_4 to ZnO_4. The calculated predicted bond lengths can be found in Table 5.3. What is found is a clear increase in bond length parameter with an increase in Zn-N type local bonding along with a decrease in bond length parameter with an increase in Ga-O type local bonding. Knowing the relative bond

distances for the range of bond length cluster types in this system will allow for experimental bond lengths found from PDF analysis to be compared and validated.

Table 5.3. Predicted bond lengths for GaN, ZnN, GaO, ZnO, and their alloys showing differences in bond length according to cluster type by bond valence sum analysis.

	$M\text{-}N_4$	$M\text{-}N_3O$	$M\text{-}N_2O_2$	$M\text{-}NO_3$	$M\text{-}O_4$
Ga	**1.951**	1.919	1.887	1.855	1.823
$(Ga_{3/4}Zn_{1/4})$	1.983	**1.951**	1.919	1.888	1.856
$(Ga_{2/4}Zn_{2/4})$	2.018	1.987	**1.955**	1.923	1.891
$(Ga_{1/4}Zn_{3/4})$	2.057	2.026	1.994	**1.962**	1.930
Zn	2.101	2.069	2.037	2.005	**1.973**

GaN **GaO**

ZnN **ZnO**

5.3.5 Pair distribution function analysis of $(GaN)_{1-x}(ZnO)_x$

Neutron pair distribution function studies were conducted on $(GaN)_{1-x}(ZnO)_x$ samples ranging from $x \sim 0.09 - 0.67$. As was discussed briefly earlier, pair distribution function analysis takes into account both the periodic and aperiodic structure of a complex material by measuring both the Bragg and diffuse diffraction during an experiment.[116] From our NMR studies it is clear that there are some local variations in chemical environment in our samples, and PDF studies should provide the data necessary for resolving differences in bond length locally. We would expect to see small changes as NMR suggests some clustering of gallium with nitrogen and oxygen bonds. In general, diffraction data is described as the diffracted intensity as a function of the momentum transfer of the scattering particle, or Q (also known as the diffraction vector). The diffraction vector, $Q = 4\pi\sin\theta/\lambda$. As Q is included in the definition of $\rho(r)$, or the atomic pair density function described in Chapter 1, it is clear that this function represents the real space structure of a material. The reciprocal space equivalent of this

function is the S(Q) or the total scattering function as it includes both Bragg and diffuse scattering.[45,117,116] A numerical Fourier transform of the measured intensity S(Q) allows for the study of the PDF, or G(r). The atomic PDF, or G(r), is equal to

$$G(r) = 4\pi r\rho_o(g(r) - 1) = \frac{2}{\pi}\int_0^\infty Q[S(Q) - 1]\sin(Qr)dQ \quad (5.2)$$

where ρ_o is the average atomic number density, g(r) is the atomic pair density, and r is a radial distance.[116,45] This function is measurable through experiments using X-ray and neutron powder diffraction methods and reflects both the long-range atomic structure and the local structural differences.

In real materials, forces between atoms result in their motion being correlated. These interatomic forces depend on atomic pair distances, and are therefore very strong for nearest-neighbor interactions. These interatomic forces decrease, or get weaker, as the atomic pair distances increase.[118] This is clearly shown in PDF patterns of our materials, as the nearest-neighbor peaks are sharper than those out to higher values of *r* (Å). Broadening of peak widths in general come from either thermal motion or internal strain, due to bond length mismatch. Bond length mismatch is common in semiconductor alloys and is likely to play a role in peak broadening of samples measured from the $(GaN)_{1-x}(ZnO)_x$ solid solution system. In earlier PDF studies efforts were made to fit the $Ga_{1-x}Al_xAs$ semiconductor alloy system using PDF analysis by taking into account bond-stretching and bond-bending forces. However, this model fails in being able to resolve specific peak types past the nearest-neighbor peak and would not be suitable for this study.[119,117] Studies of the zinc-blende structured $ZnSe_{1-x}Te_x$ alloys showed clear changes in local structure with an increase in x with differences in the nearest-neighbor peak in their PDF pattern fits. With an increase in *x* a decrease in ZnTe peak height occurred along with a subsequent increase in SeTe peak height. This indicates that pure Zn-Te and Se-Te bonds are present as a function of composition and that clustering is most likely not present. Peaks at higher *r* ranges did not show this disappearance and appearance of peaks depending on composition, but instead showed broadening of peaks due to intermediate compositions which is indicative of interatomic

strain in alloys.[117,120] We would expect the same sort of behavior in our $(GaN)_{1-x}(ZnO)_x$ samples at longer distances due to their solid solution nature, however, as indicated from our NMR studies we are certain there is local clustering of non-uniform GaN and ZnO tetrahedra suggesting that an appearance/disappearance of specific bond length peaks may not be present with changes in composition.

Initial data collection was conducted on 2.5-3g samples packed in vanadium cans using beamline NPDF at Los Alamos National Laboratory. Figure 5.10 shows the F(Q) vs. Q, or the reduced structure function where F(Q) = Q[S(Q) – 1], of $(GaN)_{1-x}(ZnO)_x$ from $x = 0.09 – 0.65$. This reduced structure function is used to highlight intensities at high Q that may be overshadowed by instrumental or background effects. Samples measured were synthesized from a $ZnGa_2O_4$ precursor, and show considerable differences at high Q as compared to end members ZnO and GaN. As the S(Q) is a measure of the total diffraction we can attribute the lack of high Q peaks for all solid solution members to a presence of short-range disorder. Peaks are present for ZnO and GaN end members out to much higher *r* ranges than for those of solid solution members. This would generally be attributed to the higher level of crystallinity of the end members as compared to $(GaN)_{1-x}(ZnO)_x$ samples, but in this system broader peaks are more likely to be due to the distribution of many different bonds lengths and/or lattice parameters for a particular peak. In order to investigate these deviations from ZnO and GaN end members further, an analysis of the Fourier transform of the S(Q), or the G(r), must be implemented.

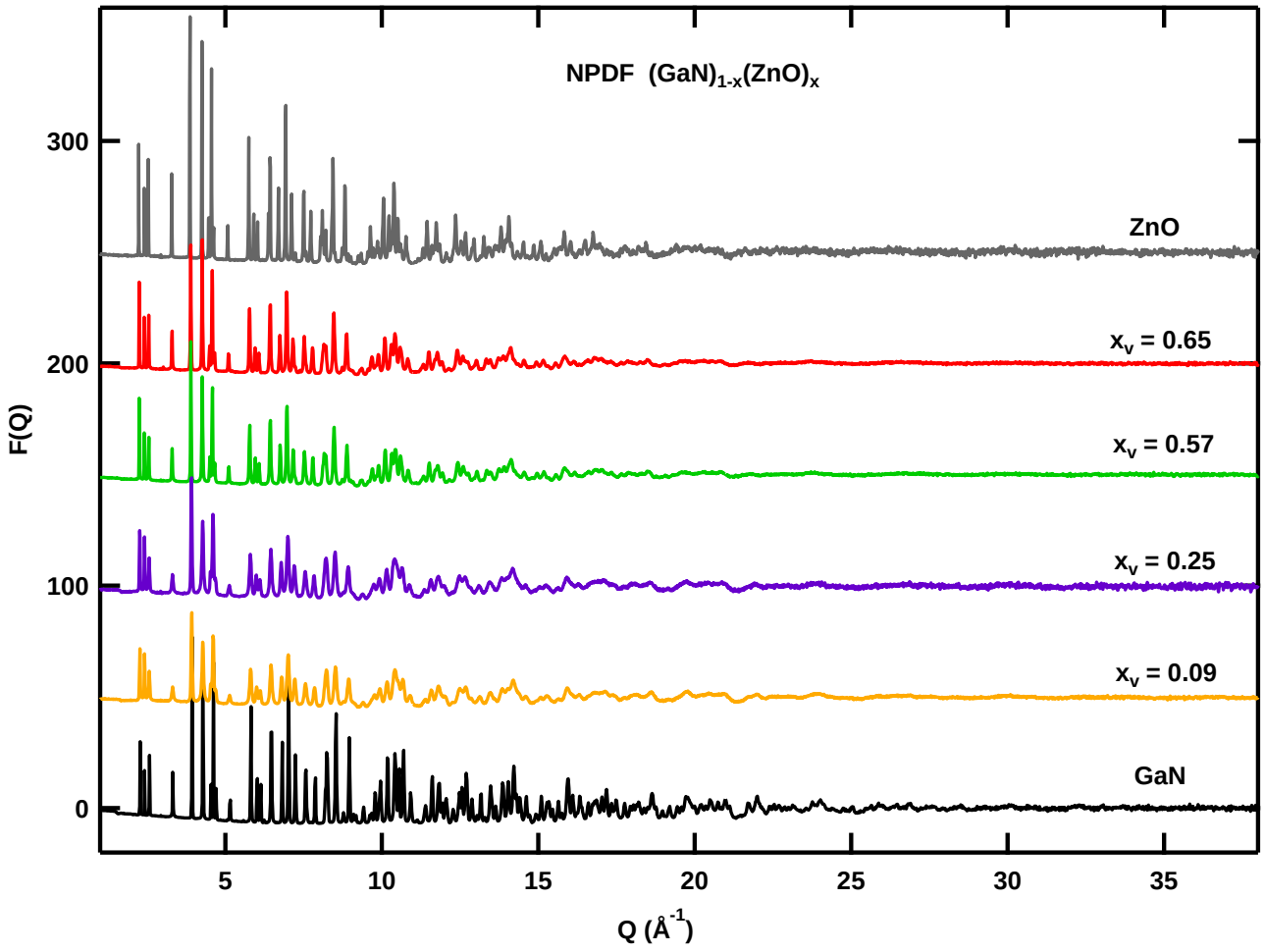

Figure 5.10. Total scattering data (normalized to F(Q) = Q[S(Q)-1]), F(Q) vs. Q, collected on NPDF, LANL at 300K showing higher crystallinity of end members indicative of local disorder among solid solution members.

Data was fit using three different model types in order to find the best fit locally to our data; an average wurtzite unit cell, a 1 tetrahedra model representing a wurtzite asymmetric unit, and a 2 tetrahedra model with separate ZnO and GaN phases. As has already been discussed in detail in Chapter 3, an average wurtzite unit cell with shared occupancies fixed according to Zn/Ga composition for the Ga/Zn cations and N/O anions separately was implemented along with anisotropic displacement parameters. The 1 tetrahedra model consisted of half of the atomic positions of a full wurtzite unit cell and showed comparable fit parameters. Finally, a two tetrahedra model implemented separate GaN and

ZnO phases with individual scale factors fixed to be equal to the ZnO or GaN composition according to the chemical formula $(GaN)_{1-x}(ZnO)_x$. The overall scale factor was therefore allowed to refine along with anisotropic displacement parameters, lattice parameters, and the cation z positions, which are not defined as special positions. Both the average wurtzite and 1 tetrahedra models showed very similar parameters overall, and a bond length distribution analysis confirmed these similarities and will be discussed later on. In all samples δ1 was allowed to refine, accounting for correlated motion and the contribution of 1/r to peak sharpening. δ2 describes low temperature behavior and was not used in refinements. The overall peak width in PDF data is described as follows where the last terms model broadening as a result of the Q resolution of the diffractometer,[121]

$$\sigma_{ij} = \sigma'_{ij}\sqrt{1 - \frac{\delta_1}{r_{ij}} - \frac{\delta_2}{r_{ij}^2} + Q_{broad}^2\, r_{ij}^2} \tag{5.3}$$

The pair distribution function, or G(*r*), data for samples measured at NPDF, and fit to an average wurtzite model type, are shown in Figure 5.11 out to 10Å in *r*. Fits using all three model types were completed and showed only very small variations in goodness of fit, or R_w, as can be seen in Table 5.3. R_w is the function used to measure the agreement of the calculated PDF from the model to the experimental data,[122]

$$R_w = \sqrt{\frac{\sum_{i=1}^{N} w(r_i)[G_{obs}(r_i) - G_{calc}(r_i)]^2}{\sum_{i=1}^{N} w(r_i) G_{obs}^2(r_i)}} \tag{5.4}$$

In all three model types the nearest-neighbor peak is not properly modeled, however, distances from 5Å to higher *r* show very good fit to the data. This is not surprising, as average structural techniques such as XRD have shown that the data fits well to an average wurtzite unit cell, except in cases where intergrowths are present causing peak intensity issues. Figure 5.12 shows a good average model fit out to higher r ranges and reiterates the conclusion that there is indeed local disorder which varies from the average wurtzite structure. An identical analysis was implemented using newly acquired data from NOMAD at Oak Ridge National Laboratory. Samples to fill in gaps of our x value range of

this solid solution were analyzed and are equally comparable to NPDF data. The total scattering data, PDF analysis, and refinement parameters from samples measured on NOMAD can be found in Figures 5.13, 5.14, and Table 5.5.

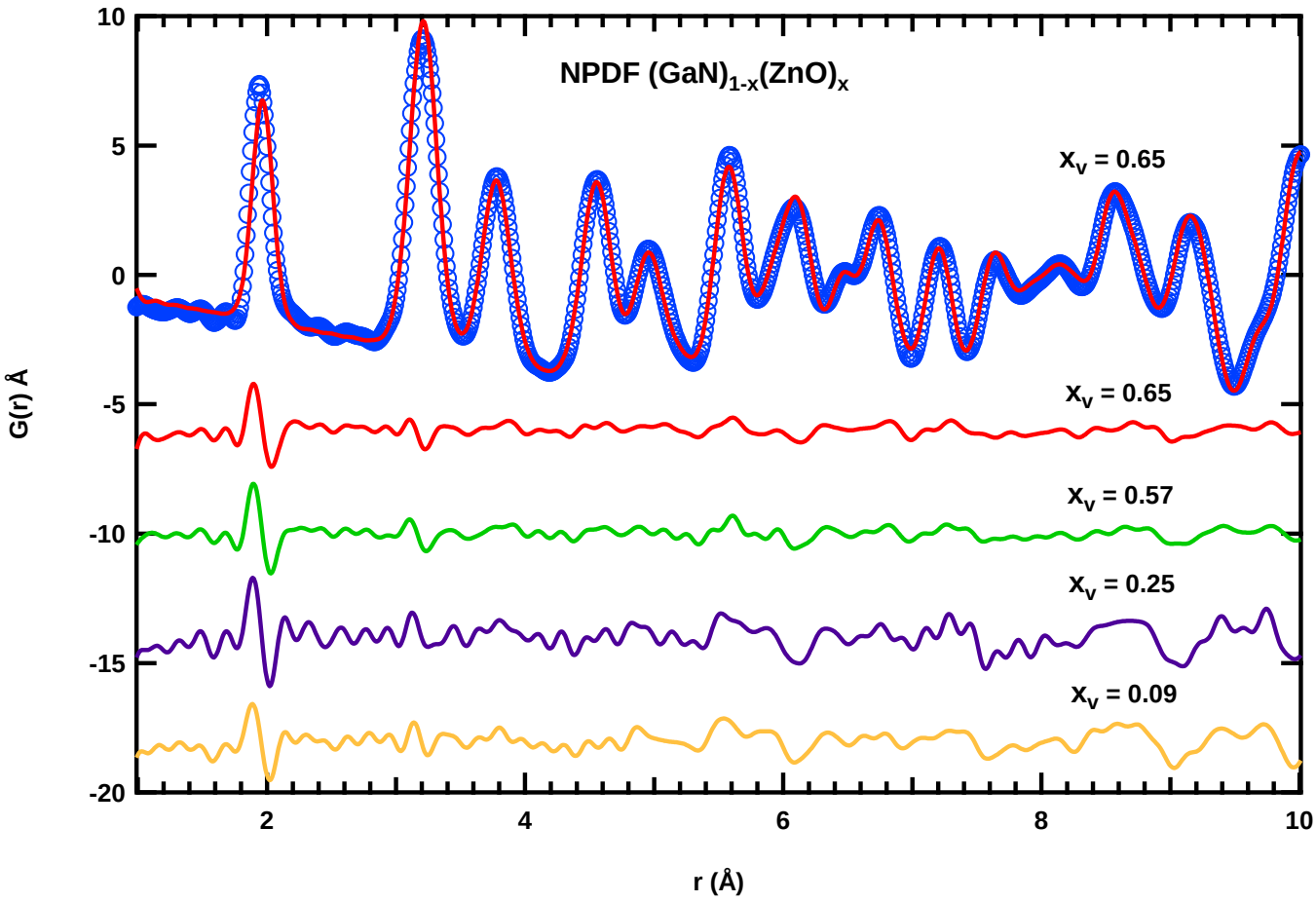

Figure 5.11. Fit to x_v = 0.65 and difference patterns for all samples measured at NPDF at 300K out to 10A using standard wurtzite model.

Table 5.4. Lattice parameters, *z* positions, and occupancies of samples measured on NPDF and refined using a wurtzite model from 1.0 – 10Å in PDFGui. Lattice parameters were allowed to refine as well as one *z* position, to conserve symmetry the next *z* position was constrained to equal the first + ½ as is according to symmetry. Occupancies were fixed to conserve the composition of the solid solution.

NPDF	x = 0.65	x = 0.57	x = 0.25	x = 0.09
a (Å)	3.228(5)	3.223(9)	3.206(8)	3.201(3)
c (Å)	5.20(1)	5.20(2)	5.20(2)	5.193(9)
z_1 Ga/Zn	0.379(3)	0.383(6)	0.377(5)	0.378(2)
Ga/N occ	0.35	0.43	0.75	0.91
Zn/O occ	0.65	0.57	0.25	0.09

Table 5.5. Refinement parameters from fits to NPDF data of $(GaN)_{1-x}(ZnO)_x$ samples from x = 0.09-0.65) using PDFGui software and three different model types.[121]

Model	Sample	$U_{11} = U_{22}$ Ga/Zn (Å^2)	U_{33} Ga/Zn (Å^2)	$U_{11} = U_{22}$ N/O (Å^2)	U_{33} N/O (Å^2)	R_w
wurtzite	x = 0.09	0.00429	0.00406	0.00509	0.00506	0.148
	x = 0.25	0.00440	0.00411	0.00641	0.00612	0.165
	x = 0.57	0.00576	0.00554	0.00658	0.00635	0.126
	x = 0.65	0.00607	0.00597	0.00687	0.00668	0.119
1 ideal tetrahedon	x = 0.09	0.00417	0.00410	0.00529	0.00521	0.154
	x = 0.25	0.00447	0.00431	0.00631	0.00628	0.175
	x = 0.57	0.00567	0.00559	0.00635	0.00630	0.135
	x = 0.65	0.00600	0.00592	0.00672	0.00675	0.126
2 ideal tetrahedra	x = 0.09	0.00412	0.00392	0.00512	0.00510	0.113
	x = 0.25	0.00417	0.00410	0.00648	0.00640	0.119
	x = 0.57	0.00569	0.00572	0.00689	0.00653	0.119
	x = 0.65	0.00600	0.00599	0.00707	0.00697	0.110

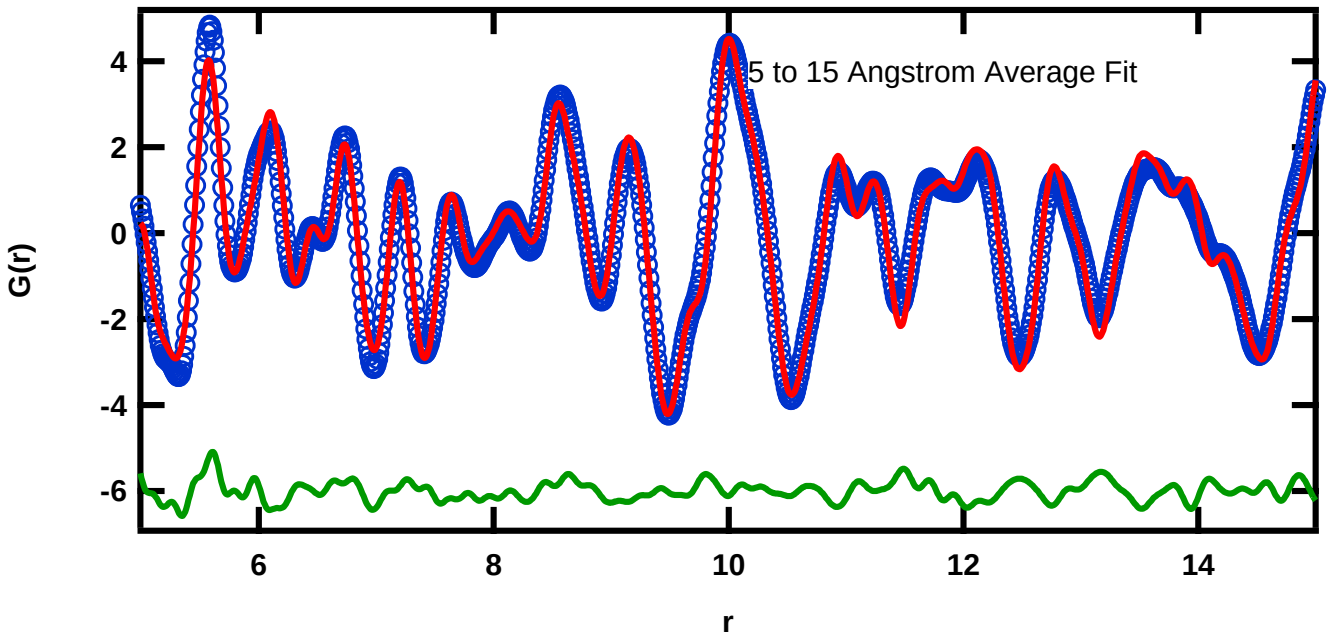

Figure 5.12. Average wurtzite structural fit to extended r range (> 5Å) showing good fit of the average structure at longer range on $(GaN)_{1-x}(ZnO)_x$ x = 0.25 sample from NPDF. All samples behaved in the same manner at higher *r* values and fit well to the average wurtzite structure.

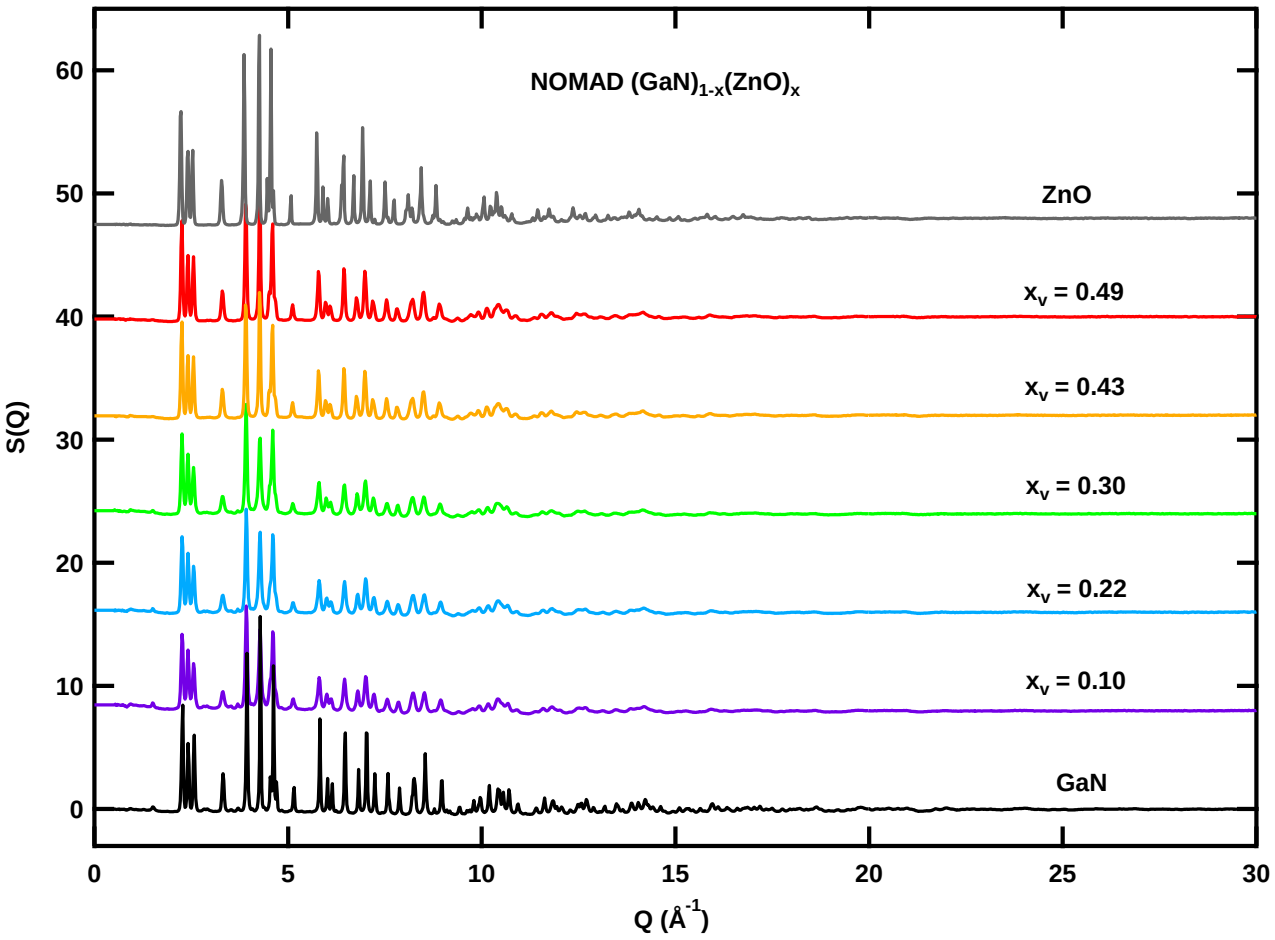

Figure 5.13. S(Q) vs Q, or total scattering pattern of samples measured at NOMAD, SNS showing comparable crystallinity to NPDF samples.

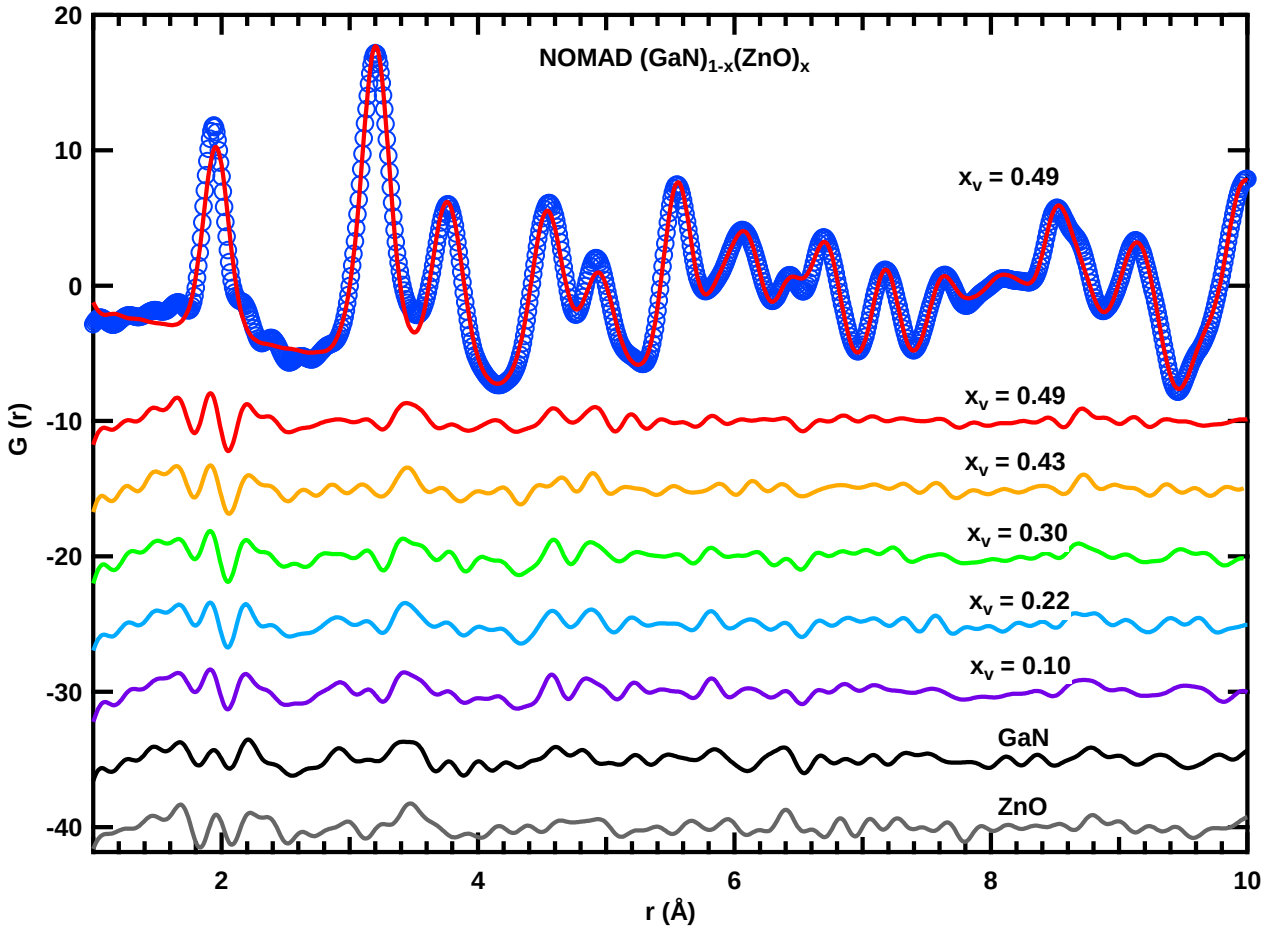

Figure 5.14. Fit to x_v = 0.49 and difference patterns for all samples measured at NOMAD out to 10 Å using standard wurtzite model and showing inability to model nearest-neighbor peak with average structural model.

Table 5.6. Lattice parameters, *z* positions, and occupancies of samples measured on NOMAD and refined using a wurtzite model from 1.0 – 10 Å in PDFGui. Lattice parameters were allowed to refine as well as one z position, to conserve symmetry the next z position was constrained to equal the first + ½ as described by symmetry. Occupancies were fixed to conserve the composition of the solid solution.

NOMAD	x = 0.49	x = 0.43	x = 0.30	x = 0.22	x = 0.10
a (Å)	3.213(8)	3.212(8)	3.209(9)	3.205(8)	3.204(8)
c (Å)	5.20(2)	5.20(3)	5.19(3)	5.19(3)	5.19(3)
z_1 Ga/Zn	0.378(7)	0.377(7)	0.378(8)	0.378(8)	0.377(8)
Ga/N occ	0.51	0.57	0.70	0.78	0.90
Zn/O occ	0.49	0.43	0.30	0.22	0.10

Table 5.7. Refinement parameters from fits to NOMAD neutron pair distribution function data of $(GaN)_{1-x}(ZnO)_x$ from $x = 0.10 – 0.49$ using three different model types in PDFGui.[121]

Model	Sample	$U_{11}= U_{22}$ Ga/Zn (Å^2)	U_{33} Ga/Zn (Å^2)	$U_{11} = U_{22}$ N/O (Å^2)	U_{33} N/O (Å^2)	R_w
wurtzite	x = 0.10	0.00617	0.00678	0.02793	0.00791	0.148
	x = 0.22	0.00646	0.00672	0.02798	0.00712	0.144
	x = 0.30	0.00839	0.00732	0.03424	0.00887	0.148
	x = 0.43	0.00556	0.01037	0.00629	0.01812	0.129
	x = 0.49	0.00551	0.01075	0.00637	0.01876	0.124
1 tetrahedra	x = 0.10	0.00543	0.00524	0.02442	0.00618	0.155
	x = 0.22	0.00661	0.00630	0.02763	0.00695	0.150
	x = 0.30	0.00768	0.00733	0.03243	0.00923	0.156
	x = 0.43	0.00491	0.00854	0.00522	0.01612	0.131
	x = 0.49	0.00539	0.01045	0.00649	0.01806	0.130
2 tetrahedra	x = 0.10	0.00328	0.00345	0.00159	0.00400	0.153
	x = 0.22	0.00589	0.00456	0.00386	0.00814	0.143
	x = 0.30	0.00561	0.02460	0.00500	0.00906	0.164
	x = 0.43	0.00615	0.01124	0.00341	0.00890	0.131
	x = 0.49	0.00770	0.00767	0.00335	0.00899	0.142

Although the models implemented in this study were not adequate for the proper fitting of the peak shape of the nearest-neighbor peaks, they were adequate for the determination of proper peak positions. Peak position information allows for a local bond length analysis of our samples and only lacks in quantitative analysis, as the integrated peak value gives rise to the number of specific bonds at that particular distance. A plot of average bond length as a function of the percentage of ZnO present in samples is shown in Figure 5.15 and shows strong agreement with our bond valence sum analysis. The plot encompasses data from fits using all three model types from 1.0 to 10Å, and for both NPDF and NOMAD data. NPDF data is shown as circles and NOMAD as triangles. Both the 1 tetrahedra and average wurtzite structural models show a general increase in lattice parameter with an increase in ZnO% as would be expected and as is shown from simple XRD patterns. However, locally there is a different story. Overall there is a decrease in average local Ga-N bond length and in the average local Zn-O bond length with an increase in ZnO% as indicated by the blue and red line data respectively. This is simply another indication that locally there are structural differences that do not occur over a long range length scale but only occur at the very nearest-neighbor distances (< 5Å). DFT calculations on this $(GaN)_{1-x}(ZnO)_x$ system agree well with this experimental data, confirming again that these are real physical differences in the local structure of these solid solution members.[28]

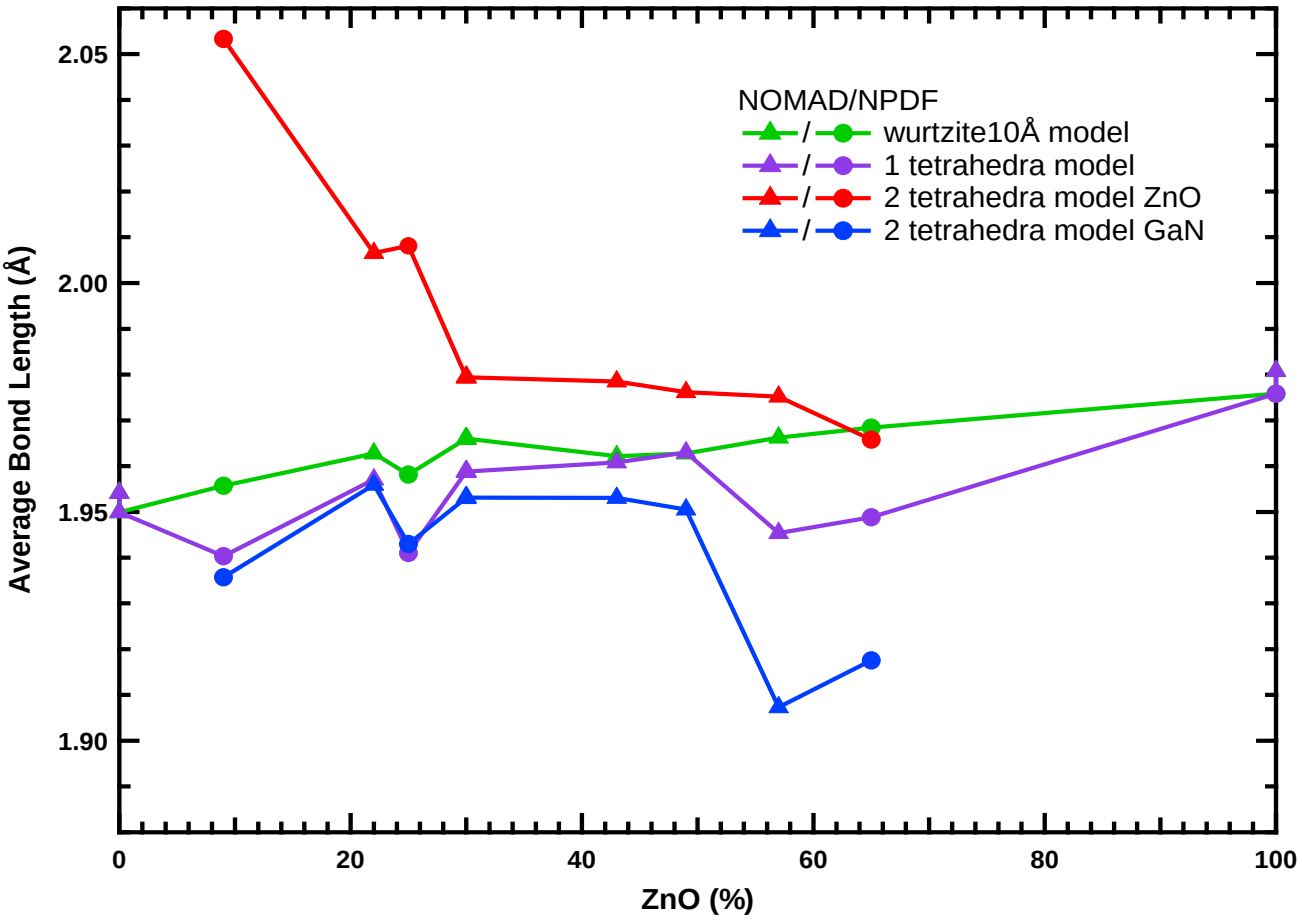

Figure 5.15. Experimental bond lengths determined through fitting experimental PDF (NOMAD and NPDF) data to three separate model types, using PDFGui software, indicating differences in local bond lengths as compared to average bond lengths.

5.4 Conclusions

The PDF response of $(GaN)_{1-x}(ZnO)_x$ end members (GaN and ZnO) is well described by their average structure, as seen in absence of peaks in the plots of the difference between the data and model. When alloying is carried out, the average structure fails to fit the data at short distance (< 5 Å), but still fits the data effectively at longer distances. Quantitative fitting finds that Ga-N bond distances noticeably shrink when ZnO is introduced while at low Zn contents, the Zn-O are substantially lengthened.

Further analysis is being conducted for the determination of a proper model for fitting the local region of our PDF data for quantitative analysis. From our analysis of neutron diffraction data using supercells with hexagonal wurtzite layers and cubic zinc blende layers, and clear evidence from TEM studies, we are aware that zinc blende structured intergrowths exist in these samples. First attempts at modeling our PDF data using ABC layered zinc-blende type and AB layered wurtzite-type separate phases was not successful. Previous pair distribution function studies on CdSe nanoparticles tackled a very similar problem to this. Bulk CdSe had been reported as having either the wurtzite or zinc blende structure, but never a combination of both until this study which showed a bulk wurtzite ($P6_3mc$) structure with extensive zinc blende (F-43*m*) type stacking faults.[122] XRD patterns showed sensitivity to the presence of planar disorder in these nanoparticles, manifested in the broadening of peaks. PDF data was fit well ($R_w < 0.30$) using a supercell structure created in the DISCUS software.[122,123,124] With our knowledge of the presence of zinc blende type intergrowths in many of these samples as discussed in Chapters 3 and 4, it seems fitting to attempt to implement one of our superstructure models into PDFGui. The program's limitations do not allow the size supercell necessary for accurately measuring a wurtzite supercell with 3-10% stacking faults. We believe the previous work was able to implement such stacking faults due to the amount present in samples (~50%). Further attempts at tackling the $r <$ 5Å range in the PDF data will be made, but it is very possible that a large box approach may be necessary for accurately modeling this range as our nearest-neighbor peaks may consist of a range of different bond types that will not be accurately modeled using PDFGui.

References

1. Lewis, N. S.; Nocera, D. G., Powering the planet: Chemical challenges in solar energy utilization. *Proceedings of the National Academy of Sciences of the United States of America* **2007,** *104* (50), 20142-20142.

2. Lewis, N. S., Nocera, D. G., Powering the planet: Chemical challenges in solar energy utilization. *Proceedings of the National Academy of Sciences U.S.A.* **2006,** (103), 15729-15735.

3. Crabtree, G. W.; Lewis, N. S., Solar energy conversion. *Physics Today* **2007,** *60* (3), 37-42.

4. Tsao, J. Lewis, N.; Crabtree, G., Solar FAQs *U.S. Department of Energy Office of Basic Energy Science documentation* **2006**, 24.

5. Archer, D. K., H.; Maier-Reimer, E., Mutiple timescales for neutralization of fossil fuel CO_2. *Geophysical Research Letters* **1997,** *24* (4), 405-408.

6. Brinkman, W. G. In *Energy Independence with Sustainability*, American Geophysical Union Fall Meeting 2012.

7. Lewis, N. S., Light work with water. *Nature* **2001,** *414*, 5889-5990.

8. Lewis, N. S., Artificial Photosynthesis. *American Scientist* **1995,** *83* (6), 534-541.

9. Nozik, A., Physical Chemistry of Semiconductor-Liquid Interfaces. *Journal of Physical Chemistry* **1996,** *100*, 13061-13078.

10. Shaner, M. R.; Fountaine, K. T.; Ardo, S.; Coridan, R. H.; Atwater, H. A.; Lewis, N. S., Photoelectrochemistry of core-shell tandem junction n-p(+)-Si/n-WO_3 microwire array photoelectrodes. *Energy & Environmental Science* **2014,** *7* (2), 779-790.

11. Tan, M. X. Lewis, N.S.; Laibinis, P.E.; Nguyen, S. T.; Stanton, C.E.; Kesselman, J.M., *Principles and Applications of Semiconductor Photoelectrochemistry*. John Wiley & Sons: Pasadena, CA. , 1994.

12. Maeda, K., Domen, K., New Non-Oxide Photocatalysts Designed for Overall Water Splitting under Visible Light. *Journal of Physical Chemistry C* **2007,** *111*, 7851-7861.

13. Van de Krol, R., Liang, Y.; Schoonman, J., Solar hydrogen production with nanostructured metal oxides. *Journal of Materials Chemistry* **2008,** *18*, 2311-2320.

14. Honda, K., Fujishima, A., Electrochemical Photolysis of Water at a Semiconductor Electrode. *Nature* **1972,** *238*, 37-38

15. Wrighton, M. S. E., A.B.; Wolczanski, P. T.; Morse, D. L.; Abrahamson, H. B.; Gineley, D. S. , Efficient Photoassisted Electrolysis of Water at Zero Applied Potential. *Journal of the American Chemical Society* **1976,** *98* (10), 2774-2779

16. (a) Osterloh, F. E.; Parkinson, B. A., Recent developments in solar water-splitting photocatalysis. *MRS Bulletin* **2011,** *36* (1), 17-22; (b) Osterloh, F. E., Inorganic Materials as Catalysts for Photochemical Splitting of Water. *Chemistry of Materials* **2008,** (20), 35-54.

17. Domen, K. N., S.; Soma, M.; Onishi, T.; Tamaru, K., Photocatalytic Decompostion of Water Vapour on an NiO-$SrTiO_3$ Catalyst. *Journal of the Chemical Society Chemical Communications* **1980,** *12*, 543-544.

18. Hara, M. K., T.; Komoda, M.; Ikeda, S.; Shinohara, K.; Tanaka, A.; Konda, J.; Domen, K., Cu_2O as a photocatalyst for overall water splitting under visible light irradiation. *Chemical Communications* **1998**, 357-358.

19. Kung, H. H. Jarrett, H.S.; Sleight, A.W.; Ferretti, A., Semiconducting oxide anodes in photoassisted electrolysis of water. *Journal of Applied Physics* **1997,** *46* (6).

20. Kasahara, A., Domen, K., Photoreactions on $LaTiO_2N$ under Visible Light Irradiation. *Journal of Physical Chemistry A* **2002,** *106*, 6750-6753

21. Kasahara, A. N., K.; Takata, T.; Kondo, J.N.; Hara, M.; Kobayashi, H.; Domen, K., $LaTiO_2N$ as a Visible-Light (<600nm)-Driven Photocatalyst. *Journal of Physical Chemistry B* **2003,** *107*, 791-797.

22. Hara, M., Hitoki, G., Takata, T., Konda, J. N., Kobayashi, H., Domen, K., TaON and Ta_3N_5 as new visible light driven photocatalysts *Catalysis Today* **2003,** *78*, 555-560.

23. Maeda, K., Takata, T., Hara, M., Saito, N., Inoue, Y., Kobayashi, H., Domen, K., GaN:ZnO Solid Solution as a Photocatalyst for Visible-Light Driven Overall Water Splitting. *JACS Communications* **2005,** *127*, 8286-8287.

24. Maeda, K., Teramura, K., Saito, N., Inoue, Y., Kobayashi, H., Domen, K., Overall water splitting using (oxy)nitride photocatalysts. *Pure Applied Chemistry* **2006,** *78* (12), 2267-2276

25. Domen, K., Maeda, K. , Oxynitride materials for solar water splitting. *Materials Research Bulletin* **2011,** *36*, 25-31.

26. Jensen, L. L., Muckerman, James T., Newton, Marshall D. , First-Principles Studies of the Structural and Electronic Properties of the $(Ga_{1-x}Zn_x)(N_{1-x}O_x)$ Solid Solution Photocatalyst. *Journal of Physical Chemistry C* **2008,** *112*, 3439-3446.

27. Wang, S. W., L.-W., Atomic and Electronic Structures of GaN/ZnO Alloys. *Physical Review Letters* **2010,** *104* (6).

28. Li, L., Muckerman; J. T.; Hybertsen, M. S.; Allen, P. B. , Phase diagram, structure, and electronic properties of $(GaN_{1-x}Zn_x)(N_{1-x}O_x)$ solid solutions from DFT-based simulations. *Physical Review B* **2011,** *83*, 134202-1 - 134202-6.

29. Hashiguchi, H., Maeda, K., Abe, R., Ishikawa, A., Kubota, J., Domen, K. , Photoresponse of GaN:ZnO Electrode on FTO under Visible Light Irradiation. *Bulletin of the Chemical Society of Japan* **2009,** *82* (3), 401-407.

30. Chen, H. Y.; Wang, L. P.; Bai, J. M.; Hanson, J. C.; Warren, J. B.; Muckerman, J. T.; Fujita, E.; Rodriguez, J. A., In Situ XRD Studies of ZnO/GaN Mixtures at High Pressure and High Temperature: Synthesis of Zn-Rich $(Ga_{(1-x)}Zn_{(x)})(N_{(1-x)}O_{(x)})$ Photocatalysts. *Journal of Physical Chemistry C* **2010,** *114* (4), 1809-1814.

31. Wang, J. H., B.; Wang, Z.; Wang, P.; Cheng, H.; Zheng, Z.; Qin, X.; Zhang, X.; Dai, Y.; Whangbo, M.-H., Facile synthesis of Zn-rich $(GaN)_{1-x}(ZnO)_x$ solid solutions using layered double hydroxies as precursors. *Journal of Materials Chemistry* **2011,** *21*, 4562-4567.

32. Hisatomi, T., Maeda, K., Lu, Daling, Domen, K. , The Effects of Starting Materials in the Synthesis of $(Ga_{1-x}Zn_x)(N_{1-x}O_x)$ Solid Solution on Its Photocatalytic Activity for Overall Water Splitting under Visible Light *ChemSusChem* **2009,** *2*, 336-343

33. Lee, K., Tienes, B.M., Wilker, M.B., Schnitzenbaumer, K.J., Dukovic, G., $(Ga_{1-x}Zn_x)(N_{1-x}O_x)$ Nanocrystals: Visible Absorbers with Tunable Composition and Absorption Spectra. *Nano Letters* **2012,** *12* (6), 3268-3272.

34. Sun, X. M., K.; Le Faucheur, M.; Teramura, K.; Domen, K., Preparation of $(Ga_{1-x}Zn_x)(N_{1-x}O_x)$ solid-solution from $ZnGa_2O_4$ and ZnO as a photo-catalyst for overall water splitting under visible light. *Applied Catalysis A* **2007,** *327*, 114-121.

35. Maeda, K., Domen, K., Solid Solution of GaN and ZnO as a Stable Photocatalyst for Overall Water Splitting under Visible Light. *Chemistry of Materials Review* **2010,** *22*, 612-623.

36. Smart, L. E., Moore, E.A., *Solid State Chemistry: An Introduction*. Taylor & Francis: Boca Raton, 2005; p 407.

37. Pecharsky, V. K., Zavalij, P.Y., *Fundamentals of Powder Diffraction and Structural Characterization of Materials*. Second ed.; Springer: New York, 2009.

38. Denton, A. R. A., N.W., Vegard's law. *Physical Review A* **1991,** *43*, 3161.

39. Dann, S. E., *Basic Concepts in Chemistry*. Wiley Interscience: The Royal Society of Chemistry: Bristol, Great Britain, 2002; p 201.

40. Goldstein, J. I., Newbury, D. E., Echlin, P., Joy, D. C., Romig, A.D., Lyman, C. E., Fiori, C., Lifshin, E., *Scanning Electron Microscopy and X-Ray Microanalysis: A Text for Biologiests, Materials Scientists, and Geologists*. Second Edition ed.; Plenum Press: New York, 1992; p 820.

41. William, D. B. Carter, C.B., *Basics I*. Springer: New York, 1996.

42. Kubelka, P. Munk, F. , *Fur Tekn. Physik* **1931,** *12*.

43. Laws, D. D., Bitter, H-M. L., Jerschow, A., Solid State NMR Spectroscopic Methods in Chemistry. *Angewandte Chemie-International Edition* **2002,** *41*, 3096-3129.

44. Schwenzer, B.; Hu, J.; Seshadri, R.; Keller, S.; Den Baars, S. P.; Mishra, U. K., Gallium Nitride Powders from Ammonolysis: Influence of Reaction Parameters on Structure and Properties. *Chemistry of Materials* **2004,** *16*, 5088.

45. Egami, T., Billinge, S.J.L., *Underneath the Bragg Peaks: Structural Analysis of Complex Materials*. Pergamon - Elsevier: Amsterdam, 2003; p 424.

46. Maeda, K., Teramura, K., Lu, D., Takata, T., Saito, N., Inoue, Y., Domen, K., Photocatalyst releasing hydrogen from water - Enhancing catalytic performance holds promise for hydrogen production by water splitting in sunlight. *Nature* **2006,** *440* (7082), 295-295.

47. Sun, X. M., K.; Le Faucheur, M.; Teramura, K.; Domen, K., Preparation of $(Ga_{1-x}Zn_x)(N_{1-x}O_x)$ solid-solution from $ZnGa_2O_4$ and ZnO as a photo-catalyst for overall water splitting under visible light. *Applied Catalysis A* **2007,** *327*, 114.

48. Michiue, Y., Kimizuka, N. , Superspace description of the homologous series $Ga_2O_3(ZnO)_m$. *Acta Crystallographica Section B Structural Science* **2009,** *B66*, 117-129.

49. Kimizuka, N., Isobe, M., Nakamura, M., Syntheses and Single-Crystal Data of Homologous Compounds, $In_2O_3(ZnO)_m$ (m = 3,4, and 5), $InGaO_3(ZnO)_3$, and $Ga_2O_3(ZnO)_m$ (m = 7,8,9, and 16) in the In_2O_3-$ZnGa_2O_4$-ZnO System. *Journal of Solid State Chemistry* **1995,** *116*, 170-178.

50. Michiue, Y., Kimizuka, N., Kanke, Y. , Structure of $Ga_2O_3(ZnO)_6$: a member of the homologous series $Ga_2O_3(ZnO)_m$. *Acta Crystallographica Section B Structural Science* **2008,** *64*, 521-526

51. Li, C., Bando, Y., Nakamura, M., Kurashima, K., Kimizuka, N., Structure analysis of new homologous compounds $Ga_2O_3(ZnO)_m$ (m = integer) by high resolution analytical transmission electron microscopy. *Acta Crystallographica Section B Structural Science* **1999,** *55*, 355-362

52. Kimizuka, N.; Isobe, M.; Nakamura, M.; Mohri, T., Syntheses and Crystallographic Data of the Homologous Compounds $InFeO_3(ZnO)_m$ (m = 1, 2, 3, 7, 11,13,15, and 19) and $Fe_2O_3(ZnO)_m$ (m = 8 and 9) in the In_2O_3-$ZnFe_2O_4$-ZnO System. *Journal of Solid State Chemistry.* **1993,** *103*, 394.

53. Kimizuka, N.; Isobe, M.; Nakamura, M., Syntheses and Single-Crystal Data of Homologous Compounds, $In_2O_3(ZnO)_m$ (m = 3,4, and 5), $InGaO_3(ZnO)_3$, and $Ga_2O_3(ZnO)_m$ (m = 7,8,9, and 16) in the In_2O_3-$ZnGa_2O_4$-ZnO System. *Journal of Solid State Chemistry*. **1995,** *116*, 170.

54. Phani, A. R.; Santucci, S.; Di Nardo, S.; Lozzi, L.; Passacantando, M.; Picozzi, P., Preparation and characterization of bulk $ZnGa_2O_4$. *Journal of Materials Science.* **1998,** *33*, 3969.

55. Maeda, K.; Takata, T.; Hara, M.; Saito, N.; Inoue, Y.; Kobayashi, H.; Domen, K., GaN:ZnO Solid Solution as a Photocatalyst for Visible-Light Driven Overall Water Splitting. *Journal of the American Chemical Society Communications.* **2005,** *127*, 8286.

56. Chen, H. W., L.; Bai, J.; Hanson, J. C.; Warren, J. B.; Muckerman, J. T.; Fujita, E.; Rodriguez, J. A. , In Situ XRD Studies of ZnO/GaN Mixtures at High Pressure and High Temperature: Synthesis of Zn-Rich $(Ga_{(1-x)}Zn_{(x)})(N_{(1-x)}O_{(x)})$ Photocatalysts. *Journal of Physical Chemistry C* **2010,** *114*, 1809.

57. Sun, X.; Maeda, K.; Le Faucheur, M.; Teramura, K.; Domen, K., Preparation of $(Ga_{1-x}Zn_x)(N_{1-x}O_x)$ solid-solution from $ZnGa_2O_4$ and ZnO as a photo-catalyst for overall water splitting under visible light. *Applied Catalysis, A* **2007,** *327*, 114.

58. Maeda, K.; Teramura, K.; Takata, T.; Hara, M.; Saito, N.; Toda, K.; Inoue, Y.; Kobayashi, H.; Domen, K., Overall Water Splitting on $(Ga_{1-x}Zn_x)(N_{1-x}O_x)$ Solid Solution Photocatalyst: Relationship between Physical Properties and Photocatalytic Activity. *Journal of Phyical Chemistry B* **2005,** *105*, 20504

59. Kikkawa, S.; Nagasaka, K.; Takeda, T.; Bailey, M.; Sakurai, T.; Miyamoto, Y., Preparation and lithium doping of gallium oxynitride by ammonia nitridation via a citrate precursor route. *Journal of Solid State Chemistry* **2007,** *180*.

60. Maeda, K.; Teramura, K.; Saito, N.; Inoue, Y.; Kobayashi, H.; Domen, K., Overall water splitting using (oxy)nitride photocatalysts. *Pure Applied Chemistry* **2006,** *78* (12), 2267

61. Wang, J.; Huang, B.; Wang, Z.; Wang, P.; Cheng, H.; Zheng, Z.; Qin, X.; Zhang, X.; Dai, Y.; Whangbo, M., Facile synthesis of Zn-rich $(GaN)_{1-x}(ZnO)_x$ solid solutions using layered double hydroxies as precursors. *Journal of Materials Chemistry.* **2011,** *21,* 4562.

62. Han, W.; Zhang, Y.; Nam, C.; Black, C. T.; Mendez, E. E., Growth and electronic properties of GaN/ZnO solid solution nanowires *Applied Physics Letters* **2010,** *97*.

63. Maeda, K.; Teramura, K.; Domen, K., Effect of post-calcination on photocatalytic activity of $(Ga_{1-x}Zn_x)(N_{1-x}O_x)$ solid solution for overall water splitting under visible light *Journal of Catalysis* **2008,** *254* (2), 198-204.

64. Visvanathan, S., Free Carrier Absorption Due to Polar Modes in the III-V Compound Semiconductors. *Physical Review* **1960,** *120* (2), 379.

65. Fan, H. Y., Infrared absorption in semiconductors. *Reports on Progress in Physics* **1956,** *19*, 107.

66. Fan, H. Y.; Spitzer, W.; Collins, R. J., Infrared absorption in n-type Germanium *Physical Review* **1956,** *101* (2), 566.

67. Thomas, D. G., Infrared absorption in zinc oxide crystals. *Journal of Physics and Chemistry of Solids* **1959,** *10* (1), 47.

68. Weiher, R. L., Optical Properties of Free Electrons in ZnO. *Physical Review* **1966,** *152* (2), 736.

69. Vanheusden, K.; Warren, W. L.; Seager, C. H.; Tallant, D. R.; Voigt, J. A., Correlation between photoluminescence and oxygen vacancies in ZnO phosphors. *Journal of Applied Physics* **1996,** *79*, 7983.

70. Hisatomi, T.; Maeda, K.; Lu, D.; Domen, K., The Effects of Starting Materials in the Synthesis of $(Ga_{1-x}Zn_x)(N_{1-x}O_x)$ Solid Solution on Its Photocatalytic Activity for Overall Water Splitting under Visible Light**.** *ChemSusChem.* **2009,** *2*, 336.

71. Choi, T.; Lee, S.; Choi, Y. J.; Kiryukhin, V.; Cheong, S. W., Switchable Ferroelectric Diode and Photovoltaic Effect in $BiFeO_3$. *Science* **2009,** *324* (5923), 63-66.

72. Li, L.; Rohrer, G. S.; Salvador, P. A., Heterostructured ceramic powders for photocatalytic hydrogen production: nanostructured TiO_2 shells surrounding microcrystalline (Ba, Sr) TiO_3 cores. *Journal of the American Chemical Society* **2012,** *95* (4), 1414.

73. Paulauskas, I. E.; Katz, J. E.; Jellison, G. E.; Lewis, N. S.; Boatner, L. A., Photochemical studies of semiconducting photoanodes for hydrogen production via water dissociation. *Thin Solid Films* **2008,** *516* (22), 8175-8178.

74. Waltereit, P.; Brandt, O.; Trampert, A.; Grahn, H. T.; Menniger, J.; Ramsteiner, M.; Reiche, M.; Ploog, K. H., Nitride semiconductors free of electrostatic fields for efficient water light-emitting diodes. *Nature* **2000,** *406*.

75. Strite, S.; Morkoc, H., GaN, AIN, and InN - a review. *Journal of Vacuum Science & Technology B* **1992,** *10* (4), 1237-1266.

76. Yeh, C. Y.; Lu, Z. W.; Froyen, S.; Zunger, A., Zinc-Blende-Wurtzite polytipism in semiconductors. *Physical Review B* **1992,** *46* (16), 10086-10097.

77. Xu, Y. N.; Ching, W. Y., Electronic, optical, and structural properties of some wurtzite crystals *Physical Review B* **1993,** *48* (7), 4335-4351.

78. Powell, R. C.; Lee, N. E.; Kim, Y. W.; Greene, J. E., Heteroepitaxial wurtzite and zincblende structure GaN grown by reactive-ion-molecular-beam epitaxy - growth-kinetics, microstructure, and properties. *Journal of Applied Physics* **1993,** *73* (1), 189-204.

79. Lei, T.; Fanciulli, M.; Molnar, R. J.; Moustakas, T. D.; Graham, R. J.; Scanlon, J., Epitaxial-growth of zinc blende and wurtzitic gallium nitride thin-films on (001) silicon. *Applied Physics Letters* **1991,** *59* (8), 944-946.

80. Porowski, S., Growth and properties of single crystalline GaN substrates and homoepitaxial layers. *Mater. Sci. Eng. B-Solid State Mater. Adv. Technol.* **1997,** *44* (1-3), 407-413.

81. Callahan, M.; Wang, B. G.; Rakes, K.; Bliss, D.; Bouthillette, L.; Suscavage, M.; Wang, S. Q., GaN single crystals grown on HVPE seeds in alkaline supercritical ammonia. *Journal of Materials Science* **2006,** *41* (5), 1399-1407.

82. Shin, H.; Thomson, D. B.; Schlesser, R.; Davis, R. F.; Sitar, Z., High temperature nucleation and growth of GaN crystals from the vapor phase. *J. Cryst. Growth* **2002,** *241* (4), 404-415.

83. Li, S.; Yang, G. W., Phase Transition of II-VI Semiconductor Nanocrystals. *Journal of Physical Chemistry C* **2010,** *114* (35), 15054-15060.

84. Lany, S., Polymorphism, band-structure, band-lineup, and alloy energetics of the group II oxides and sulfides MgO, ZnO, CdO, MgS, ZnS, CdS. *Oxide-Based Materials and Devices V* **2014,** 8987.

85. Kulkarni, A. J.; Wang, J.; Sarasamak, K.; Limpijumnong, S.; Ke, F. J.; Zhou, M., *Polymorphism of zinc oxide nanowires*. 2008; p 70-77.

86. Steger, G.; Jagodzinski, H.; Frey, F., Polytypism and phase-transformation zinc blende wurtzite. *Acta Crystallographica Section A* **1984,** *40*, C461-C461.

87. Wells, A. F., *Structural Inorganic Chemistry*. Clarendon Press: Oxford, 1984.

88. Yashima, M.; Yamada, H.; Maeda, K.; Domen, K., Experimental visualization of covalent bonds and structural disorder in a gallium zinc oxynitride photocatalyst $(Ga_{1-x}Zn_x)(N_{1-x}O_x)$: origin of visible light absorption. *Chemical Communications* **2010,** *46* (14), 2379-2381.

89. Yashima, M.; Maeda, K.; Teramura, K.; Takata, T.; Domen, K., Crystal structure analysis of $(Ga_{0.93}Zn_{0.07})(N_{0.9}O_{0.10})$ oxynitride photocatalyst. *Materials Transactions* **2006,** *47* (2), 295-297.

90. West, A. R., *Solid State Chemistry and its Application*. John Wiley & Sons: 1984.

91. Jagodzinski, H., Polytypism in SiC crystals *Acta Crystallographica* **1954,** *7* (3), 300-300.

92. Jagodzinski, H., Der symmetrieeinfluss auf den allgeneinen losungsansatz eindimensionaler fehlordnungsprobleme *Acta Crystallographica* **1954,** *7* (1), 17-25.

93. Liu, R.; Bell, A.; Ponce, F. A.; Chen, C. Q.; Yang, J. W.; Khan, M. A., Luminescence from stacking faults in gallium nitride. *Applied Physics Letters* **2005,** *86* (2).

94. Van de Walle, C. G., Theory of impurities and defects in III-nitrides: Vacancies in GaN and related materials. In *Silicon Carbide and Related Materials - 1999 Pts, 1 & 2*, Carter, C. H.; Devaty, R. P.; Rohrer, G. S., Eds. 2000; Vol. 338-3, pp 1561-1566.

95. Yan, Y. F.; Al-Jassim, M. M., Inversion domain boundaries in ZnO: First-principles total-energy calculations. *Physical Review B* **2004,** *69* (8).

96. Wang, X. D.; Li, J.; Hart, R. D.; van Riessen, A.; McDonald, R., Quantitative X-ray diffraction phase analysis of poorly ordered nontronite clay in nickel laterites. *Journal of Applied Crystallography* **2011,** *44*, 902-910.

97. Maeda, K.; Domen, K., Photocatalytic Water Splitting: Recent Progress and Future Challenges. *Journal of Physical Chemistry Letters* **2010,** *1* (18), 2655-2661.

98. Maeda, K., Teramura, K., Takata, T., Hara, M., Saito, N., Toda, K., Inoue, Y., Kobayashi, H., Domen, K., Overall Water Splitting on $(Ga_{1-x}Zn_x)(N_{1-x}O_x)$ Solid Solution Photocatalyst: Relationship between Physical Properties and Photocatalytic Activity. *Journal of Physical Chemistry B* **2005,** *105*, 20504-20510

99. Reinert, A. A.; Payne, C.; Wang, L.; Ciston, J.; Zhu, Y.; Khalifah, P. G., Synthesis and Characterization of Visible Light Absorbing $(GaN)_{1-x}(ZnO)_x$ Semiconductor Nanorods. *Inorganic Chemistry* **2013,** *52* (15) 8389.

100. Popa, N. C., The (hkl) dependence of diffraction-line broadening caused by strain and size for all Laue groups in Rietveld refinement. *Journal of Applied Crystallography* **1998,** *31*, 176-180.

101. Stephens, P. W., Phenomenological model of anisotropic peak broadening in powder diffraction. *Journal of Applied Crystallography* **1999,** *32*, 281-289.

102. Popa, N. C.; Balzar, D., Size-broadening anisotropy in whole powder pattern fitting. Application to zinc oxide and interpretation of the apparent crystallites in terms of physical models. *Journal of Applied Crystallography* **2008,** *41*, 615-627.

103. Fertitta, K. G.; Holmes, A. L.; Neff, J. G.; Ciuba, F. J.; Dupuis, R. D., High-quality GaN heteroepitaxial films grown by metalorganic chemical-vapor-deposition. *Applied Physics Letters* **1994,** *65* (14), 1823-1825.

104. Ufer, K.; Kleeberg, R.; Bergmann, J.; Dohrmann, R., Rietveld refinement of disordered illite-smectite mixed-layer structures by a recursive algorithm. II: powder-pattern refinement and quantitative phase analysis *Clays and Clay Minerals* **2012,** *60* (5), 535-552.

105. Ufer, K.; Kleeberg, R.; Bergmann, J.; Curtius, H.; Dohrmann, R., Refining real structure parameters of disordered layer structures within the Rietveld method. *Zeitschrift Fur Kristallographie* **2008**, 151-158.

106. Ufer, K.; Stanjek, H.; Roth, G.; Dohrmann, R.; Kleeberg, R.; Kaufhold, S., Quantitative phase analysis of bentonites by the Rietveld method. *Clays and Clay Minerals* **2008,** *56* (2), 272-282.

107. Ufer, K.; Roth, G.; Kleeberg, R.; Stanjek, H.; Dohrmann, R.; Bergmann, J., Description of X-ray powder pattern of turbostratically disordered layer structures with a Rietveld compatible approach. *Zeitschrift Fur Kristallographie* **2004,** *219* (9), 519-527.

108. Leoni, M., Diffraction analysis of layer disorder. *Zeitschrift Fur Kristallographie* **2008,** *223* (9), 561-568.

109. Liu, J.; Nichols, E. J.; Howe, J.; Misture, S. T., Enhanced photocatalytic activity of TiO_2-niobate nanosheet composites. *Journal of Materials Research* **2013,** *28* (3), 424-430.

110. Yesinowski, J. P.; Purdy, A. P., Defect dynamics observed by NMR of quadrupolar nuclei in gallium nitride. *Journal of the American Chemical Society* **2004,** *126* (30), 9166-9167.

111. Yesinowski, J. P., ^{69,71}Ga and ^{14}N high-field NMR of gallium nitride films. *Physica Statue Solidi c* **2005,** *2* (7).

112. Jeschke, G. J., M., High-Resolution ^{14}N Solid-State NMR Spectroscopy. *Angewandte Chemie-International Edition* **1998,** *37* (9), 1282-1283.

113. Schwenzer, B.; Hu, J.; Wu, Y.; Mishra, U. K., Elucidation of the correlation between atomic-level defects in GaN nanoparticles and photoluminescence properties by NMR, XRD and TEM *Solid State Sciences* **2006,** *8*, 1193.

114. Jung, W.-S. H., O.H.; Chae, S-A., Solid-state gallium NMR characterization of cubic gallium nitride prepared by the reaction of gallium arsenide with ammonia. *Materials Chemistry and Physics* **2006,** *100*, 199-202.

115. Brese, N. E. O. K., M., Bond-Valence Parameters for Solids. *Acta Crystallographica* **1990,** *B47*, 192-197.

116. Billinge, S. J. L.; Kanatzidis, M. G., Beyond crystallography: the study of disorder, nanocrystallinity and crystallographically challenged materials with pair distribution functions. *Chemical Communications* **2004,** (7), 749-760.

117. Proffen, T.; Billinge, S. J. L.; Egami, T.; Louca, D., Structural analysis of complex materials using the atomic pair distribution function - a practical guide. *Zeitschrift Fur Kristallographie* **2003,** *218* (2), 132-143.

118. Jeong, I. K. H., R.H.; Grad, M.J.; Billinge, S.J.L., Lattice dynamics and correlated atomic motion from the atomic pair distribution function. *Physical Review B* **2003,** *67*.

119. Chung, J. S. T., M. F., Local atomic structure of semiconductor alloys using pair distribution functions. *Physical Review B* **1997,** *55* (3).

120. Peterson, P. F.; Proffen, T.; Jeong, I. K.; Billinge, S. J. L.; Choi, K. S.; Kanatzidis, M. G.; Radaelli, P. G., Local atomic strain in $ZnSe_{(1-x)}Te_{(x)}$ from high real-space resolution neutron pair distribution function measurements. *Physical Review B* **2001,** *63* (16).

121. Farrow, C. L.; Juhas, P.; Liu, J. W.; Bryndin, D.; Bozin, E. S.; Bloch, J.; Proffen, T.; Billinge, S. J. L., PDFfit2 and PDFgui: computer programs for studying nanostructure in crystals. *J. Phys.-Condes. Matter* **2007,** *19* (33).

122. Masadeh, A. S.; Bozin, E. S.; Farrow, C. L.; Paglia, G.; Juhas, P.; Billinge, S. J. L.; Karkamkar, A.; Kanatzidis, M. G., Quantitative size-dependent structure and strain determination of CdSe nanoparticles using atomic pair distribution function analysis. *Physical Review B* **2007,** *76* (11).

123. Neder, R. B. P., T. , *Diffuse Scattering and Defect Structure Simulations A cook book using the program DISCUS*. Oxford University Press: Oxford, 2008.

124. Proffen, T.; Neder, R. B., DISCUS: A program for diffuse scattering and defect-structure simulation. *Journal of Applied Crystallography* **1997,** *30*, 171-175.